FROM SINGLE TO COLLECTIVE: MODEL SWIMMERS AT INTERMEDIATE REYNOLDS NUMBERS

Thomas John Dombrowski

A dissertation submitted to the faculty of the University of North Carolina at Chapel Hill in partial fulfillment of the requirements for the degree of Doctor of Philosophy in the Physics and Astronomy department in the College of Arts & Sciences.

Chapel Hill
2021

Approved by:

Daphne Klotsa

Laura Miller

Fabian Heitsch

Yue Wu

Michael Falvo

ABSTRACT

Thomas John Dombrowski: From Single to Collective: Model Swimmers at Intermediate Reynolds Numbers
(Under the direction of Daphne Klotsa)

Biological and artificial swimmers exist across a broad range of length scales, spanning from micron-sized bacteria and self-propelled nanoparticles to large aquatic organisms and marine robots on the order of meters. Swimming can be categorized by the Reynolds number (Re) which characterizes the relative importance of inertial over viscous forces. Microscopic swimmers at low Re, where viscosity dominates, swim differently than high Re swimmers, where inertia dominates. Between the two extremes resides the intermediate Reynolds regime ($\mathrm{Re}_{\mathrm{int}} \approx 0.1 - 1000$), where both viscosity and inertia play a role. Mesoscopic organisms i.e. those that operate at intermediate Re are diverse both in size, $\approx$ 0.5mm - 50cm, and in swimming mechanisms. Most prior studies on $\mathrm{Re}_{\mathrm{int}}$ motility have focused on the details of specific organisms. As a result, few general models exist and there is a lack of understanding regarding the unifying physical mechanisms that swimmers at $\mathrm{Re}_{\mathrm{int}}$ exhibit. In this dissertation, we use computational fluid dynamics to model and characterize mesoscale swimmers, examine their pairwise interactions, and ultimately build a framework to understand their collective behavior. We first show a simple model swimmer used to understand the transition from Stokes ($\mathrm{Re} = 0$) to intermediate Reynolds numbers. Our swimmer is a dumbbell which consists of two unequal spheres that oscillate in antiphase generating nonlinear steady streaming flows. We show computationally that steady streaming flows enable the swimmer to propel itself and switch direction as Re increases. We quantify the transition in the swimming direction by collapsing my data on a critical Re and show that the transition in swimming direction corresponds to the reversal of the flows. From thousands of initial conditions, four stable pairs were identified, where the swimmers coordinated in-line or in-tandem. We investigated how the stable pairs' fluid flow fields evolved across Re and connected them to transitions in pair swimming behavior. The collective behavior of 122 swimmers transitions from in-line network-like connections to small, transient in-tandem clusters. Pairwise interactions were used to partly explain the collective behavior; however, limitations were discovered as many-body interactions such as triples were also identified.

ACKNOWLEDGEMENTS

There were many people in my life who assisted and encouraged me throughout my graduate career. I'd like to first thank my PhD advisor, **Daphne Klotsa**. I'll never forget the first time Daphne showed me slides from her latest presentation on active matter and collective behavior. That moment became a turning point in not only my graduate studies but also my future. I'm truly grateful for all the time, assistance, and opportunities Daphne provided me as my advisor/mentor. I am sincerely thankful to my Masters advisor **Fabian Heitsch** for being instrumental in my growth as a graduate student. I want to thank the other members of my committee, **Michael Falvo**, **Laura Miller**, and **Yue Wu** who have each provided me with scientific support and direction. I would also like to thank **Shannon Jones** for all of her guidance and support during my first year in the Klotsa group. Shannon was always very patient with me, and she made my transition between research groups and subject matter really easy and enjoyable. To the current and former Klotsa group members **Tom Kolb**, **Ian Seim**, **Nick Lauersdorf**, and **Hong Nguyen**, thank you for the stimulating scientific discussions and brainstorming sessions. Thank you to **Joule Othman**, **Charlie Bonfield**, and **Chris Frazer** for being great friends and for making my life in Chapel Hill truly enjoyable. I wish you all the best in your future endeavours.

I am indebted to my longtime and closest friend **Brandon Symoens**. Brandon has the most contagious laughter I've ever heard and is also one of the most caring and compassionate people I know. To my best friends **Charlie Lewsadder**, **John Blozinski**, and **Kaitlyn Shotwell**, thank you for always being there for me. I am proud to call you all and the rest of the crew my second family. I would also like to thank all the friends I have made outside of work during my time as a graduate student, especially **Dan Brown** and **James Checrallah**. I truly appreciate their encouragement and support throughout the years.

Most important of all, this work would have been impossible without the undying love and support from my family. I will forever be grateful to my mom and my dad who instilled in me a strong set of core values and always encouraged me to follow my dreams. And thank you to my brother Andrew who is truly a role model and somebody I've looked up to over the years.

TABLE OF CONTENTS

LIST OF TABLES viii

LIST OF FIGURES ix

LIST OF ABBREVIATIONS xi

1 Introduction 1

1.1 Swimmers across Reynolds numbers 1

1.2 Onset of inertia and swimming transitions 4

1.3 Steady streaming 5

2 Transition in swimming direction in a model self-propelled inertial swimmer 8

2.1 Overview 8

2.2 Introduction 8

2.3 Simulation Model 10

2.3.1 Immersed Boundary Method 10

2.3.2 Grid convergence study 13

2.3.3 Spherobot Model 13

2.4 Simulation Methods 16

2.5 Results 20

2.6 Discussion 21

2.7 Conclusions 22

2.8 Supplemental Information 23

2.8.1 Momentum flux calculations 23

2.8.2 Additional spherobot velocity data 23

3 Kinematics of a simple reciprocal model swimmer at intermediate Reynolds numbers 28
3.1 Overview 28
3.2 Introduction 28
3.3 Methods 31
3.4 Results 36
3.4.1 Kinematics 36
3.4.1.1 Small-sphere-leading (SSL) 38
3.4.1.2 Large-sphere-leading (LSL) 38
3.4.1.3 Separate spheres 38
3.4.2 Power and recovery 42
3.5 Fluid Flows and Efficiency 45
3.6 Discussion 48
3.7 Supplemental Information 51
3.7.1 Kinematics 51
3.7.1.1 Center of Mass: Displacement and Velocity 52
3.7.1.2 Individual spheres: Displacement and Velocity 52
3.7.1.3 Expansion and Compression 52
3.7.2 Fluid Flow and Efficiency 53
4 Pairwise and collective behavior between model swimmers at intermediate Reynolds numbers 62
4.1 Overview 62
4.2 Introduction 62
4.3 Model and Methods 64
4.4 Results 69
4.4.1 Pair stable states 69
4.4.2 Pair velocity as a function of Re 69
4.4.3 Pair fluid flows and swimming 73
4.4.4 Collective Behavior of Multiple Swimmers 75

4.5 Conclusions 76
4.6 Supplemental Information 77
4.6.1 Collective Methods 77
4.6.2 Pair stable states 81
4.6.3 Pair initial configurations for sweep across Re 82
4.6.4 Stable pair separation distances and in-tandem V angle vs. Re 82
4.6.5 Pair identification algorithm in multiple swimmer systems 82
BIBLIOGRAPHY 86

LIST OF TABLES

2.1 Simulation parameters. 12

3.1 List of net displacements 36

LIST OF FIGURES

1.1 Swimming organisms organized by their travelling speed and the Reynolds number 2

1.2 Stokes flow time reversibility and larval fish starvation 4

1.3 Experimental externally-vibrated asymmetric pair achieves locomotion 5

1.4 Low amplitude steady streaming limits 6

2.1 Grid convergence study for spherobot 14

2.2 3D spherobot schematic and the fluid mesh refinement 15

2.3 Spherobot oscillation schematic over one cycle 17

2.4 Universal swimming transition collapse of the spherobot 18

2.5 Spherobot stroke-averaged fluid flows in the two regimes: small-sphere-leading and large-sphere-leading 19

2.6 Momentum flux calculated upstream and downstream from the spherobot for both swimming regimes 24

2.7 Velocity of spherobot as a function of Re for constant A (a) and d_0 (b) 25

2.8 Velocity of the spherobot over a range of Re for different sphere sizes 26

2.9 Velocity of the spherobot and the swimming transition range 27

3.1 Reciprocal oscillation of the spherobot over one cycle and simulation parameters 32

3.2 Kinematic quantities plotted as functions of time over one cycle of oscillation after steady state had been reached. 37

3.3 Velocities of the large sphere, small sphere, and the spherobot's CM over an oscillation cycle 39

3.4 Fit expansion and compression displacements with respect to Re, ϵ, and d_0 using a multiple variable linear regression 41

3.5 The power and recovery strokes over a range of Re 43

3.6 The average velocity field of a small-sphere-leading and large-sphere-leading spherobot averaged over expansion, compression, and an oscillation cycle 46

3.7 Efficiency of a spherobot with parameters $\epsilon = 1.2$ and $\hat{d}_0 = 6.5$ as a function of Re 49

3.8 The continuous evolution of the spherobot's fluid flow across Re 50

3.9 The legend used for the displacement and velocity figures that follow 52

3.10 Net displacement of the spherobot Δy_{CM} during an oscillation. 53

3.11 Velocity of the spherobot v_{CM} during an oscillation. 54

3.12 Net displacement of large sphere Δy_R during an oscillation. 55

3.13 Net displacement of small sphere Δy_r during an oscillation. 56

3.14 Net displacement of individual spheres: top row = sphere of radius R and bottom row = sphere of radius r for the spherobot of equilibrium distance $\hat{d}_0 = 6.5$. 57

3.15 Velocity of large sphere v_R during an oscillation. 58

3.16 Velocity of small sphere v_r during an oscillation. 59

3.17 Net expansion displacement Δy_{exp} and compression displacement Δy_{com} for the spherobot with constant $\epsilon = 1.2$ versus Re 60

3.18 Net expansion displacement Δy_{exp} and compression displacement Δy_{com} for the spherobot with constant $\epsilon = 1.2$ versus Re on a log-log scale 60

3.19 Efficiency of a spherobot with amplitude $\epsilon = 1.2$ with varying $\hat{d}_0$ as a function of Re 61

4.1 Swim stroke of the asymmetric dumbbell, and a pair of asymmetric dumbbells separated by a distance H and oriented with angle θ 65

4.2 Identified regions of diverging or stable pairs after steady state had been reached based on initial configurations. 68

4.3 The swimming velocity of an in-tandem V pair, a parallel in-line pair, and a single swimmer versus the Reynolds number 70

4.4 Stroke-averaged fluid flow for an individual dumbbell, in-tandem V, in-tandem orbit, parallel in-line, and anti-parallel in-line pairs on the 100th swim stroke 72

4.5 Collective behavior evolution of multiple asymmetric dumbbell swimmers over a range of Re 74

4.6 Schematic illustration of all key parameters in simulations of many-spherobot systems 78

4.7 Identified regions of diverging or stable pairs for Re = 7 81

4.8 The separation distance and the angle between two swimmers measured for the four stable pairs as a function of Re. 82

4.9 Schematics of the parameters between a pair of asymmetric used in the pair identification algorith for multiple swimmers 83

4.10 Determination of three parameters $\{\theta_1, \theta_2, l\}$ for all stable pair configurations 84

LIST OF ABBREVIATIONS

Re	Reynolds number
SS	Steady streaming
CM	Center of mass
SSL	Small-sphere-leading
LSL	Large-sphere-leading

CHAPTER 1:
Introduction

1.1 Swimmers across Reynolds numbers

Swimmers are seen across all different scales, from the microscopic where bacteria thrive to the macroscopic where real-life organisms can even be tens of meters in length. Whether microscopically swimming within blood streams or macrocscopically coasting in the deep blue, swimmers are influenced by both inertial and viscous forces. The non-dimensional ratio known as the Reynolds number (Re) determines the relative importance of inertial over viscous forces. In general, Re is defined to be Re $=$ inertia forces/viscous forces $= \rho u L/\mu$, where ρ is the density of the surrounding fluid, u is the velocity of the swimming organism, L is the characteristic length scale (usually the organism's size), and μ is the dynamic viscosity of the surrounding fluid. Swimming can be categorized into three different regimes of fluid flow: Stokes regime, intermediate regime, and inviscid regime (Fig. 1.1)[1].

The Stokes regime is where the Reynolds number approaches zero, Re $\ll 1$, viscosity dominates, and inertia can be neglected. Here, we find microorganisms such as microalgae, bacteria, sperm cells, and small larval fish. Because the organisms are so small, the surrounding fluid feels very thick to them and is analogous to a human swimming in a tar pit or mollasses. On the other end of the spectrum is the inviscid regime, Re $\gg 1$, where inertia dominates and viscosity is neglected. Here, we see larger and faster organisms which can exhibit fascinating collective behavior like how sardines form bait balls to protect themselves from predators. In these two limiting cases, one can make mathematical simplifications to the Navier-Stokes equations that govern the fluid dynamics.

Simple models have been developed to understand organisms in Stokes flow, a well-studied one being the squirmer. A spherical squirmer is a simple model for self-propulsion at low Re which was developed by Lighthill and Blake to mimic the locomotion of organisms with dense arrays of motile cilia[2,3]. The squirmer achieves locomotion through small, axisymmetric perturbations tangential to its surface. The squirmers are divided by the parameter β, which quantifies the amount of fluid-mixing done by the squirmer. When $\beta > 0$,

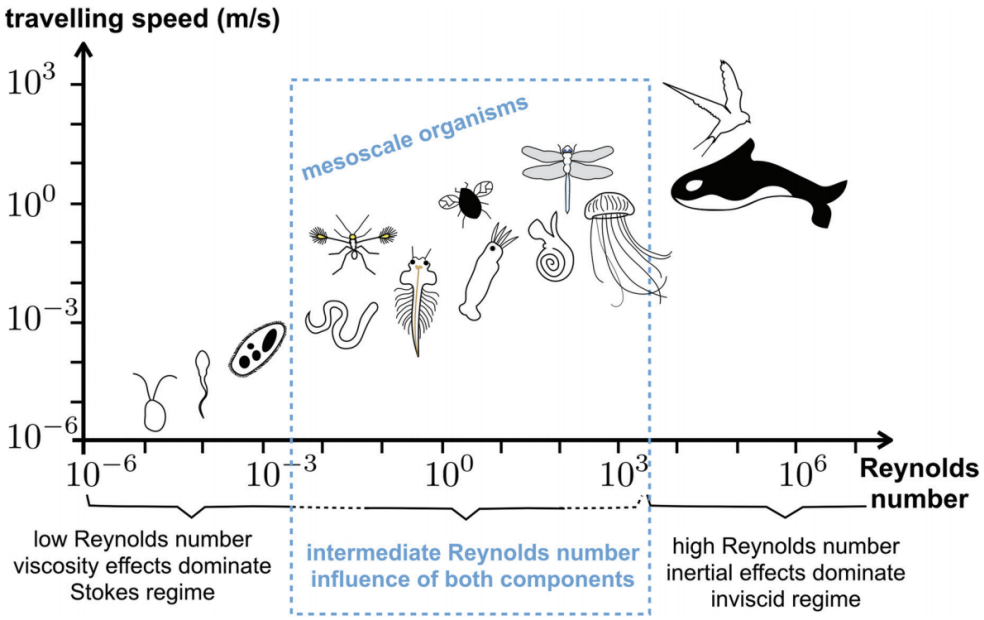

Figure 1.1: Organisms organized by their travelling speed and the Reynolds number. The Reynolds number can be used to divide the swimming organisms into three regimes of fluid flow: Stokes regime, intermediate regime, and inviscid regime. The Stokes regime is where viscous forces dominate and inertial forces are neglected. The inviscid regime is the opposite where inertial forces dominate and viscous forces are neglected. In between, the intermediate regime is where the inertial and viscous forces are both finite and lead to very diverse swimming behaviors. Reproduced from[(1)].

squirmers are classified as pullers, $\beta < 0$ as pullers, and $\beta = 0$ as neutral. Microalgae Chlamydomonas can be modeled as a puller where the fluid is pulled in parallel to its axis of motion and pushed away perpendicular to it, while spermatozoa can be modeled as a pusher where there is the opposite, a push parallel and a pull perpendicular.

Between the two extremes resides the intermediate Reynolds regime (Re $\approx 1 - 1000$), where both finite viscous and inertial forces are important. Finite inertia is relevant for millions of mesoscopic organisms, i.e. those that operate at intermediate Re, and robots that swim or fly covering at least three orders of magnitude in size ($\approx$ 0.5mm–50cm). Along with a variable size comes different functionality: jet propulsion from squids and jellyfish[4,5], anguilliform (or eel-like) locomotion from nematodes[6–10], a flapping motion from water boatmen[11], and metachronal and ciliate beating from organisms like brine shrimp[12,13]. Yet, despite their enormous scope and diversity, their collective behavior is largely unknown. The main challenge arises due to the comparable inertial and viscous forces resulting in nonlinear hydrodynamic effects. Mathematical simplifications cannot be made to the Navier-Stokes equations, and solutions are analytically intractable for individual swimmers and for the collective system. For that matter, most studies are experimental and focus on specific organisms[4–7,9–18]. Recently, numerical work has been published on different models of mesoscale organisms[19–33].

An interesting classification of swimmers was developed by Purcell where swimmers are separated into reciprocal and non-reciprocal swim strokes. A reciprocal swim stroke is the same forwards as it is backwards in time. One can think of a scallop opening and closing as a reciprocal swim stroke, and it is impossible to discern if the scallop is performing its swim stroke forward or in reverse. A non-reciprocal swim stroke lacks time reversibility, and the swim stroke appears different when performed forward and in reverse. An example of this is seen from organisms with flagella. Their corkscrew spinning motion is not time reversible. Purcell's scallop theorem states that at low Re, if an organism tries to swim by a reciprocal motion, it cannot move anywhere[34]. Organisms which are able to swim by themselves in Stokes flow must have a non-reciprocal swim stroke. This is why microorganisms developed non-reciprocal swimming mechanisms, such as the metachronal motion of cilia and the corkscrew motion of flagella.

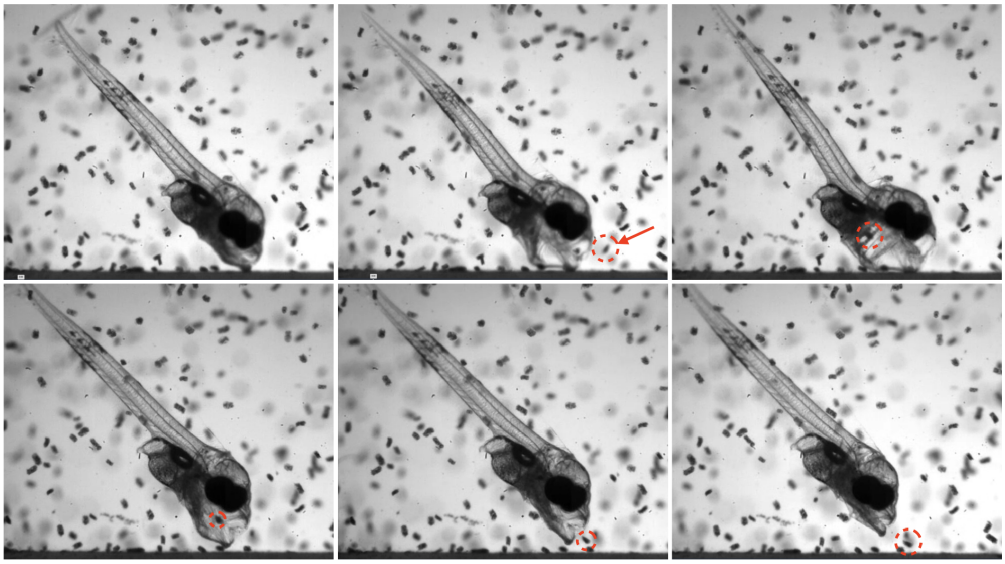

Figure 1.2: Larval fish trying to catch prey (indicated in red circle and arrow) and failing. The fish opens its mouth, sucks the prey in, and then, as it closes its mouth, the prey escapes. Images extracted from movie in supplemental information of China and Holzman[35].

1.2 Onset of inertia and swimming transitions

What happens to real biological organisms that live on the boundary between low Re, where viscosity dominates, and Re_{int}, where inertia starts to play a role? How do they reconcile the difference in the fluid dynamics between the two regimes? This interesting region in phase space was studied by Childress and Dudley[36] who reported on a mollusc that changes its swimming stroke as it grows in size and thus transitions from the Stokes regime to the intermediate Re regime. Muller et al.[37] show that undulatory swimmers, such as zebra fish, are well-suited to transitioning through different regimes of Re. From a mathematical point of view, Lauga studied model swimmers and showed a continuous breakdown of the Scallop theorem when inertia is gradually introduced[19]. Recently, China and Holzman[35] argued that the reason larval fish die in the larval stage at a high percentage (99%) is because they have difficulty eating food at low Re where the flows are reversible – they suck the food in but then as they close their mouths it goes out again, see Fig. 1.2.

Childress and Dudley asked: "Can models of reciprocal flapping be found which exhibit the bifurcation from rest to locomotion as viscosity decreased, and which are consistent with our observations?"[36]. The question was later investigated by looking at an externally-vibrated asymmetric pair, which was designed to be simply implemented experimentally and to study the transition from rest at low Re to locomotion as Re increases and inertia kicks in[28]. The pair was powered by external oscillations of the fluid-filled

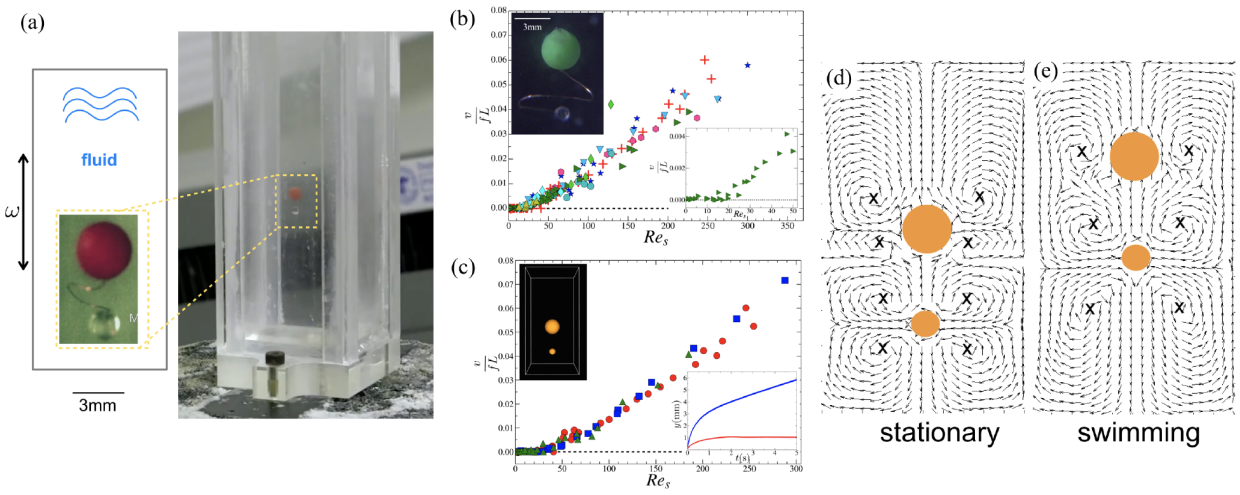

Figure 1.3: (a) Experimental realization of a robot (two unequal spheres connected by a spring) driven by flow oscillations at Reint. (b) Velocity as a function of the streaming Reynolds number, indicating discontinuous onset with increasing Res, ($= A^2\omega/\nu$). (c) Average fluid flows around the pair when it is stationary, below the critical onset, and (e) when it swims, above the critical onset. (b-e) are reproduced from[28]

container (Fig. 1.3a,b) and was studied both computationally and experimentally. The results showed that the asymmetric pair undergoes a discontinuous transition from rest to swimming (with the large sphere at the front) at a critical value Re ≈ 30. Above the critical value, the speeds scaled linearly with the oscillatory Reynolds number, for various parameters (amplitude, frequency, spheres' sizes, their aspect ratio, distance between them, and fluid viscosity ν) collapsing on a straight line, shown in Fig. 1.3b,c. The fluid flows were also found to be qualitatively different below and above the critical Re, further evidence for a discontinuous transition, see Fig. 1.3d,e. However, this is a different problem than a self-propelling organism because of the external vibration and can thus be hard to compare or reach general conclusions.

1.3 Steady streaming

We introduce the phenomenon known as steady streaming to better explain how the externally-vibrated pair achieved locomotion at Re > 30. Steady streaming is the non-zero time averaged flow for a rigid, oscillating body at intermediate Re. Despite the attention streaming flow has won over the years, it is still not fully understood, as it involves the nonlinear Navier-Stokes equations over a large parameter space. We shall define four dimensionless parameters which have been used in the literature: the Reynolds number Re, the inverse strouhal number ε, the streaming Reynolds number Re_s, and M^2. The radius of the oscillating sphere

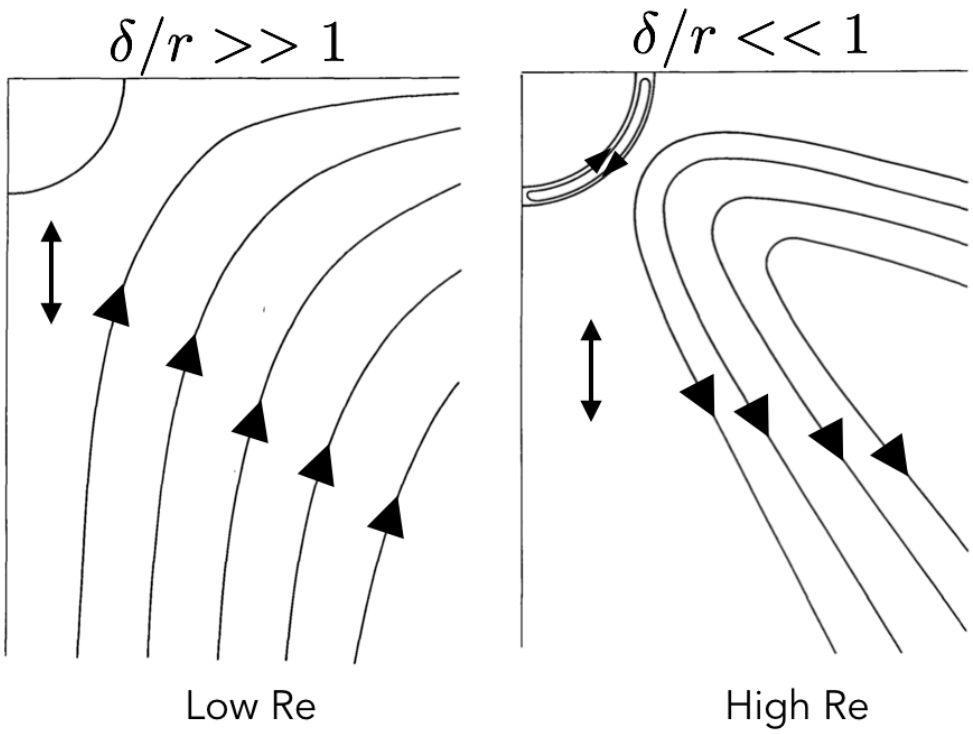

Figure 1.4: When $\varepsilon \ll 1$, there are two limiting cases to steady streaming. (a) The sphere oscillates with $M^2 \gg 1$ and $\mathrm{Re}_s \ll 1$ and generates a vortex pair which pulls fluid in along the oscillation axis and pushes out perpendicular to it. (b) When $M^2 \gg 1$ and Re has increased, a second counter rotating vortex pair forms. Reproduced from[38].

is r, the amplitude of oscillation is A, the angular frequency is ω, the kinematic viscosity of the fluid is ν, and the boundary layer thickness is $\delta = sqrt\nu/\omega$. The dimensionless ratios are:

$$\text{Re} = Ar/\delta^2, \tag{1.1}$$

$$\varepsilon = A/r \tag{1.2}$$

$$Re_s = \varepsilon\text{Re} = A^2/\delta^2, \tag{1.3}$$

$$M^2 = Re/\varepsilon = r^2/\delta^2. \tag{1.4}$$

The solution to the velocity field changes in structure in different limits and thus the form of the steady streaming flow pattern depends on the location of the specific problem in this parameter space. In some cases, the structure observed is of the form shown schematically in Fig. 1.4a and depending on the parameters there is a transition to the structure shown in Fig. 1.4b. Using perturbation theory, for low amplitudes $\varepsilon \ll 1$, Riley[38,39] showed that Fig. 1.4a occurs for $M^2 \gg 1$ and $\text{Re}_s \ll 1$ and Fig. 1.4b for $M^2 \ll 1$. When the sphere oscillates in a fluid with high viscosity and low Re, the flow is dominated by one vortex pair where the flow pulls in along the oscillation axis and pushes out perpendicular to it. When the viscosity is decreased and Re is increased, the one vortex pair shrinks and another counter-rotating vortex pair forms.

In Chapters 2 and 3, we introduce an internally-powered model swimmer that consists of two unequal sized spheres which propels itself using steady streaming flows. We study the swimming dynamics and fluid flow on average, and we relate the swim stroke's movement and generated flow to behavior seen in real-life organisms. In Chapter 4, we first investigate the pair interactions between two model swimmers and then expand the system to 122 swimmers to observe their collective behavior. Each chapter can be read as a stand alone manuscript.

CHAPTER 2:
Transition in swimming direction in a model self-propelled inertial swimmer[1]

2.1 Overview

We propose a reciprocal, self-propelled model swimmer at intermediate Reynolds numbers (Re). Our swimmer consists of two unequal spheres that oscillate in antiphase generating nonlinear steady streaming (SS) flows. We show computationally that the SS flows enable the swimmer to propel itself, and also switch direction as Re increases. We quantify the transition in the swimming direction by collapsing our data on a critical Re and show that the transition in swimming directions corresponds to the reversal of the SS flows. Based on our findings, we propose that SS can be an important physical mechanism for motility at intermediate Re.

2.2 Introduction

Understanding motility requires connections between fundamental physics and biology[40–42] and has many applications, including drug-delivering nanomachines[43,44] and autonomous underwater vehicles[45–47]. Swimming regimes can be classified by the Reynolds number (Re), which characterizes the relative importance of inertial over viscous forces. Although there is a large body of work on motility in Stokes flows ($Re \ll 1$), in which viscous forces dominate, and at high Re ($Re \gg 1$), in which inertial forces dominate, less is known about the intermediate regime $Re_{\text{int}} \sim 1 - 1000$[41,48,49].

The Re_{int} regime encompasses an enormous diversity of organisms, ranging from larvae (of *e.g.* fish, squid, ascidian) and large ciliates, to nematodes, copepods, plankton and jellyfish, that exhibit a variety of motility mechanisms: jet propulsion[4,5], anguilliform locomotion [6–10], rowing[14,15], aquatic flapping flight[11], and ciliate beating[12,13]. Plankton have even been proposed to contribute to the large-scale transport of nutrients and dissolved gases in the ocean[16,17,24,50,51]. However, most prior studies on Re_{int} motility have

[1] This chapter previously appeared as an article in *Physical Review Fluids*. The original citation is as follows: T. Dombrowski, S.K. Jones, G. Katsiskis, A.P.S. Bhalla, B.E. Griffith, and D. Klotsa, Transition in swimming direction in a model self-propelled inertial swimmer. *Phys. Rev. Fluids* **4**, 021101(R) (2019)

focused on the details of specific organisms [4–7,9–18]. As a result, few general models exist for motility at Re_{int}; examples are an extension of the Stokesian squirmer to include inertia[19–24], which makes assumptions about the generation of flow due to small-amplitude oscillations on the surface of a spherical swimmer and the flapping-plate model, which is a lumped-torsional-flexibility model that uses passive pitching and responds to an actuation[26,27]. However, there is a lack of understanding regarding the unifying physical mechanisms that swimmers at Re_{int} exhibit. To achieve this, more models with varying degrees of freedom that operate under different conditions at Re_{int} are needed. Only then can we make progress in better understanding biological swimmers and designing artificial ones at intermediate scales.

Steady streaming (SS) is the nonzero, time-averaged flow that arises at Re_{int} due to oscillations of a rigid body in a fluid and has been studied for various cases, such as around a single sphere[38,39,52–54], cylinder, near a wall. While SS has been used to manipulate particles *e.g.*[28,55–58] and cells[59] via *external* vibrations, it has not been used as a mechanism for self-propulsion, even though there have been suggestions that it may be relevant for the enhanced motility of *Synechococcus* cyanobacteria[60].

In this letter we propose a simple, reciprocal, and self-propelled model swimmer, termed the *spherobot*, that uses steady streaming flows in a novel way, *i.e.* for propulsion. The spherobot is composed of two unequal spheres that oscillate with respect to each other, in antiphase, generating SS flows, Fig. 2.3(a). We computationally studied the spherobot's motility over a broad range of parameters: viscosity, sphere amplitudes, distance between the spheres, sphere radii and sphere-radii ratio. At $Re = 0$, the spherobot cannot swim because of Purcell's scallop theorem[34]; its reciprocal stroke does not break time-reversal symmetry. At low, nonzero Re the spherobot started to swim and, interestingly, switched swimming direction from a small-sphere-leading to a large-sphere-leading regime. We found that the point of transition collapsed to a critical value when the appropriate Reynolds number was used, which revealed a strong dependence on the SS flows of the small sphere. Analyzing the flow fields, we showed that the transition in swimming direction corresponds to the reversal of SS flows around the spherobot that occurs as the Reynolds number increases.

2.3 Simulation Model

2.3.1 Immersed Boundary Method

To simulate the dynamics of the spherobot in a fluid, we used the immersed boundary (IB) method[61]. We specifically used an exactly constrained immersed boundary (CIB) method[62,63] to enforce the rigid-body motion of the two spheres that comprise the spherobot. This method also allowed us to couple the two spheres via a stiff spring. The fluid surrounding the spherobot was assumed to be viscous and incompressible.

The IB method for fluid-structure interaction uses an Eulerian formulation of the momentum equation and incompressibility constraint for the coupled fluid-solid system along with a Lagrangian description of the motion of the immersed structures. Let $\mathbf{x} \in \Omega$ be fixed Eulerian physical coordinates, and let $\mathbf{s} \in U^i$ be fixed Lagrangian curvilinear coordinates attached to the structure. In our notation, $\mathbf{X}(\mathbf{s},t) \subset \Omega$ is the physical position of material point $\mathbf{s}$ at time t. The momentum equation and incompressibility constraint are given by

$$\rho \frac{D\mathbf{u}}{Dt}(\mathbf{x},t) = -\nabla p(\mathbf{x},t) + \mu \nabla^2 \mathbf{u}(\mathbf{x},t) + \mathbf{f}(\mathbf{x},t), \tag{2.1}$$

$$\nabla \cdot \mathbf{u}(\mathbf{x},t) = 0, \tag{2.2}$$

in which $\mathbf{u}(\mathbf{x},t)$ is the material velocity field, $p(\mathbf{x},t)$ is the pressure field that imposes the incompressibility constraint, $\mathbf{f}(\mathbf{x},t)$ is a body force that arrises from the presence of the immersed structure, ρ is the mass density, and μ is the viscosity. Eulerian and Lagrangian variables are coupled via integral transforms with Dirac delta function kernels:

$$\mathbf{f}(\mathbf{x},t) = \int_U \mathbf{F}(\mathbf{s},t)\, \delta(\mathbf{x} - \mathbf{X}(\mathbf{s},t))\, \mathrm{d}\mathbf{s}, \tag{2.3}$$

$$\mathbf{U}(\mathbf{s},t) = \int_\Omega \mathbf{u}(\mathbf{x},t)\, \delta(\mathbf{x} - \mathbf{X}(\mathbf{s},t))\, \mathrm{d}\mathbf{x}\,. \tag{2.4}$$

Eq. (2.3) converts the Lagrangian force density $\mathbf{F}(\mathbf{s},t)$ (which is a Lagrange multiplier force that constrains the spheres to move as rigid bodies) to an equivalent Eulerian force density $\mathbf{f}(\mathbf{x},t)$, and Eq. (2.4) evaluates the local material velocity at each structural position.

The position of each sphere of the spherobot is updated via:

$$\frac{\partial \mathbf{X}}{\partial t}(\mathbf{s},t) = \mathbf{U}(\mathbf{s},t) = \mathbf{V}_{\text{COM}} + \mathbf{W}_{\text{COM}} \wedge \mathbf{R}(\mathbf{s},t), \tag{2.5}$$

in which $\mathbf{V}_{\text{COM}}$ and $\mathbf{W}_{\text{COM}}$ are the (unknown) translational and rotational velocities, respectively, and $\mathbf{R}(\mathbf{s},t) = \mathbf{X}(\mathbf{s},t) - \mathbf{X}_{\text{COM}}(t)$ is the radius vector to the center of mass of the sphere. The Lagrangian force density $\mathbf{F}(\mathbf{s},t)$ is required to satisfy the net external force and torque constraint on the immersed body:

$$\int_U \mathbf{F}(\mathbf{s},t)\,\mathrm{d}\mathbf{s} = \mathbf{F}_{\text{external}}, \tag{2.6}$$

$$\int_U \mathbf{R}(\mathbf{s},t) \wedge \mathbf{F}(\mathbf{s},t)\,\mathrm{d}\mathbf{s} = \mathbf{T}_{\text{external}}. \tag{2.7}$$

We remark that the net external force and torque on the immersed structure excludes hydrodynamic traction forces on the surface of the body, but could include forces and torques arising, for example, due to gravity, surface tension, tethered springs, etc. In the case of the spherobot, $\mathbf{F}_{\text{external}}$ is nonzero and results from the force applied by the active spring described in the main text, and $\mathbf{T}_{\text{external}} = \mathbf{0}$ because the active springs pass through the centers of masses of the two spheres. There are no other external forces or torques.

In our computer model, each sphere of the spherobot was composed of a mesh of Lagrangian marker points that were generated using an in-house MATLAB code, and the singular delta function kernels were replaced by a 6-point regularized kernel fuction[62]. The remainder of the spatial discretization and the time stepping algorithm for the CIB method have been described in detail in prior work by some of us[62,63].

To simulate the dynamics of the spherobot, we used a distributed-memory parallel implementation of the CIB method provided by the open-source IBAMR library[64]. For our simulations, the fluid domain occupied a container of dimensions 2 m$\times$2 m$\times$8 m in 3D and 2 m$\times$8 m in 2D, (longest dimension$=30\ r$). Three levels of local mesh refinement were used, with a refinement ratio of four between levels. The resolution of the finest level of the fluid grid corresponded to a uniform $512 \times 128 \times 128$ discretization in 3D and a 512×128 discretization in 2D (see grid convergence study below). Additionally, regions of fluid that contained a higher threshold of vorticity were dynamically refined as the simulation progressed. We used no-slip boundary conditions at all sides of the fluid domain. The structural mesh spacing was taken to be 1.25 times greater than the background Eulerian grid spacing.

For Stokes flow ($Re = 0$), we set $\rho = 0$, so that the inertial terms in the Navier-Stokes equations are zero. Additional simulation parameters are described in Table 2.1.

Note that due to the computational expense of running simulations in 3D, we performed an extensive parameter sweep in 2D to understand which parameters affect the transition between the two regimes (Fig. 2.4, Fig. 2.1) but all other results and fluid flow figures in the paper were from 3D simulations.

Table 2.1: Simulation parameters.

Parameter	**Value**
density, ρ (kg-m^{-3})	2
frequency, f (s^{-1})	10
number of Eulerian grid levels	3
Eulerian grid refinement ratio	1:4
time step size, Δt (s)	10^{-4}
2D Parameters	
Reynolds number, Re	[10^{-3}, 150.0]
inverse Strouhal number, $\epsilon = \frac{A}{r}$	[0.8, 1.6]
$M = \frac{r}{\delta}$	[0.04, 17.86]
sphere 1 radius, R (m)	[0.2, 0.375]
sphere 2 radius, r (m)	[0.15, 0.225]
equilibrium distance, d_0 (m)	[0.75, 1.50]
relative amplitude, A (m)	[0.12, 0.24]
Eulerian grid dimensions (m)	2×8
effective Eulerian grid resolution	128×512
3D Parameters	
Reynolds number, Re	$[5.0 \times 10^{-4}, 80.0]$
(includes Stokes, $Re = 0$)	
inverse Strouhal number, $\epsilon = \frac{A}{r}$	1.6
$M = \frac{r}{\delta}$	[0.02, 7.50]
sphere 1 radius, R (m)	0.3
sphere 2 radius, r (m)	0.15
equilibrium distance, d_0 (m)	0.75
relative amplitude, A (m)	0.24
Eulerian grid dimensions (m)	$2 \times 2 \times 8$
effective Eulerian grid resolution	$128 \times 128 \times 512$

2.3.2 Grid convergence study

We chose to perform the convergence study in two spatial dimensions because running 3D simulations at the most refined grid level is computationally expensive. In addition, the radial symmetry of the spherobot lead to similar behavior in two- and three-dimensions. To test for spatial convergence, we compared three effective fine-grid resolutions: a 64×256 discretization, a 128×512 discretization, and a 256×1024 discretization. The spherobot was evaluated for these three discretizations at $Re = 3$ and $Re = 80$ (two representative Reynolds numbers with the velocity in the direction of the small sphere and large sphere, respectively). Fig. 2.1 shows the position of the small and large sphere of the spherobot over a representative 8 cycles of oscillation. There was an excellent agreement between all three grid resolutions at $Re = 3$ (Fig. 2.1(a)). As expected, $Re = 80$ demonstrated the greatest error between grid resolutions (Fig. 2.1(b)) because boundary layers were smaller and resolving the separation of vortices was more challenging as Re increased. However, there was good agreement between the 128×512 and 256×1024 grids. We calculated the difference in the spherobot's position over the first 40 cycles of oscillation at 128×512 and 256×1024 grid resolution, and found the mean difference in position was less than 0.1% of body lengths at both $Re = 3$ and $Re = 80$. Similarly, we found less than a 5% difference in the average velocity of the spherobot at 128×512 and 256×1024 grid resolution at both $Re = 3$ and $Re = 80$. For that reason, an effective $128 \times 128 \times 512$ grid discretization and a 128×512 grid discretization was used for all other 3D and 2D simulations, respectively.

2.3.3 Spherobot Model

Here, we elaborate on the spherobot model (Fig. 2.2) described in the main text. At each time step, the equilibrium distance of the actuated spring is updated, and an equal and opposite force is applied to each sphere to move them a desired distance, $d(t)$, apart. The magnitude and direction of the force applied to each sphere depends on the relative positions of the two spheres. $[F_R(t), F_r(t)] = [+, -]k(x(t) - d(t))$, in which F_R is the force applied to the large sphere, F_r is the force applied to the small sphere, k is a spring constant ($k = 2.5 \times 10^4$ Nm^{-1}), and $x(t)$ is the current distance between the spheres. Note that $F_R = -F_r$ at every instance in time (i.e., the swimmer is self-propelled). The prescribed distance between the spheres' centers changes sinusoidally with time, and the model ensures a geometrically reciprocal cycle (error $\approx 10^{-7}$ m). The model conditions ensure that the spherobot swims only along the oscillation axis (vertical). The position

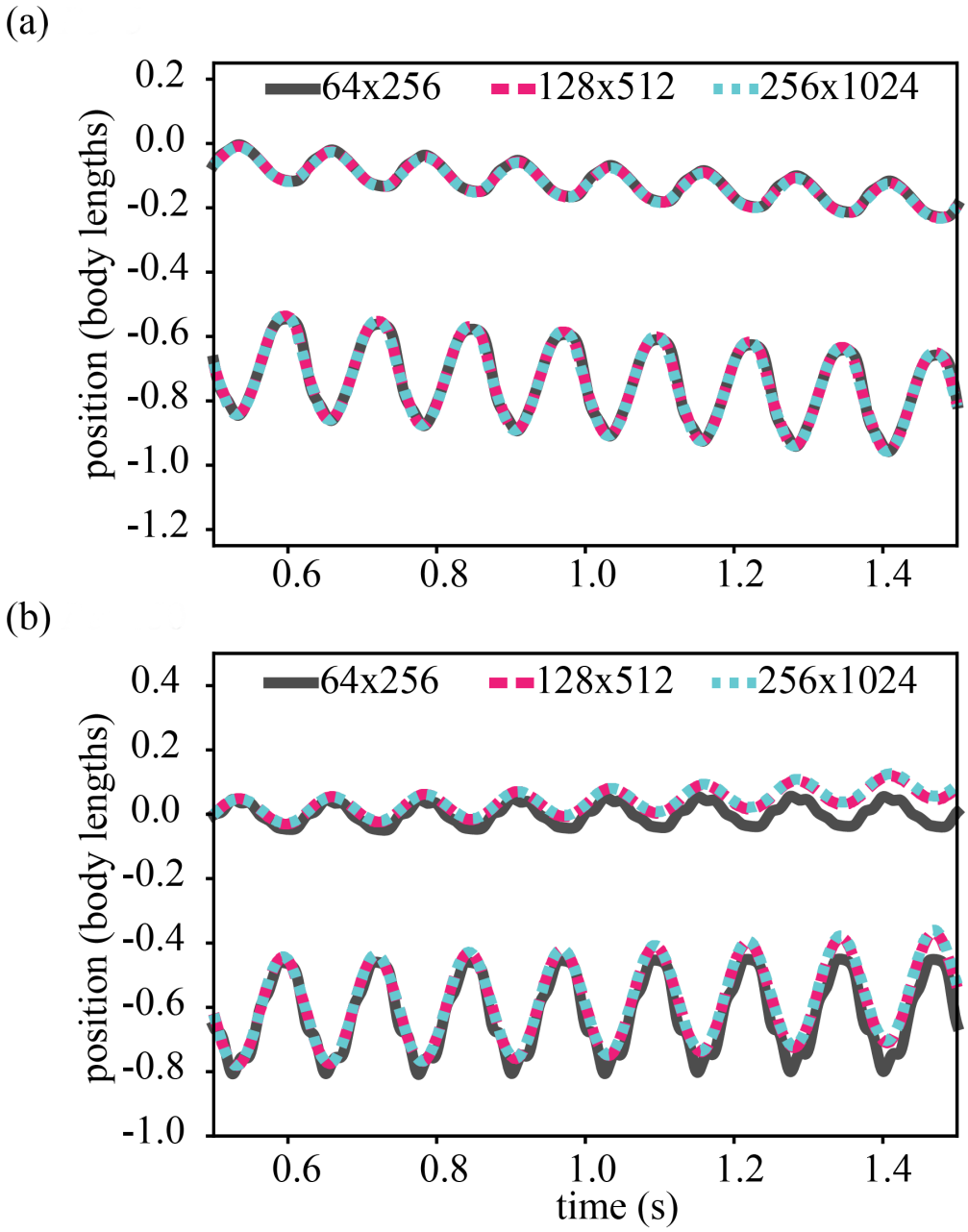

Figure 2.1: Grid convergence study shown at (a) $Re = 3$ and (b) $Re = 80$ ($R = 0.3$, $r = 0.15$, $A = 0.24$, $d_0 = 0.75$, 2D). Lines indicate the position of the large and small sphere as a function of time. Color and line style indicate grid resolution: 64×256 (dark grey, full), 128×512 (magenta, broken), 256×1024 (light blue, dashed). Effective $128 \times 128 \times 512$ grid resolution was used for all other simulations in this paper.

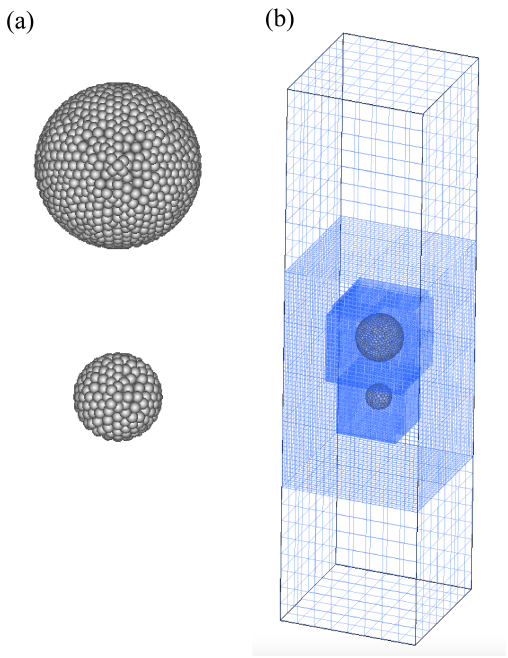

Figure 2.2: (a) Immersed boundary spherobot was composed of solid spheres with Lagrangian spacing 1.25 times greater than the Eulerian spacing. (b) The spherobot was immersed in a box with viscous, incompressible fluid. No slip boundary conditions were used on all sides.

of the center of mass (COM) of the spherobot is defined as $r_{\text{COM}} = \frac{V_R \mathbf{p_R} + V_r \mathbf{p_r}}{V_R + V_r}$, in which V_R and V_r are the volumes and $\mathbf{p_R}$ and $\mathbf{p_r}$ are the position vectors of the centers of each sphere.

We let the spherobot swim until steady state swimming speed was reached, less than a 1% change in swimming speed per cycle of oscillation between consecutive cycles. We performed a linear regression of the position of the COM and time over ten cycles of oscillation after steady state had been reached and took the slope to be the average steady state swimming speed of the spherobot. The spherobot velocity was reported as the dimensionless velocity, v/fr. The visualization and analysis of the flow fields was done in VisIt[65].

The Re used here is one of many dimensionless ratios that can be defined from the length scales A, A_r, A_R, L (characteristic size of spherobot, e.g., R, r, d_0, or some combination, such as $R + r + d_0$), and $\delta = (\frac{\nu}{2\pi f})^{1/2}$, which is the oscillatory boundary layer thickness. In this paper, we report the Reynolds number, defined as $Re = \frac{A_r r}{\delta^2}$ because it characterizes the transition between small-sphere-leading and large-sphere-leading swimming. We note that because the spheres have the same mass densities, $A_r = \frac{AR^2}{r^2+R^2}$ in 2D and $A_r = \frac{AR^3}{r^3+R^3}$ in 3D, leading to *e.g.* $A_r = 4A_R$ in 2D and $A_r = 8A_R$ in 3D (for $r = 0.15$ m, $R = 0.3$ m).

Fig. 2.4(a) of the main text shows a comparison between the velocity curves in 3D (black curve) and 2D (purple curve in inset). We clearly see that the magnitude of the velocity in 3D is smaller than it is in 2D. We note that the simulations shown are identical in A = 0.24m, R = 0.3m, r = 0.15m, and d_0 = 0.75m but are different in A_r and A_R. Our current method is unable to generate simulations with all the parameters being identical in 3D and 2D. In order to match A_R, A_r, and A in 3D, we would need to change A_r and A_R in 2D. However, the change would be in opposite directions where, in 2D, A_r would increase from 0.192m to 0.213m, but A_R would decrease from 0.048m to 0.027m. Considering the net force on the spheres must be zero, this cannot be the case. If we increase A_r, we would also need to increase A_R and in return increase A.

What would happen to the velocity if the changes were introduced? Compared to the current simulation of 2D, in which A_r = 0.192m, the magnitude of the velocity of our swimmer should increase. We have data supporting this claim. Considering Fig. 2.4(b), 2.7(b), they show us a direct relationship between V and A. The magnitude of the velocity increases as the amplitude increases. With the proposed changes to our 2D model parameters, we would in fact see a larger difference in the velocities than those of 3D and current 2D data.

2.4 Simulation Methods

The spherobot was composed of two unequal spheres with radii r, R, which were coupled to one another by prescribing the distance between their centers. To model this computationally, we tethered the two spheres using an active spring with a time-dependent distance $d(t) = d_0 + A\sin(\omega t)$, in which d_0 is the equilibrium distance between the sphere centers, $A = 0.5(d_{\text{max}} - d_{\text{min}})$ is the amplitude of the spherobot, and ω is the frequency of oscillation (Fig. 2.3). Equal and opposite (spring) forces were applied to the spheres that acted to keep them approximately at the prescribed distance apart (error $\approx 10^{-7}$m). Thus, the model ensures a geometrically reciprocal cycle and a force-free swimmer. Because the same force is applied to both spheres, the one with the smaller mass (the small sphere) will have a larger amplitude A_r than the one with the bigger mass (large sphere), A_R, (*i.e.* if $r \leq R$ then $A_r \geq A_R$). In most simulations we have $A_r \approx 4A_R$. The amplitude of the spherobot A is the sum of the two, $A = A_r + A_R$, Fig. 2.3. Both spheres were neutrally buoyant with respect to the surrounding fluid. To simulate the spherobot in a fluid, we used an exactly constrained immersed boundary (CIB) method[62,63]. The CIB scheme is implemented in IBAMR [64,66],

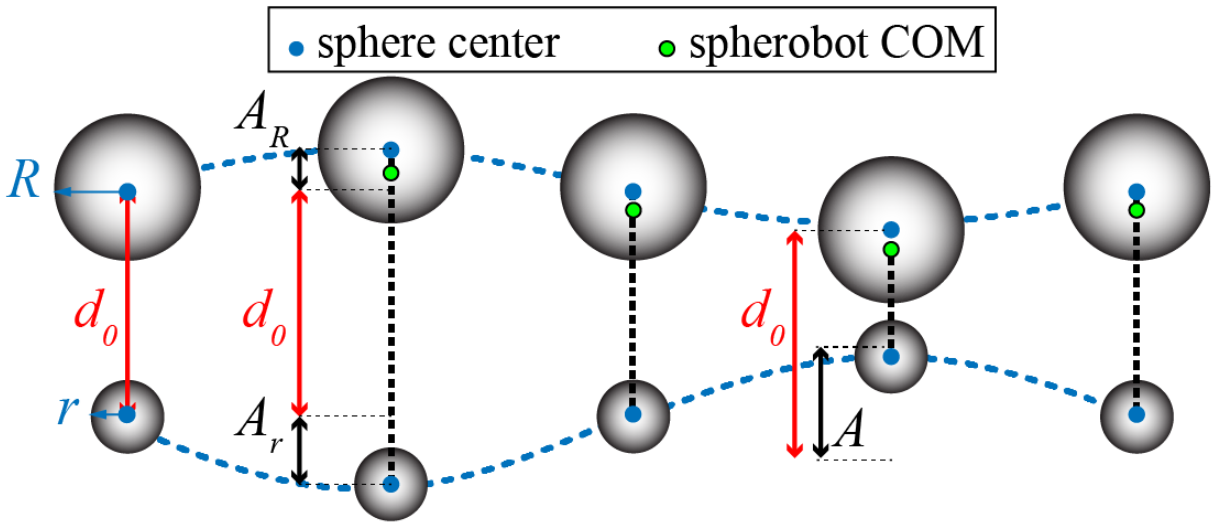

Figure 2.3: Reciprocal oscillation of the spherobot swimmer over one cycle. Spheres' centers of mass (COM)(blue circles) and the spherobot COM (green circle) are indicated. The distance between the spheres' centers, $d(t)$, is d_0, at the equilibrium distance, $d_0 - A$, minimum distance and $d_0 + A$ at maximum distance. The total amplitude $A = A_R + A_r$.

which provides several variants of the immersed boundary (IB) method[61] for fluid-structure interaction. The spherobot was immersed in a fluid that occupied a finite cell with no-slip walls. The visualization and analysis of the flow fields was done in VisIt[65]. Further details on the model and method are given in the Supplemental Material (SM)[67].

The swimming velocity of the spherobot was measured after steady state had been reached and was defined as the net displacement of the spherobot center of mass over one cycle. We defined the Reynolds number as $Re = A_r r/\delta^2 = A_r r\omega/\nu$ because, as we will show, it is the ratio that determines the transition between small-sphere-leading and large-sphere-leading regimes; $\delta = \sqrt{\nu/\omega}$ is the oscillatory boundary layer thickness and ν is the kinematic viscosity of the fluid. We carried out simulations in 2D and 3D and found qualitative agreement. We focused on 2D because it allowed us to study a much broader parameter space. The range studied in Re was $0.001 \leq Re \leq 150$. All other parameter ranges (amplitude, radii,*etc.*) are shown in the SM, table 2.1[67].

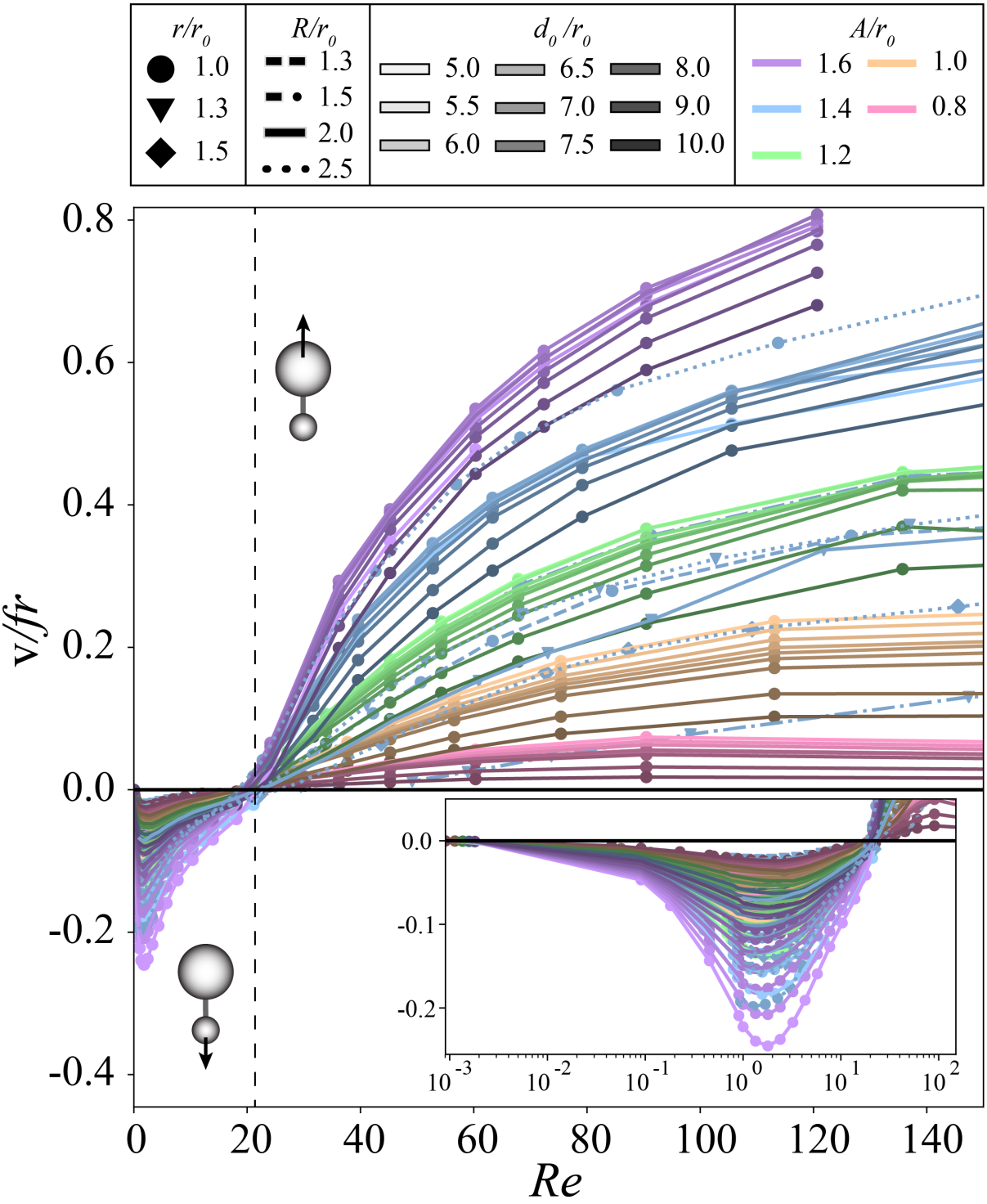

Figure 2.4: Velocity of the spherobot as a function of Re in 2D for a range of A, d_0, R, r shown in the legend. The inset shows the small-sphere-leading regime plotted on a semi-log-x scale. Parameters A, d_0, R, and r are non-dimensionalized by the length scale, $r_0 = 0.15$m, the radius for the small sphere. Line color indicates A, line saturation indicates d_0, line style indicates R, and symbols indicate r. Negative velocity indicates swimming in the direction of the small sphere, positive velocity indicates swimming in the direction of the large sphere. Vertical dashed lines denote critical Re for transition.

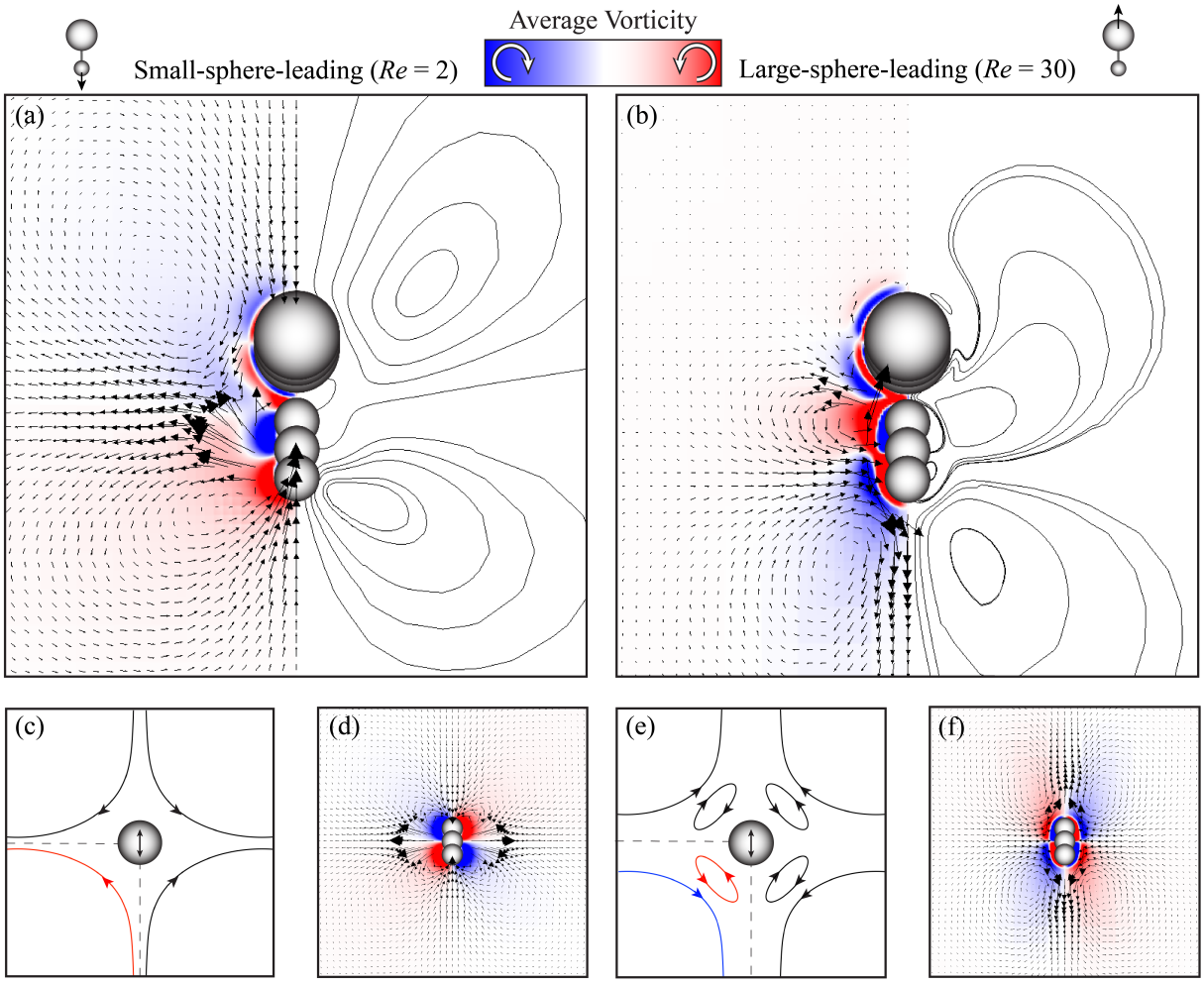

Figure 2.5: Left column: Small-sphere-leading regime at Re = 2. Right column: Large-sphere-leading regime at Re = 30. Spherobot velocity field superimposed with the vorticity field and streamlines in (a) the small-sphere-leading regime and (b) the large-sphere-leading regime. The largest dimensionless velocity magnitude in (a), (b) is $|\mathbf{v_{max}}|/fr = 0.88$. Schematic diagrams showing the reversal of steady streaming flows for one sphere in the limiting cases (c) $\delta \gg r$, and (e) $\delta \ll r$. Due to symmetry the lower left quadrant is indicated with a dashed line. Velocity vector plot superimposed with the vorticity field for one sphere at (d) $Re = 2$ and (f) $Re = 30$. The largest dimensionless velocity magnitude in (d), (f) is $|\mathbf{v_{max}}|/fr = 1.1$. All velocity vectors are scaled the same.

2.5 Results

We initially placed the spherobot in the simulation box at constant A, A_R, A_r, d_0, f, R, r and varied the Re via the kinematic viscosity, ν. As a validation, we ran a simulation at $Re = 0$ and confirmed that the spherobot did not swim because of Purcell's theorem for reciprocal swimmers[34]. As soon as $Re > 0$ (lowest value $Re = 0.001$) the spherobot began to swim in the direction of the small sphere (Fig.2.4), *i.e.* the small-sphere-leading regime. As Re increased, the speed of the spherobot increased until reaching a maximum at $Re \approx 2$. Above $Re \approx 2$ the spherobot slowed down and eventually had no net displacement (even though the spheres oscillated) at $Re \approx 20$. As Re increased further, the spherobot switched direction to swim with the large sphere on the front, *i.e.* the large-sphere-leading regime, where its increasing speed started to plateau as Re increased further. We then ran a broader parameter sweep varying R, r, A, A_R, A_r, and d_0 besides the viscosity ν. We found that the transition only depended on the small sphere's radius and amplitude (besides viscosity) and that it was independent of all the other length scales R, A_R and d_0. The transition-point data collapsed (within the scatter on a single, critical dimensionless number $Re = A_r r/\delta^2 \approx 20$ (Fig.2.4).

To gain insight into the propulsion mechanism and the switch in swimming direction, we turned our attention to the flow fields generated by the spherobot. Based on classical work on steady streaming generated by a single oscillating sphere, we expected each sphere of the spherobot to generate SS flows, which are time-averaged flows by definition. We also anticipated the SS flows around the spherobot to be different than the classical SS flows around a sphere for two reasons. First, the small sphere's oscillation amplitude, A_r, was of the same order of magnitude as the sphere radius, *i.e.* $\epsilon = A_r/r \approx O(1)$ unlike the assumption for classical steady streaming where $\epsilon \ll 1$[38,39,68]. Second, it was unclear what the cumulative SS flows of two spheres oscillating in antiphase should be, as it has only been studied for spheres and cylinders in phase[55,69–71]. Bearing these considerations in mind, we calculated the time-averaged flow fields around the spherobot, varying the same parameters as before, (Fig. 2.4). We found that the switch in the swimming direction at $Re \approx 20$ corresponded to the reversal of the SS flows both parallel and perpendicular to the axis of oscillation. Specifically, in the small-sphere-leading regime ($Re < 20$), the fluid, on average, was pulled in towards the spheres along the axis of oscillation and was pushed out away from the spheres along the axis perpendicular to the oscillation, (Fig. 2.5 (a)). On the contrary, in the large-sphere-leading regime ($Re > 20$), the fluid, on average, did the opposite – it was pushed away from the spheres along the direction of swimming

(with a strong downward jet below the small sphere) and was pulled in towards the gap between the spheres in the direction perpendicular-to-swimming (Fig. 2.5 (b)).

Furthermore, in both regimes it is clear that the velocity vectors along the oscillation axis are larger around the small sphere than the large sphere, (Fig. 2.5). In fact, through control volume analysis we found that for both regimes, the momentum flux on the side of the small sphere was larger than the momentum flux on the side of the large sphere, (the ones along the perpendicular axis generated fluxes that canceled each other). Though initially unexpected, this finding makes sense together with the collapse, which depends on the Re of the small sphere only, (Fig. 2.4). The net momentum flux of course switches direction as the swimming direction switches, (see Fig. 2.6[67]). Our data, thus, strongly suggest that the transition in the spherobot's swimming direction is due to the reversal of SS flows, which is associated with the switch in the direction of the net momentum flux[67].

2.6 Discussion

To better understand the reversal of SS flows, we will consider what is known for one sphere. Analytic solutions have been obtained under the small-amplitude assumption $A_r \ll r$ and in the two limiting cases relating the sphere radius to the boundary layer thickness, $\delta \gg r$ and $\delta \ll r$. The two limiting cases demonstrate a reversal in direction, shown schematically in Fig. 2.5(c),(e)[38,39,68]. In the first case, the boundary layer thickness is much larger than the radius, $\delta \gg r$, (Fig. 2.5(c)). Due to symmetry we describe one quadrant of flow. A single vortex that is the boundary layer is generated near the surface of the sphere, which pulls fluid along the axis of oscillation and pushes fluid out in the perpendicular. In the second case, the boundary layer thickness is much smaller than the radius of the sphere, $\delta \ll r$, (Fig. 2.5(e)). Two vortices are generated swirling in opposite directions. The boundary layer is confined into an inner vortex close to the surface of the sphere (same direction as in the first case) but there is an additional outer vortex in the opposite direction – it pushes fluid out along the axis of oscillation and pulls it in along the perpendicular. The analytical limiting solutions, that we just described, provide us a with qualitative picture; we cannot use them for direct comparison because neither $A_r \ll r$ nor $\delta \gg r$ or $\delta \ll r$ holds true for our system. Instead, we compare our results to experiments and simulations, where $\epsilon = A_r/r = O(1)$ and $r/\delta = O(1)$, as for the spherobot.

Unlike the spherobot where the reversal of flows corresponds to a switch in the direction of swimming, the point where reversal of flows occurs for a single sphere is not well-defined[38,52,72,73]. Experimental observations have reported that they could observe the inner vortex when $r/\delta \leq 4$[74], while experiments and simulations reported the coexistence of inner and outer vortices with opposing flows for $r/\delta \geq 7$[74–78]. It was also shown that the reversal of flows depends on the sphere's amplitude, yet a specific scaling was not found[52,72–74]. Relating all this back to the spherobot, our data collapse gave $Re = A_r r/\delta^2$ as the critical parameter for the transition in swimming direction, a scaling that includes an amplitude dependence, as suggested by previous works. Moreover, we found that when plotting the dimensionless velocity of the spherobot as a function of r/δ, the transition in swimming ($Re \approx 20$) occurred in the range $r/\delta \approx [3.5, 7]$, (see Fig. 2.9[67]), again in agreement with previous reports on the reversal of SS flows for a sphere.

We can make an analogy that the large sphere of the spherobot acts like the body of the swimmer while the small sphere acts like the flagellum. In fact, it is really interesting that the SS flows, which are unrelated to the squirmer models, in the small-sphere leading regime resemble the flow field of Stokesian pullers and in the large-sphere leading regime resemble the flow field of Stokesian pushers[2,3,79]. However, the organisms that swim like pullers and pushers such as algae and bacteria, respectively, have different appendages in order to perform the "pulling" or the "pushing". What is remarkable here is that the geometry of the spherobot does not have to change – the small sphere can act as an effective flagellum that can both "pull" and "push" depending only on the critical parameter $Re = A_r r/\delta^2$. *E.g.* our swimmer can change its amplitude and it will switch swimming direction.

2.7 Conclusions

To conclude, we have proposed a model spherobot swimmer that utilizes SS in a novel way, to propel itself. The main findings of the current letter are (i) a transition in the swimming direction that collapses onto a single critical Reynolds number and (ii) the physical mechanism for the transition in swimming is the reversal of SS flows. Based on our findings, we propose that SS can be an important physical mechanism present more generally in motility at Re_{int} both in biological organisms but also when designing artificial swimmers[58,60,80,81]. Finally, we expect to find interesting emergent collective behavior of multiple spherobot swimmers as nonlinearities add up leading to different steady states and patterns.

2.8 Supplemental Information

2.8.1 Momentum flux calculations

To quantify the differences in flow in the two regimes, we calculated the time-averaged mass and momentum fluxes through upstream and downstream planes located at distance R above and below the spherobot (Fig. 2.6). At $Re = 3$, the fluid velocity was negative/positive in the planes above/below the spherobot. The reverse was true at $Re = 80$. In both cases, the momentum flux through the plane below the small sphere (red arrows) was greater than the momentum flux through the plane above the large sphere (i.e. the momentum flux of the stream below the small sphere is greater than the momentum flux of the stream above the large sphere).

2.8.2 Additional spherobot velocity data

Fig. 2.8 shows the velocity of the spherobot as a function of Re for different sphere sizes, R and r. Fig. 2.7 shows the velocity of the spherobot as a function of *Re* for a range of A, d_0, and ν with constant large sphere radius, R = 0.30m and small sphere radius, r = 0.15m. We have broken down Fig. 2.4 in the main text to explain how each of the parameters we vary affects the spherobot velocity.

As the spherobot's amplitude A increases, its velocity also increases, which makes intuitive sense; imagine being able to reach farther in a swim stroke (Fig. 2.7(b)(i),(ii)). In contrast, if the equilibrium distance d_0 increases, the spherobot's velocity decreases, which again makes intuitive sense if we consider a spherobot where the spheres are very far away from one another, *i.e.* $d_0 \to \infty$; the spheres oscillate independently, and there is no swimming (Fig. 2.7(a)(i),(ii)). Similarly, if the small sphere radius r increases or the ratio $\frac{r}{R} \to 1$, the velocity of the spherobot also decreases, showing that the more asymmetric the spherobot, the larger its swimming velocity (Fig. 2.8). Of course if the asymmetry is such that there is effectively only one sphere *e.g.* $R \to \infty$ or $r \to 0$ then again there is no swimming.

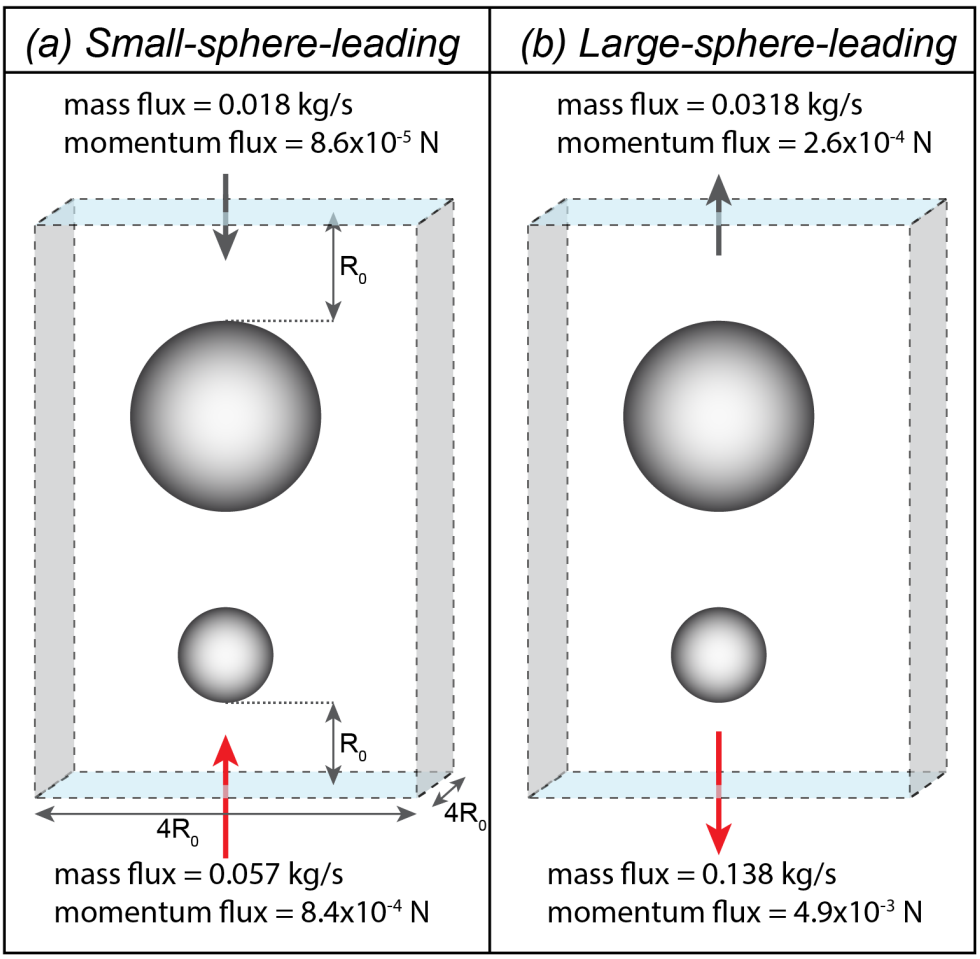

Figure 2.6: Momentum flux calculated upstream and downstream from the spherobot for (a) a representative small-sphere-leading case (Re=3) and (b) a representative large-sphere-leading case ($Re = 80$) ($R = 0.3$, $r = 0.15$, $A = 0.24$, $d_0 = 0.75$, 3D). The planes were $4R$ x $4R$ and located R above and below the spherobot (shown in light blue). Fluxes were time-averaged over a cycle after steady state had been reached.

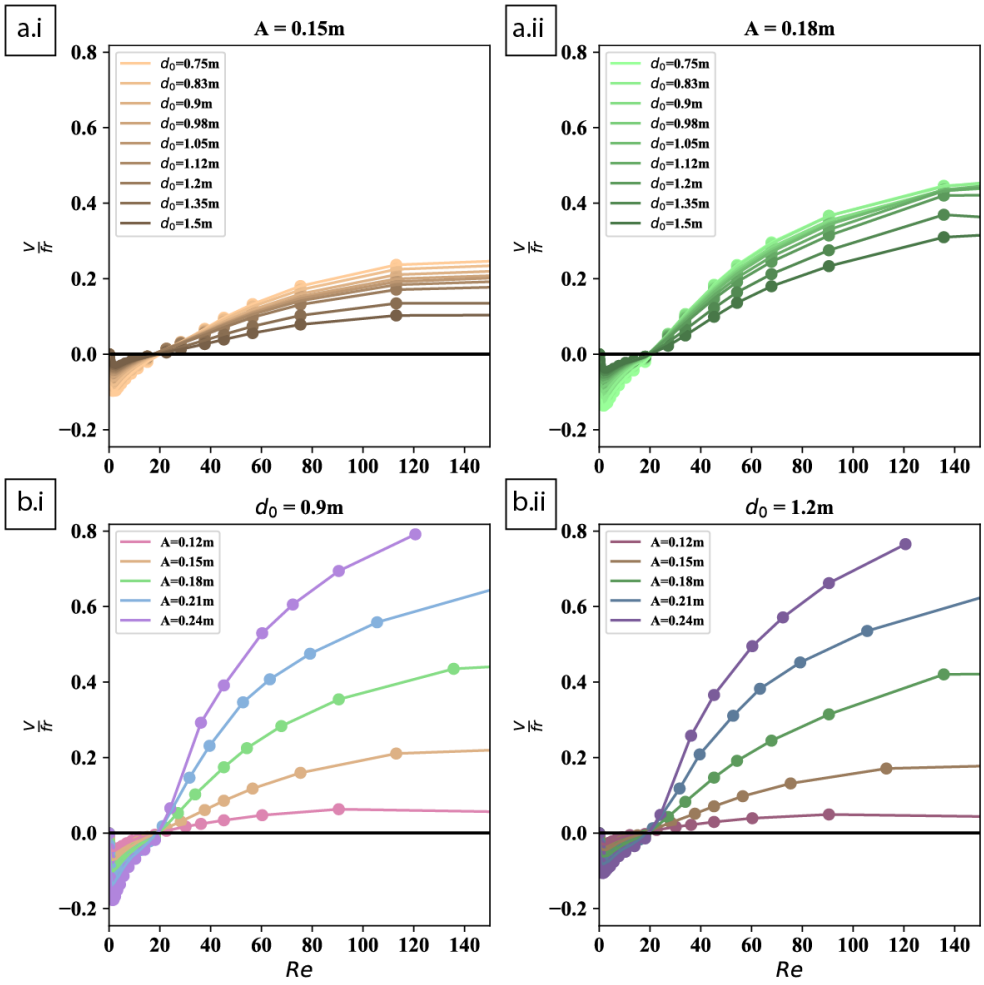

Figure 2.7: Velocity of the spherobot as a function of *Re* for a range of A, d_0, and ν with constant large sphere radius, R = 0.30m and small sphere radius, r = 0.15m (2D). Velocity of the spherobot for (a) a range of d_0 with constant A ((i) $A = 0.15m$ and (ii) $A = 0.18m$) and (b) a range of A with constant d_0 ((i) $d_0 = 0.9m$ and (ii) $d_0 = 1.2m$). At $0 < Re < 20$, the spherobot swims with the small sphere leading. At *Re*≈20, there is a switch in direction. At $Re > 20$ the spherobot swims with the large sphere leading. The spherobot does not swim in Stokes flow, $Re = 0$. (Line color indicates A and line saturation indicates d_0.)

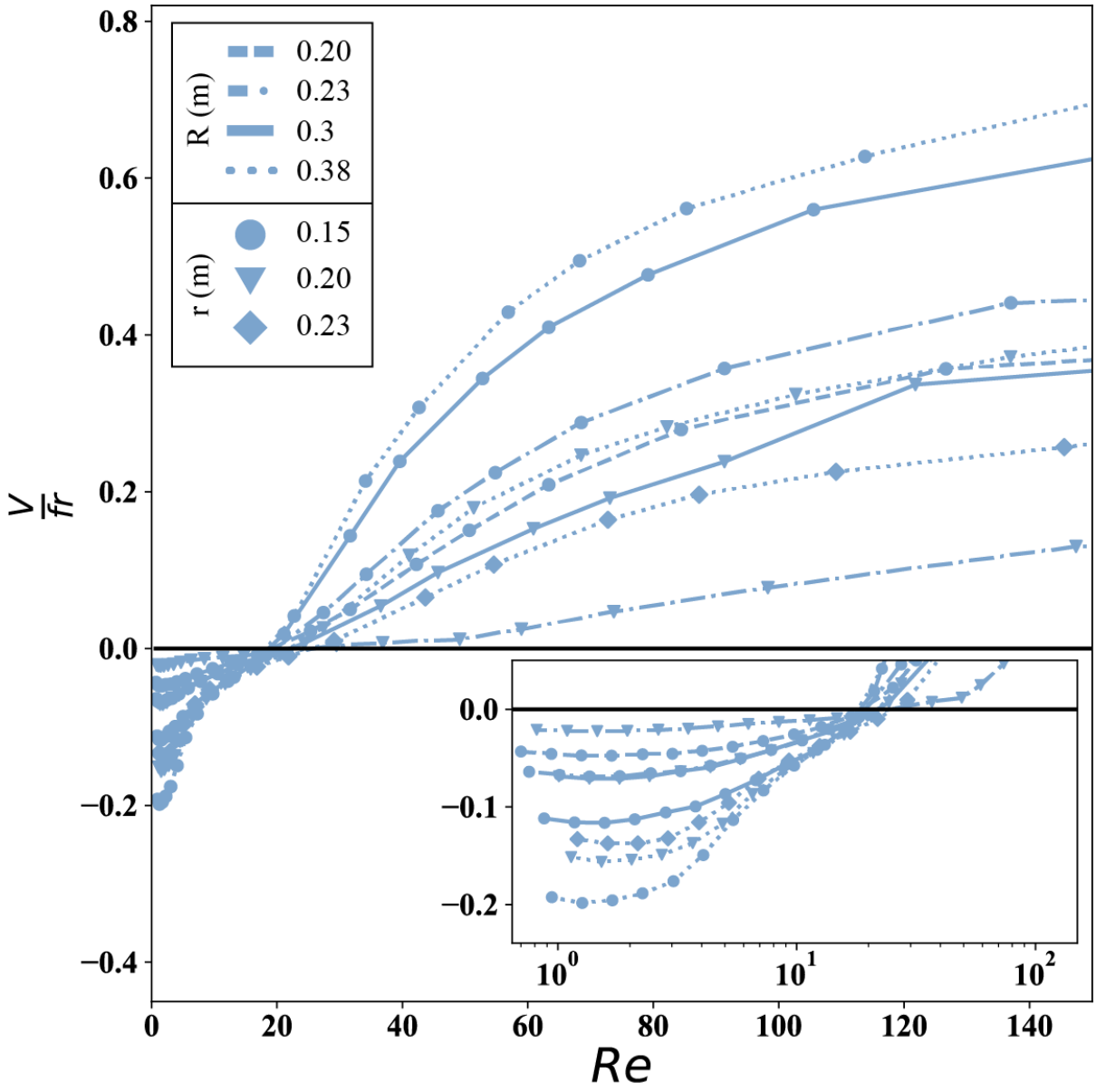

Figure 2.8: Velocity of the spherobot as a function of *Re* for a range of R, r, and ν with constant amplitude, A = 0.21m, and center-center distance, d_0 = 0.975m (2D). The radii used are shown in the legend. At $0 < Re < 20$, the spherobot swims with the small sphere leading. At *Re*≈20, there is a switch in direction. At $Re > 20$ the spherobot swims with the large sphere leading. Inset shows the small-sphere-leading regime plotted on a semi-log-x scale. (Line saturation indicates d_0, line style indicates R, and symbols indicate r.

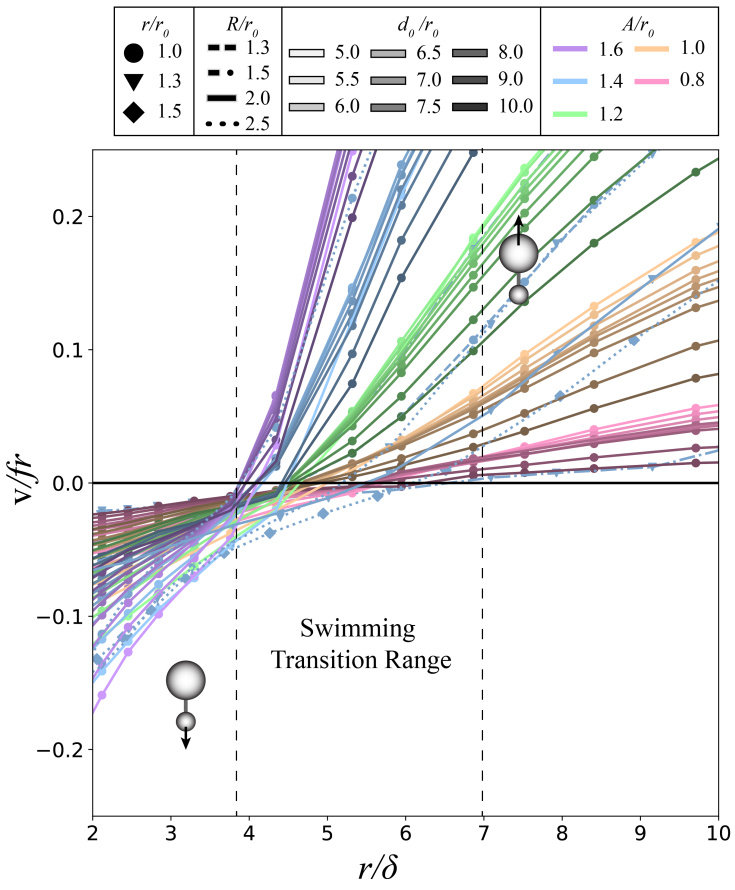

Figure 2.9: Velocity of the spherobot as a function of $\frac{r}{\delta}$. Swimming transition regime indicated by region in between vertical dashed lines. Negative velocity indicates swimming in the direction of the small sphere, positive velocity indicates swimming in the direction of the large sphere. Parameters A, d_0, R, and r are non-dimensionalized by the length scale $r_0 = 0.15$m, the most common radius of the small sphere. Line color indicates A, line saturation indicates d_0, line style indicates R, and symbols indicate r.

CHAPTER 3:
Kinematics of a simple reciprocal model swimmer at intermediate Reynolds numbers[1]

3.1 Overview

We computationally study the kinematics of a simple model reciprocal swimmer (asymmetric dumbbell) in a Newtonian fluid as a function of the Reynolds number (Re) and investigate how the onset and gradual increase of inertia impacts the swimming behavior: a reversal in the swim direction, flow directions, and the swim stroke. We divide the swim stroke into the increase and decrease in the distance between the two spheres, termed expansion and compression respectively, and relate them to power and recovery strokes. We find that the switch in swim direction also corresponds to a switch in power and recovery strokes. We obtain expressions for the mean swimming velocity by collapsing the net displacement during expansion and compression under power law relationships with respect to Re, the swimmer's amplitude, and the distance between the two spheres. Analyzing the fluid flows, we see the averaged flow field during expansion always resembles a pusher and compression always a puller, but when averaged over the whole cycle, the flow that dominates is the one that occurs during the power stroke. We also relate the power and recovery strokes to the swimming efficiency during times of expansion and compression, and we find that the power stroke is, surprisingly, not always more efficient than the recovery stroke. Our results may have important implications for biology and ultimately the design of artificial swimmers.

3.2 Introduction

Biological and artificial swimmers exist across a broad range of length scales, spanning from micron-sized bacteria and self-propelled nanoparticles to large aquatic organisms and marine robots on the order of meters. Swimming can be categorized by the Reynolds number (Re) which relates viscous and inertial forces. Microscopic swimmers at low Re, where viscosity dominates, swim differently than high-Re swimmers,

[1] This chapter previously appeared as an article in *Physical Review Fluids*. The original citation is as follows: Thomas Dombrowski and Daphne Klotsa, Kinematics of a simple reciprocal model swimmer at intermediate Reynolds numbers. *Phys. Rev. Fluids* **5**, 063103 (2020)

where inertia dominates. Indeed, in nature one can see bacteria swim with a corkscrew chiral flagellum at low Re, while larger fish undulate their bodies pushing fluid backwards to move forwards at high Re. Between the two extremes resides the intermediate Reynolds regime (Re $\approx 0.1 - 1000$), where both viscosity and inertia play a role. Mesoscopic organisms *i.e.* those that operate at intermediate Re are diverse both in size, $\approx$ 0.5mm - 50cm, and in swimming mechanisms, including for example jet propulsion of squid and jellyfish[4,5], rowing of copepod antennae[14,15], aquatic flapping flight of pteropods[11,82], anguilliform (eel-like) locomotion[6–10], and ciliate beating[12,13]. Understanding motility in fluids is important both for answering fundamental biological questions, such as how do organisms swim, feed, communicate, etc. but also for the design of artificial swimmers and flyers, such as marine robots and drones.

To gain insight into generic features and underlying physical mechanisms, simple theoretical models have been developed such as the scallop and Purcell's three-link-swimmer[34], the squirmer model[2,3,49,79], asymmetric and symmetric dumbbell swimmers[83–85], the three-sphere swimmer[86], and the push-me-pull-you swimmer[87]. Most of the models have focused on microscopic scales where inertia is negligible because: a) there are a lot of interesting biological questions and applications at microscopic scales, such as intracellular dynamics and processes in the cytoplasm, cell motility, bacteria, and algae[88], as well as artificial swimmers, such as self-propelled colloids and nanoparticles aspiring for example to aid in drug delivery[89,90]; and b) because Stokesian swimmers must break time reversibility, which makes their design theoretically challenging. While the Stokes regime is indeed very interesting, it is as important to understand what happens as we move away from the strict Re $= 0$ Stokes regime, when and how inertia kicks in, and its consequences for different kinds of swimmers (*e.g.* different geometries and motility mechanisms). Models that include finite inertia are the inertial squirmer[19–25], the flapping plate[26,27], and the asymmetric and symmetric dumbbell swimmers[28–32].

It is worth noting that a lot of biology takes place near the boundary between the Stokes and intermediate Reynolds regimes, yet where the boundary is precisely is generally unknown. Where the boundary is matters because organisms have to change their swimming mode, feeding strategy, etc. depending on the regime in which they live. Switching regimes is not unusual, in fact, a plethora of organisms born into the Stokes regime move out of it as they grow in size. We would expect that they also change the way they move as a result of this change in regime. For example, the mollusk *C. antartica* switches from using cilia to flapping as it grows[36], the brine shrimp transitions from rowing to gliding with metachronally-beating legs[91], and the nymphal mayfly transitions from rowing to flapping with its gill plates[92]. From an applications point of

view, understanding the physics near the boundary can help us design artificial swimmers or (microfluidic) processes that utilize the relative ratio of inertial and viscous forces, switching between regimes, and thus switching between desired properties. For a longer discussion on biology and applications at intermediate Re, see[1].

In this paper, we studied the kinematics of a simple reciprocal model swimmer as a function of the Reynolds number. The same asymmetric dumbbell model (termed the spherobot) was determined to switch swim direction depending on the Reynolds number because of the corresponding induced steady streaming flows[31]. The spherobot switched from a small-sphere-leading regime to a large-sphere-leading regime at $\mathrm{Re}_c \approx 20$. Here, we studied the motion of the spherobot swimmer in more detail by splitting its oscillation into the expansion and compression of the two spheres and collapsed their corresponding net displacements under piece-wise power law relationships with respect to Re, inverse Strouhal number ϵ, and equilibrium distance between spheres d_0. We also related the expansion and compression to power and recovery strokes. We found that the switch in swim direction as Re increased corresponded to a switch in the power and recovery strokes. In the small-sphere leading regime ($\mathrm{Re} < \mathrm{Re}_c$), the power stroke occurred during compression and the recovery stroke during expansion, while the reverse occurred in the large-sphere-leading regime ($\mathrm{Re} > \mathrm{Re}_c$). We noticed how as Re increased and inertial forces became more dominant, our swimmer transitioned from a jerky, back-and-forth motion with a large backward displacement during the recovery stroke in the small-sphere-leading regime to a continuous movement forward in the direction of swimming all in the same direction, with no backward displacement during the recovery stroke in the large-sphere-leading regime. By studying the fluid flows, we saw that the averaged flow field during expansion was always pusher-like and during compression puller-like, which is to be expected, but when averaged over the whole cycle one of the two flow fields dominated. We determined the most dominant flows consistently occurred during the power stroke in each regime. We also related the power and recovery strokes to the spherobot's efficiency during times of expansion and compression, and we found that the power stroke was, surprisingly, not always more efficient than the recovery stroke. The subtle differences in Re that can lead to switching regimes and swim strokes may have important implications for biology and ultimately the design of artificial swimmers.

The structure of the paper is as follows. In section II, we briefly describe the model, computational method, and simulation details. In section III we present results for the kinematics of the spherobot, section IV

for averaged fluid flows, efficiencies, and the evolution of fluid flow. We end with discussion and conclusions in section V.

3.3 Methods

The spherobot is a geometrically simple, reciprocal model swimmer composed of two unequally sized spheres of radii R and r, such that $R > r$ (asymmetric dumbbell), see Fig. 3.1(a) and refs[31,67]. The spheres oscillate in antiphase with respect to each other, and they are coupled to one another by prescribing the distance between their centers, $d(t) = d_0 + A\sin(2\pi ft)$, with an actuated spring, where d_0 is the equilibrium distance between the centers, A is the amplitude of the spherobot $A = 0.5(d_{max} - d_{min})$, and f is the frequency of oscillation, see Fig. 3.1(a). At each time step, the equilibrium distance of the actuated spring is updated, and an equal and opposite force is applied to each sphere to move them a desired distance, $d(t)$, apart. The magnitude and direction of the force applied to each sphere depends on the relative positions of the two spheres. $[F_R(t), F_r(t)] = [+, -]k(d(t) - x(t))$, in which F_R is the force applied to the large sphere, F_r is the force applied to the small sphere, k is a spring constant, and $x(t)$ is the current (actual) distance between the spheres. Note that $F_R = -F_r$ at every instance in time (*i.e.*, the swimmer is self-propelled). The prescribed distance between the spheres' centers changes sinusoidally with time, and the model ensures a geometrically reciprocal cycle (error $\approx 10^{-7}$ m). The model conditions ensure that the spherobot swims only along the oscillation axis (vertical). Since the forces were equal in magnitude and the spheres were of the same density, their amplitudes were different: $A_R < A_r$ and $A = A_R + A_r$. Subscripts R and r indicate quantities specific to the large and small sphere, respectively. Both spheres were neutrally buoyant with the surrounding fluid, *i.e.* they had equal densities $\rho_p = \rho_f = \rho$.

The spherobot was immersed in a viscous, incompressible Newtonian fluid that occupied a finite cell with no-slip walls. The fully-coupled fluid-structure interaction system was resolved using the Constrained Immersed Boundary (CIB) method[62,63]. The CIB scheme was implemented in IBAMR, which is an immersed boundary numerical method with adaptive mesh refinement[64,66]. The IB method for fluid-structure interaction uses an Eulerian formulation of the momentum equation and incompressibility constraint for the coupled fluid-solid system along with a Lagrangian description of the motion of the immersed structures. Let $\mathbf{x} \in \Omega$ be fixed Eulerian physical coordinates, and let $\mathbf{s} \in U^i$ be fixed Lagrangian curvilinear coordinates attached to the structure. In our notation, $\mathbf{X}(\mathbf{s}, t) \subset \Omega$ is the physical position of material point $\mathbf{s}$

(a)

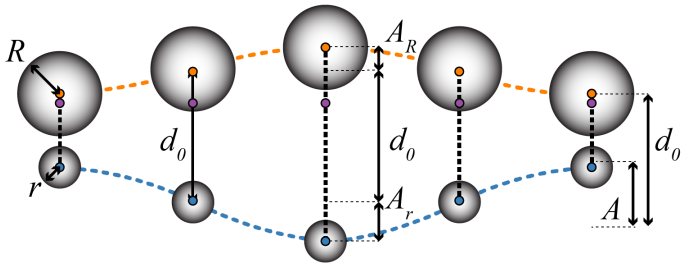

(b)

Simulation specs and parameters

Specifications	**Value**
Eulerian grid dimensions (m/r)	53.3×53.3
number of Eulerian grid levels	4
Eulerian grid refinement ratio	1:4
effective Eulerian grid resolution	512×512
time step size, Δt (s)	10^{-4}
Parameters	
Reynolds number, Re	$[10^{-3}, 150.0]$
sphere radii ratio, $\alpha = R/r$	2
amplitude, $\epsilon = A/r$	[0.8, 1.6]
frequency, f (s^{-1})	10
$M = r\sqrt{\omega/\nu} = r/\delta$	[0.88, 11.89]
equilibrium distance, $\hat{d}_0 = d_0/r$	[5.0, 10.0]

Figure 3.1: (a) Reciprocal oscillation of the spherobot swimmer over one cycle. The large sphere (orange) with radius R always oscillates in the opposite direction of the small sphere (blue) with radius r. The distance between the spheres $d(t) = d_0 + A\sin(2\pi ft)$ is prescribed to be of a simple harmonic oscillator with frequency f, where d_0 is the equilibrium distance between the spheres, and $A = A_r + A_R$ is the amplitude of the spherobot. The amplitude of the small and large spheres are A_r and A_R respectively. When absent of fluid, the spherobot's center of mass (CM), shown in purple, does not move throughout the oscillation. (b) Simulation specifications and parameters

at time t. The momentum equation and incompressibility constraint are given by

$$\rho\frac{D\mathbf{u}}{Dt}(\mathbf{x},t) = -\nabla p(\mathbf{x},t) + \mu\nabla^2\mathbf{u}(\mathbf{x},t) + \mathbf{f}(\mathbf{x},t), \tag{3.1}$$

$$\nabla\cdot\mathbf{u}(\mathbf{x},t) = 0, \tag{3.2}$$

in which $\mathbf{u}(\mathbf{x},t)$ is the material velocity field, $p(\mathbf{x},t)$ is the pressure field that imposes the incompressibility constraint, $\mathbf{f}(\mathbf{x},t)$ is a body force that arrises from the presence of the immersed structure, ρ is the mass density, and μ is the viscosity. Eulerian and Lagrangian variables are coupled via integral transforms with Dirac delta function kernels:

$$\mathbf{f}(\mathbf{x},t) = \int_U \mathbf{F}(\mathbf{s},t)\,\delta(\mathbf{x}-\mathbf{X}(\mathbf{s},t))\,\mathrm{d}\mathbf{s}, \tag{3.3}$$

$$\mathbf{U}(\mathbf{s},t) = \int_\Omega \mathbf{u}(\mathbf{x},t)\,\delta(\mathbf{x}-\mathbf{X}(\mathbf{s},t))\,\mathrm{d}\mathbf{x}\,. \tag{3.4}$$

Eq. (3.3) converts the Lagrangian force density $\mathbf{F}(\mathbf{s},t)$ (which is a Lagrange multiplier force that constrains the spheres to move as rigid bodies) to an equivalent Eulerian force density $\mathbf{f}(\mathbf{x},t)$, and Eq. (3.4) evaluates the local material velocity at each structural position.

The position of each sphere of the spherobot is updated via:

$$\frac{\partial \mathbf{X}}{\partial t}(\mathbf{s},t) = \mathbf{U}(\mathbf{s},t) \quad = \quad \mathbf{V}_{\text{COM}} + \mathbf{W}_{\text{COM}} \wedge \mathbf{R}(\mathbf{s},t), \tag{3.5}$$

in which $\mathbf{V}_{\text{COM}}$ and $\mathbf{W}_{\text{COM}}$ are the (unknown) translational and rotational velocities, respectively, and $\mathbf{R}(\mathbf{s},t) = \mathbf{X}(\mathbf{s},t) - \mathbf{X}_{\text{COM}}(t)$ is the radius vector to the center of mass of the sphere. The Lagrangian force density $\mathbf{F}(\mathbf{s},t)$ is required to satisfy the net external force and torque constraint on the immersed body:

$$\int_U \mathbf{F}(\mathbf{s},t)\,\mathrm{d}\mathbf{s} \quad = \quad \mathbf{F}_{\text{external}}, \tag{3.6}$$

$$\int_U \mathbf{R}(\mathbf{s},t) \wedge \mathbf{F}(\mathbf{s},t)\,\mathrm{d}\mathbf{s} \quad = \quad \mathbf{T}_{\text{external}}. \tag{3.7}$$

We remark that the net external force and torque on the immersed structure excludes hydrodynamic traction forces on the surface of the body, but could include forces and torques arising, for example, due to gravity, surface tension, tethered springs, etc. In the case of the spherobot, $\mathbf{F}_{\text{external}}$ is nonzero and results from the force applied by the actuated spring, and $\mathbf{T}_{\text{external}} = \mathbf{0}$ because the actuated spring passes through the centers of masses of the two spheres. There are no other external forces or torques.

In our computer model, each sphere of the spherobot was composed of a mesh of Lagrangian marker points that were generated using an in-house Python code, and the singular delta function kernels were replaced by a 6-point regularized kernel function[62]. The remainder of the spatial discretization and the time stepping algorithm for the CIB method have been described in detail in prior work[62,63].

An adaptive mesh is implemented to improve the efficiency of the simulation. The coarsest level is broken up into N=8 cells along one dimension. We use a grid refinement ratio of 1:4 where the next highest refinements are N=32, 128, and 512. There are 4 refinement levels, and the spherobot's mesh is evaluated at the highest grid refinement of N=512. The simulation box is 6$\times$ the length of the swimmer and it is 53$\times$ the radius of the small sphere to prevent interactions with the wall.

In previous work, we investigated the spherobot, which was shown to switch swim direction depending on a critical Re[31]. The swim direction was related to the reversal of steady streaming flows (SS) around the small sphere[38]. We note three important findings that are relevant in this paper too: 1) The steady streaming reversal of the time-averaged flow fields over a cycle was qualitatively similar to puller and pusher flow fields defined in Stokes flows, although these swimmers were at finite inertia and no assumptions were made on

the fluid flows; 2) we showed that steady streaming flows can be used as a propulsion mechanism, which is especially interesting in the low-intermediate Re < 20, where inertia is weak; and 3) Although the SS flows reversal is gradual as a function of Re, the result in a system like ours is a drastic change in behavior, namely change the direction of swimming.

Before we further discuss the spherobot, let us first consider the simpler problem of a single oscillating sphere with angular frequency ω, amplitude A, and radius r. As discussed in Lauga[19], in general, there are three relevant dimensionless ratios in this class of problems: the frequency (flapping) Reynolds number $\mathrm{Re}_f = rA\omega/\nu$ which scales with the non-linear advective term in the Navier-Stokes equations[19,93–95], $M^2 = r^2\omega/\nu$, which scales with the unsteady term in the Navier-Stokes equations[38], and the particle Reynolds number $\mathrm{Re}_p = \rho_p r^2\omega/\rho_f\nu$, which quantifies the particle inertia. Note that for us $\rho_p = \rho_f$ so the particle Reynolds number reduces to M^2. The oscillatory motion introduces a relevant length scale, the oscillatory boundary layer thickness, $\delta = \sqrt{\nu/\omega}$[96]. M can also be thought of as the ratio of the particle radius r to the oscillatory boundary layer thickness δ. An oscillating sphere also produces a nonzero cycle-averaged flow otherwise known as steady streaming, and there is an additional dimensionless ratio, the streaming Reynolds number $Re_s = A^2\omega/\nu$, which quantifies the steady streaming flows around a single oscillating sphere beyond the oscillatory boundary layer[38,39,52]. At intermediate Reynolds numbers, choosing which dimensionless ratio best characterizes the system is challenging because a lot of the parameters can have similar magnitudes, as is the case here. Thus, even for the simpler case of one oscillating sphere there are at least four relevant dimensionless ratios.

Additional complexity enters the system when we include a second sphere of different size oscillating antiphase, resulting in net motion, *i.e.* swimming. First, there are the extra length scales of the second sphere and of the whole swimmer, as well as the amplitude of the second sphere (apart from the ones stated above *i.e.* amplitude and radius of first sphere, distance between spheres, oscillatory boundary layer thickness). Second, there is a swimming Reynolds $\mathrm{Re}_{swim} = Ul/\nu$, where U is the swim velocity, and l the swimmer's length scale. It is worth noting that for experimentally relevant systems, many of these length scales (that enter the different dimensionless ratios) are of the same order of magnitude giving values for the ratios close to 1. As a result, the problem becomes more challenging and often analytically intractable[97].

Here, we use Re $= A_r r\omega/\nu$ as the reference Reynolds number (for simplicity the notation will be just Re) because that was the Re we found to determine the spherobot switch in swim direction from a small-sphere-leading regime (SSL) to a large-sphere-leading regime (LSL) in previous work[31]. Note that a

similar Re has been shown to dominate other intermediate-Re phenomena: the scaling of the stagnation point indicating the reversal of outer and inner steady streaming[53,76] and the gap between two granular spheres oscillating in phase[55,57].

We investigated the spherobot's movement in Stokes flow and in the range of $0.1 \leq Re \leq 150$. If we were to observe a dumbbell composed of a small sphere with radius r = 1mm and a large sphere with radius R = 2r = 2mm which swims in water and oscillates with a frequency f = 10Hz and amplitude A = r = 1mm, the Reynolds number would be in the intermediate range, Re = $2\pi f A_r r/\nu$ = 50.3. We defined the length scales with respect to the radius of the small sphere r and the time scales with respect to the frequency of the oscillation f. We introduced the dimensionless positions, velocities, equilibrium distance between spheres, and time

$$\hat{y} = y/r, \quad \hat{\mathrm{v}} = \mathrm{v}/fr, \quad \hat{d}_0 = d_0/r, \quad \tau = ft, \tag{3.8}$$

as well as the amplitude, kinematic viscosity, and large sphere radius

$$\epsilon = A/r, \quad M = r\sqrt{\omega/\nu} = r/\delta, \quad \alpha = R/r, \tag{3.9}$$

in terms of their dimensional counterparts. We performed a parameter sweep varying the fluid's kinematic viscosity M, the spherobot's amplitude ϵ, and the equilibrium distance between spheres $\hat{d}_0$, while keeping the spheres' radii R and r, frequency f, and sphere and fluid density ρ constant ($\alpha = R/r = 2$ and ρ = 2kg/m^3). All of the simulation parameters are shown in Fig. 3.1(b). The simulations were run long enough for the spherobot to reach a steady state, defined as less than a one percent change in the average velocity over consecutive oscillations. Data was acquired after steady state was reached. In most of the paper we focused on two characteristic systems, one in the small-sphere-leading regime at Re $= 2.5$ and one in the large-sphere-leading regime at Re $= 70.0$. For both systems, $\hat{d}_0$ = 6.5 and ϵ = 1.2. We used the software VisIt[65] for fluid flow analysis. Other analysis was done with in-house Python code. In the rest of the paper, we assume the spherobot is placed vertically (y-direction) with the large sphere on top and the small sphere at the bottom (as shown in Fig. 3.1). For all figures showing a characteristic cycle of oscillation, the data is shifted in the time axis in the following way. The first half of the cycle is a region of expansion, followed by a region of compression in the second half. We define $\tau = ft$ as our dimensionless time unit, essentially the fraction of time elapsed in the cycle. At $\tau = 0.00, 1.00$ the spheres are at minimum distance $\hat{d}_0 - \epsilon$, at $\tau = 0.50$ they are

Table 3.1: List of net displacements

Variable	Definition
$\Delta\hat{y}_{CM}$	center of mass
$\Delta\hat{y}_R$	large sphere
$\Delta\hat{y}_r$	small sphere
$\Delta\hat{y}_{exp}$	expansion
$\Delta\hat{y}_{com}$	compression
$\Delta\hat{y}_{min}$	shift in compression
$\Delta\hat{y}_+$	along $\langle\hat{\mathrm{v}}_{CM}\rangle$
$\Delta\hat{y}_-$	opposite to $\langle\hat{\mathrm{v}}_{CM}\rangle$

at maximum distance $\hat{d}_0 + \epsilon$, and at $\tau = 0.25, 0.75$ they are at their equilibrium distance apart $\hat{d}_0$. We use a number of variables to describe the net displacement of the spherobot during its cycle, as shown in Table 3.1.

3.4 Results

3.4.1 Kinematics

We first studied how the periodic oscillation of the two spheres, that composed the spherobot, resulted in net displacement of their combined center of mass (CM) over one cycle, $\hat{y}_{CM} = (\hat{y}_r m_r + \hat{y}_R m_R)/(m_r + m_R)$, where $\hat{y}$ indicates position along the swimmer's axis and m the mass of each sphere indicated by the subscript, for a range of Re (Fig. 3.2). Note that because of the unequal masses of the spheres, the CM is actually on the large sphere (see Fig. 3.1) and as such closely follows the trajectory of the large sphere. We used the CM to indicate the displacement and velocity of the spherobot as a whole. Moreover, displacement was measured in relation to the position of the CM at the start of the cycle at $\hat{y}_{CM} = 0$. The full parameter range of data shown in Table 1 is found in the SI. We present our findings where the spherobot's amplitude, $\epsilon = 1.2$, the equilibrium distance between spheres, $\hat{d}_0 = 6.5$, and the individual sphere radii, $\alpha = 2$, were held constant such that Re was only $\propto 1/\nu$. In other words, Re was increased gradually via the kinematic viscosity ν.

For Re $= 0$ (Stokes flow), the spherobot's reciprocal motion resulted in no net displacement over a cycle, as expected from the scallop theorem[34,84]. It moved in the direction of the large sphere during expansion, reaching maximum displacement half way through the cycle and then moved in the direction of the small sphere during compression, ultimately returning exactly where it began, see Fig. 3.2(a) black curve.

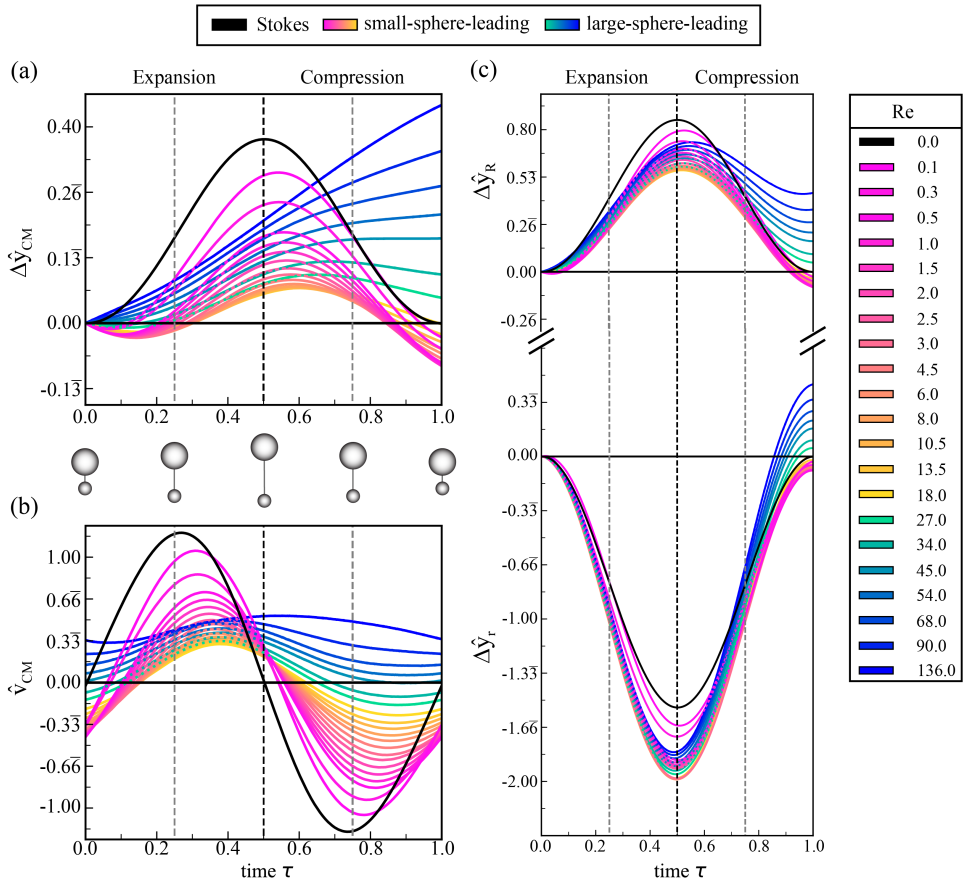

Figure 3.2: Kinematic quantities plotted as functions of time over one cycle of oscillation after steady state had been reached. (a) Displacement of spherobot, represented by the net displacement of its center of mass $\Delta\hat{y}_{CM}$, (b) velocity of spherobot represented by $\hat{\mathrm{v}}_{CM}$, and (c) displacement of individual spheres of radius R and r. Net swimming direction is indicated by the colors of the curves (black = Stokes flow, pink to yellow = small-sphere-leading, and green to blue = large-sphere-leading. The Reynolds number is represented by the shading of the curves, see legend.

3.4.1.1 Small-sphere-leading (SSL)

As we transitioned from Stokes flow to intermediate Re, the spherobot's trajectory changed, see Fig. 3.2(a) pink to yellow curves. At the start of its cycle, the spherobot moves forward (small sphere on the front), then slightly in the opposite direction during expansion and the initial part of compression; it moves with the small sphere on the front for the rest of the compression, with net displacement in that same direction at the end of the cycle. Note that the maximum displacement during the cycle is in the opposite direction to that of net swimming. This backward maximum displacement occurred at the half-period mark for Stokes flows and was shifted to a later time $\tau \approx 0.55 - 0.65$ in the small-sphere-leading regime. As Re increased both the maximum backward displacement near the half-period mark and the net displacement at the end of the cycle got smaller, see curves from Re=0.5 to Re=13.5, at $\tau \approx 0.5$ and $\tau = 1$, respectively. For Re=18.0, the net displacement after one cycle is ≈ 0. The spherobot will switch direction and transition from the small-sphere-leading to the large-sphere-leading regime.

3.4.1.2 Large-sphere-leading (LSL)

In the large-sphere-leading regime we see two behaviors, see Fig. 3.2(a) green to blue curves. First, for Re=27 and Re=34, at the start of its cycle, the spherobot moves backward slightly (small sphere on the front), and then moves forward (large sphere on the front) during expansion. It then continues to move forward during compression, only to slightly move back again at the end of the compression, with net displacement towards the large sphere. Already, it is clear that in the large-sphere-leading regime, the spherobot is hardly ever found to be with displacement in the opposite direction to its swimming, converse to the small-sphere-leading regime. Then, as Re increases further (Re > 45), the backward motion is suppressed more until the spherobot moves in the direction of swimming at all times. The two behaviors are more evident from the velocity plots, see Fig. 3.2(b) green curves, where for Re=27 and Re=34 the velocity at the start and the end of the cycle is negative (towards the small sphere), while for all other higher Re, the velocity is always positive (towards the large sphere).

3.4.1.3 Separate spheres

To understand how each sphere contributes to the overall motion, we also looked at the kinematics of the spheres separately, see Fig. 3.2(c). During expansion (compression), for both regimes the large sphere's

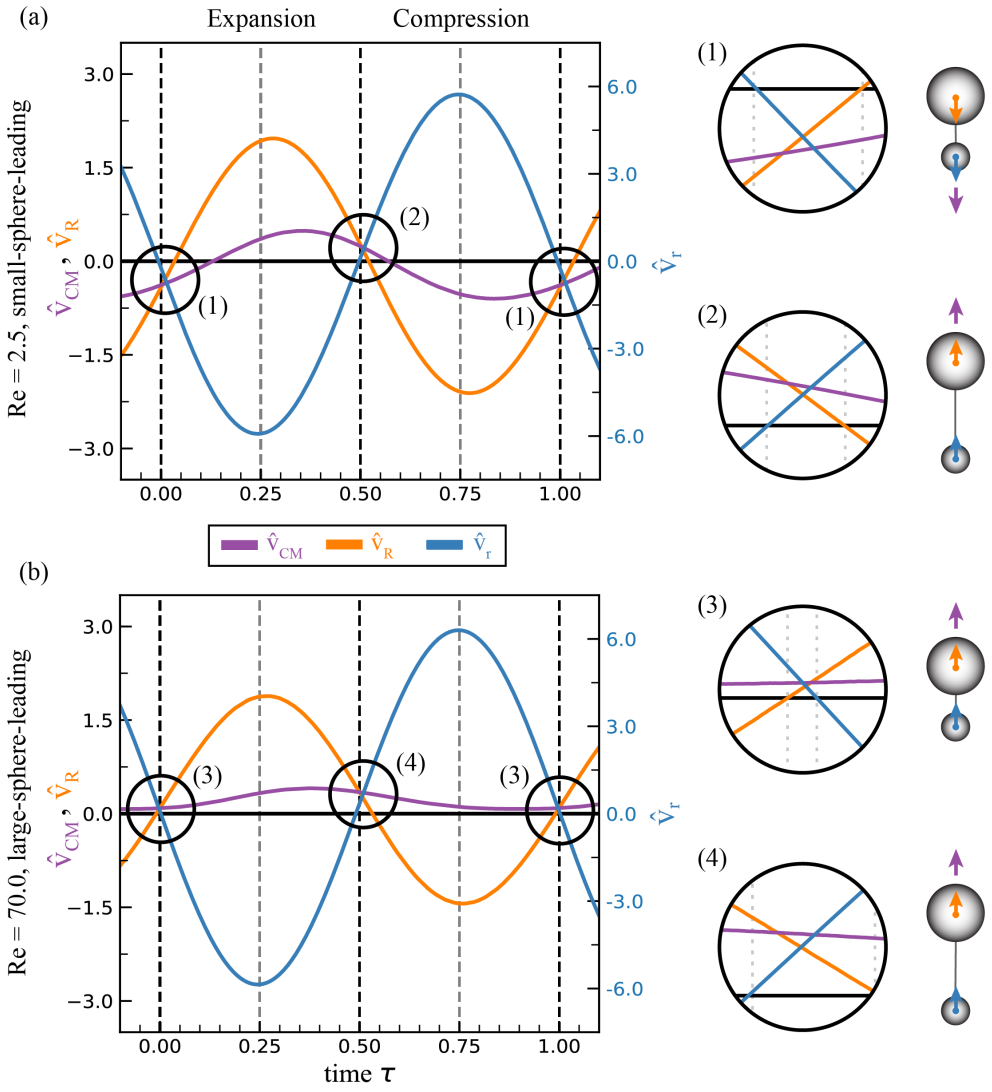

Figure 3.3: We define slip to be the region of movement where both spheres move in the same direction. As a result, the entire spherobot moves in the same direction as its spheres. Here, we show the non-dimensional velocities (v/fr) of the spherobot $\hat{v}_{CM}$ (purple), its large sphere $\hat{v}_R$ (orange), and its small sphere $\hat{v}_r$ (blue) when it is (a) small-sphere-leading and (b) large-sphere-leading. We identify the regions of slip observed during each spherobot's oscillation with black circles, and the region is magnified to the right. For the (a) small-sphere-leading spherobot, slip regions (1) and (2) are shown. (1) displays a region where slip is small-sphere-leading. It occurs at the end of compression and at the start of expansion. (2) shows a region where slip is large-sphere-leading. It occurs at the end of expansion and the start of compression. For the (b) large-sphere-leading spherobot, slip regions (3) and (4) are identified. (3) and (4) show regions where the spherobot slips large-sphere-leading. (3) occurs at the end of compression and the start of expansion. (4) occurs at the end of expansion and the start of compression.

net displacement $\Delta\hat{y}_R$ is always LSL (SSL), and the small sphere's $\Delta\hat{y}_r$ is always SSL (LSL). During compression, the large and small spheres do the opposite. The distinction in the trajectories of the two regimes seems to appear during compression.

In Stokes flow, the trajectory of each sphere is symmetric with respect to time over a cycle, and the two spheres are always antiphase. As we increase Re, the individual spheres are affected by the onset of inertia differently resulting in a phase difference between them. We present data for two characteristic systems (described in the Methods section), one in each regime. In Fig. 3.3, we compared the velocities of the large sphere (orange), small sphere (blue), CM (purple), and identified regions of "slip" to be when both spheres moved in the same direction. When both spheres' velocities are negative (toward the small sphere) we refer to SSL-slip and when they are both positive (toward the large sphere), we refer to LSL-slip. In the small-sphere-leading regime, at the end of expansion and the start of compression we found slip in the direction opposite to swimming (LSL-slip), while at the end of compression and the start of expansion we found a larger slip in the direction of swimming (SSL-slip), see Fig. 3.3(a). In the large-sphere-leading regime, at the end of expansion and the start of compression the slip was still LSL but now in the direction of swimming, while at the end of compression and the start of expansion we found that the direction of slip depended on the Re. As Re increased, the slip switched to LSL. In other words, the increase in inertia only affected the slip direction after compression. So, we identified for Re > 0.0 two contributions to the motion of the spherobot, the oscillatory and the slip (steady).

We also varied ϵ and $\hat{d}_0$ in addition to ν, shown in Fig. 3.2, the full parameter range shown in Table 3.1, and additional plots are included in the SI (section I). The magnitude of the net displacement at the end of the cycle increased when ϵ and Re also increased. Vice versa, the net displacement decreased when $\hat{d}_0$ increased (Fig. 3.9, 3.10).

To help identify trends in the data, we decomposed $\Delta\hat{y}_{CM}$ into the net displacements during expansion $\Delta\hat{y}_{exp}$ and during compression $\Delta\hat{y}_{com}$. Fig. 3.4(a,b) shows an example of this decomposition for all amplitudes and equilibrium distances studied. Let us consider expansion first. When the $\Delta\hat{y}_{exp}$ data is plotted on a log-log scale, see Fig. 3.4(a), we see a constant negative slope followed by a constant positive slope, indicative of two regions, each defined by a power law in Re. If we now consider compression and look at the data for $\Delta\hat{y}_{com}$ on a log-log scale, see Fig. 3.4(b), we observe three distinct trends with respect to Re all with positive slopes, also determined to be power laws with different exponents. We considered three variables Re, $\epsilon = A/r$, and $\hat{d}_0$ and assume they are independent of one another. We partitioned the data

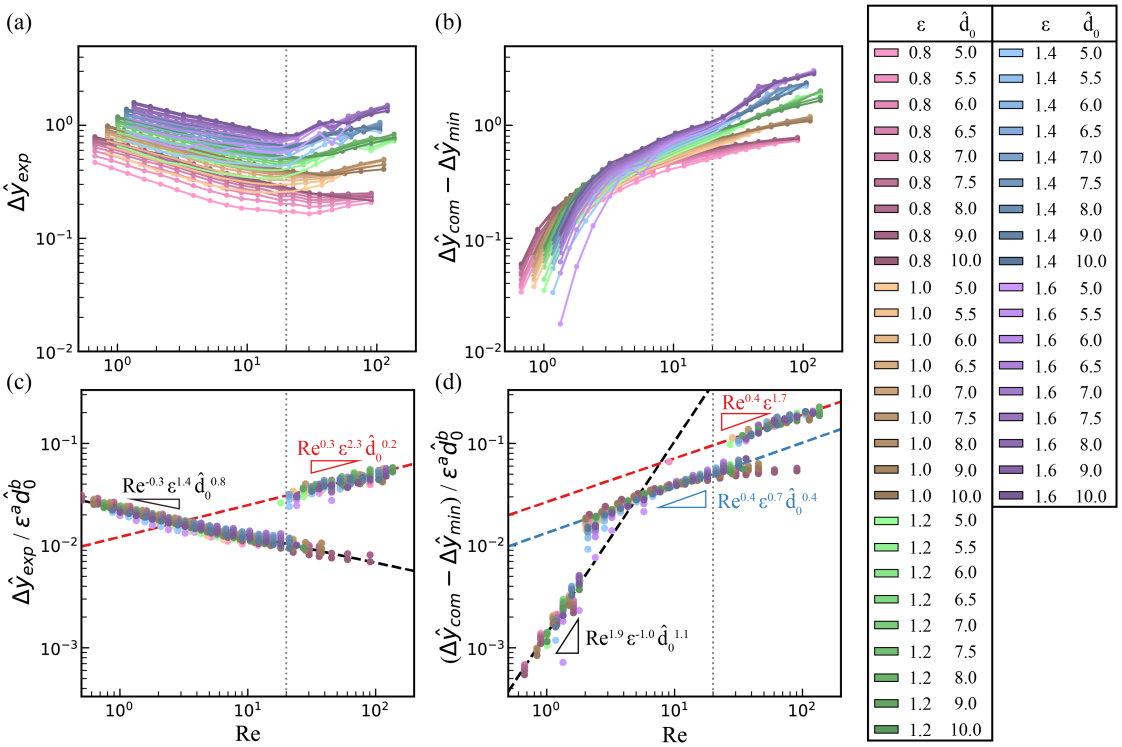

Figure 3.4: (a) Net displacement of the spherobot during expansion $\Delta\hat{y}_{exp}$ as a function of Re on a log-log scale for all ϵ and $\hat{d}_0$ simulated, see legend. Curves show a constant negative slope followed by a positive slope except for when both $\epsilon = 0.8$ (pink) and $\hat{d}_0 = 9.0, 10.0$. The turning point and the positive slope change for different amplitudes ϵ (color). (b) Net displacement of the spherobot during compression $\Delta\hat{y}_{com}$ as a function of Re on a log-log scale. There are three distinct positive slope trends with Re. We fit the expansion and compression displacements with respect to Re, ϵ, and d_0 using a multiple variable linear regression. (c) $\Delta\hat{y}_{exp}$ vs. Re on a log-log scale collapsed into a negative slope (black dashed) and a positive slope region (red dashed). (d) $\Delta\hat{y}_{com}$ vs. Re on a log-log scale collapsed into three distinct positive slope regions. The corresponding relationships with Re, ϵ, and d_0 are also shown in (c) and (d). The dotted grey line represents the critical Reynolds number where the swimming direction switches from small-sphere-leading to large-sphere-leading.

into two expansion regions and three compression regions with Re, and performed a multiple variable linear regression on each. It is important to note that each region has a different dependence on Re, ϵ, and $\hat{d}_0$. For the expansion, the data was split where there was a minimum in $\Delta\hat{y}_{exp}$, see Fig. 3.4(a). For compression, the data was split where the slope changed at Re ≈ 2.0 and then again when $\Delta\hat{y}_{exp}$ was at a minimum (the same criterion as the expansion data), see Fig. 3.4(b). The resulting collapse is shown on a log-log scale in Fig. 3.4(c,d). Equations (3.10) and (3.11) show the fits for $\Delta\hat{y}_{exp}$ and $\Delta\hat{y}_{com}$, respectively, and their power law relationships with Re, ϵ, and $\hat{d}_0$. It is worth noting that while there is currently no analytical theory for finite amplitudes, the expressions we obtained from the collapse can be used to give a prediction for the velocity of the spherobot, $\langle \hat{\mathrm{v}}_{CM} \rangle = f(\Delta\hat{y}_{exp} + \Delta\hat{y}_{com})$, where f is the frequency of its oscillation.

$$\Delta\hat{y}_{exp} = \begin{cases} 10^{-1.6}\mathrm{Re}^{-0.3}\epsilon^{1.4}\hat{d}_0^{0.8} & \text{Fig. 3.4(c) Black} \\ 10^{-1.9}\mathrm{Re}^{0.3}\epsilon^{2.3}\hat{d}_0^{0.2} & \text{Fig. 3.4(c) Red} \end{cases} \tag{3.10}$$

$$\Delta\hat{y}_{com} = \begin{cases} 10^{-2.9}\mathrm{Re}^{1.9}\epsilon^{-1.0}\hat{d}_0^{1.1} & \text{Fig. 3.4(d) Black} \\ 10^{-1.9}\mathrm{Re}^{0.4}\epsilon^{0.7}\hat{d}_0^{0.4} & \text{Fig. 3.4(d) Blue} \\ 10^{-1.6}\mathrm{Re}^{0.4}\epsilon^{1.7} & \text{Fig. 3.4(d) Red} \end{cases} \tag{3.11}$$

3.4.2 Power and recovery

To gain insight into the spherobot's motility mechanism in the two regimes, we divided its periodic motion into power and recovery strokes, a classical analysis for the motility of Stokesian swimmers[41]. In living organisms, a common way to define power and recovery strokes is as follows. The power stroke occurs when the swimmer's appendage, *i.e.* the part of the swimmer that generates motion, moves opposite to the direction of the mean swim velocity $\langle \hat{\mathrm{v}}_{CM} \rangle$, and the recovery stroke occurs when the appendage moves in the same direction as $\langle \hat{\mathrm{v}}_{CM} \rangle$[98,99]. For example, one can imagine a human swimmer's breast stroke. The power stroke occurs when the swimmer's arms move back to propel the swimmer forward, and the recovery stroke occurs as the arms return to their original position. During the recovery stroke, the swimmer either moves backwards or slows down depending on the motility mechanism, Re, etc. It is also important to note that organisms with reciprocal strokes (stroke same forwards in time as backwards) cannot swim in Stokes

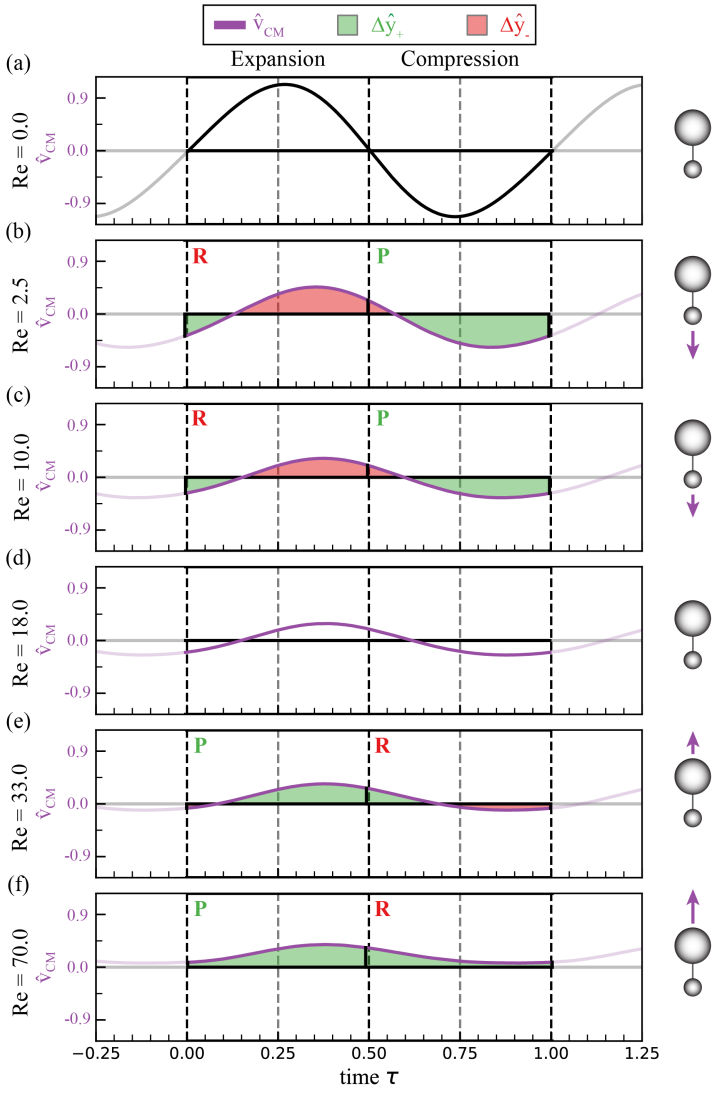

Figure 3.5: The power and recovery stroke of the spherobot is determined by the movement of its appendage, the small sphere, represented by $\hat{v}_r$. We define the power stroke to be when the small sphere moves opposite to the direction of net motion, $\hat{v}_r\langle\hat{v}_{CM}\rangle < 0$. Vice versa, the recovery stroke is defined to be when the small sphere moves in the same direction as the net motion, $\hat{v}_r\langle\hat{v}_{CM}\rangle > 0$. In this figure, the non-dimensional velocity of the spherobot, $\hat{v}_{CM}$, is represented by the purple curves. The mean swim direction $\langle\hat{v}_{CM}\rangle$ is indicated by the purple arrow in the accompanying spherobot schematics. The shaded areas under the $\hat{v}_{CM}$ curve represent the displacements: in the mean swimming direction $\Delta\hat{y}_+$ (green) and opposite to it $\Delta\hat{y}_-$ (red). The power and recovery strokes for each swimmer are labeled by P and R, respectively. (a) The spherobot in Stokes flow. Here, there is zero net displacement. Therefore, there is no power or recovery stroke observed. (b) and (c) The spherobot swims net small-sphere-leading at Re=2.5. Its power stroke is during compression, and its recovery stroke is during expansion. (d) The spherobot does not swim and its net displacement is very small and approximated to be zero. Like Stokes flow, we do not observe a power or recovery stroke. (e) and (f) The spherobot swims large-sphere-leading at Re=33.0 and Re=70.0. Its power and recovery stroke are opposite of those observed for the small-sphere-leading spherobot. The power stroke occurs during expansion, and the recovery stroke occurs during compression.

flow meaning the power stroke is identical to the recovery stroke and the swimmer moves back and forth the same amount *i.e.* the scallop or the spherobot.

How does a power and recovery stroke emerge as Re increases from 0 to finite? And how do the notions of power and recovery strokes evolve as Re increases further? We aim to answer these questions for the spherobot. We view the large sphere as the body of the swimmer and the small sphere as its appendage. The justification of this is that the small sphere moves the most as it has a larger amplitude than the large sphere, see also[31]. Thus, we define the power stroke to be when the velocity of the small sphere and the average velocity of the CM over the whole cycle are in opposite directions $\hat{\mathrm{v}}_r\langle\hat{\mathrm{v}}_{CM}\rangle < 0$ and the recovery stroke when the velocity of the small sphere and the average velocity of the CM are in the same direction $\hat{\mathrm{v}}_r\langle\hat{\mathrm{v}}_{CM}\rangle > 0$. Note that $\langle\hat{\mathrm{v}}_{CM}\rangle < 0$ in the small-sphere-leading regime and $\langle\hat{\mathrm{v}}_{CM}\rangle > 0$ in the large-sphere-leading regime.

In Fig. 3.5, we plot $\hat{\mathrm{v}}_{CM}$ (purple), the displacements in the same direction as $\langle\hat{\mathrm{v}}_{CM}\rangle$ termed $\Delta\hat{y}_+$ (green area) and opposite to it $\Delta\hat{y}_-$ (red area), and indicate power (P) and recovery strokes (R) in each regime. For $\mathrm{Re} = 0.0$, there was no distinction between power and recovery strokes because the spherobot does not swim $\langle\hat{\mathrm{v}}_{CM}\rangle = 0.0$, Fig. 3.5(a). Connecting to the two regimes, in the small-sphere-leading regime, Fig. 3.5(b), the spherobot performs a power stroke during compression and a recovery stroke during expansion. The effect of inertia is already apparent: the curve has shifted in the time axis compared to Stokes flow, such that, early in the recovery stroke, the swimmer is still moving forward due to the power stroke. Similarly the swimmer is still moving backward early in the power stroke. As Re increases, the power and recovery strokes produce smaller displacements in both directions, see Fig. 3.5(c). As a result, the spherobot experiences less intense back-and-forth motion. Note that we do not see a further shift with respect to time. At the critical value where the transition in the swimming direction occurs ($\mathrm{Re} = 18.0$), expansion and compression generate smaller but equal displacements in both directions; so the spherobot remains stationary over a cycle, see Fig. 3.5(d). As Re increases further, the spherobot switches direction to swim large-sphere-leading, and now performs a power stroke during expansion and a recovery stroke during compression, Fig. 3.5(e,f). Its periodic motion is still prescribed and does not change, but the power and recovery strokes reverse. There is also a behavioral change in the recovery stroke. When $\mathrm{Re} > 18$ but still close to the transition, the recovery stroke produces a backwards displacement (Fig. 3.5(e)), while for higher Re the recovery stroke does not produce a backward displacement and just slows down the swimmer (Fig. 3.5(f)). The power stroke, on the other hand, does not change much with Re and the maximum velocity remains approximately constant. This is a demonstration

showing how the movement of a simple model swimmer is affected by the onset and gradual increase of inertia.

3.5 Fluid Flows and Efficiency

We, previously, showed that in the small-sphere-leading regime the averaged flow over a cycle is puller-like *i.e.* the flow is pulled in toward the spheres along the swimming direction and is pushed out along the perpendicular, see Fig 3.6(c), while in the large-sphere-leading regime, the averaged flow over a cycle is pusher-like *i.e.* the flow is pushed out away from the spheres along the swimming direction and is pulled in along the perpendicular, see Fig 3.6(f)[31]. We related this reversal of averaged fluid flows of the spherobot to a reversal in steady streaming around a sphere calculated analytically by Riley[38]. It is noteworthy that while the spherobot operates at intermediate Reynolds numbers and the flow around it is generated by the oscillation of the spheres, its average flow field qualitatively resembles the flow around Stokesian model pullers and then pushers as Re increases and the flow field of the spherobot reverses. As discussed more in Dombrowski *et al.*[31], there is no reason to assume that such a link would exist because the source of the flow field and the hydrodynamics are different in the two cases: surface velocity oscillations at Re$= 0$ in the squirmer model versus translational sphere oscillations at intermediate Re in the spherobot.

To get more insight into how the averaged fluid flow fields' reversal relates to motion, we split the flows averaging over expansion and compression separately for the two characteristic systems. The averaged flow during expansion resembles a pusher and during compression a puller for both swimming regimes. This makes intuitive sense as we expect the fluid to flow into the gap between the spheres during expansion and to be pushed out of the gap during compression. There is a competition between pusher and puller type flow, and depending on Re, either puller or pusher flow is more dominant, as evident by the difference in net flow fields (c) and (f).

The presence of both puller- and pusher-like flows during the cycle for both small-sphere leading (puller-like overall) and large-sphere-leading (pusher-like overall) regimes is interesting because it apparently happens around living organisms too, albeit in Stokes flows. *Chlamydomonas* and sperm cells, for example, have been shown to oscillate between puller and pusher flows even though they are classified as a puller and pusher respectively based on the net far field flow[100]. Relating to power and recovery strokes in each regime, it is worth noting that the flow field that occurs during the power stroke is the one that dominates

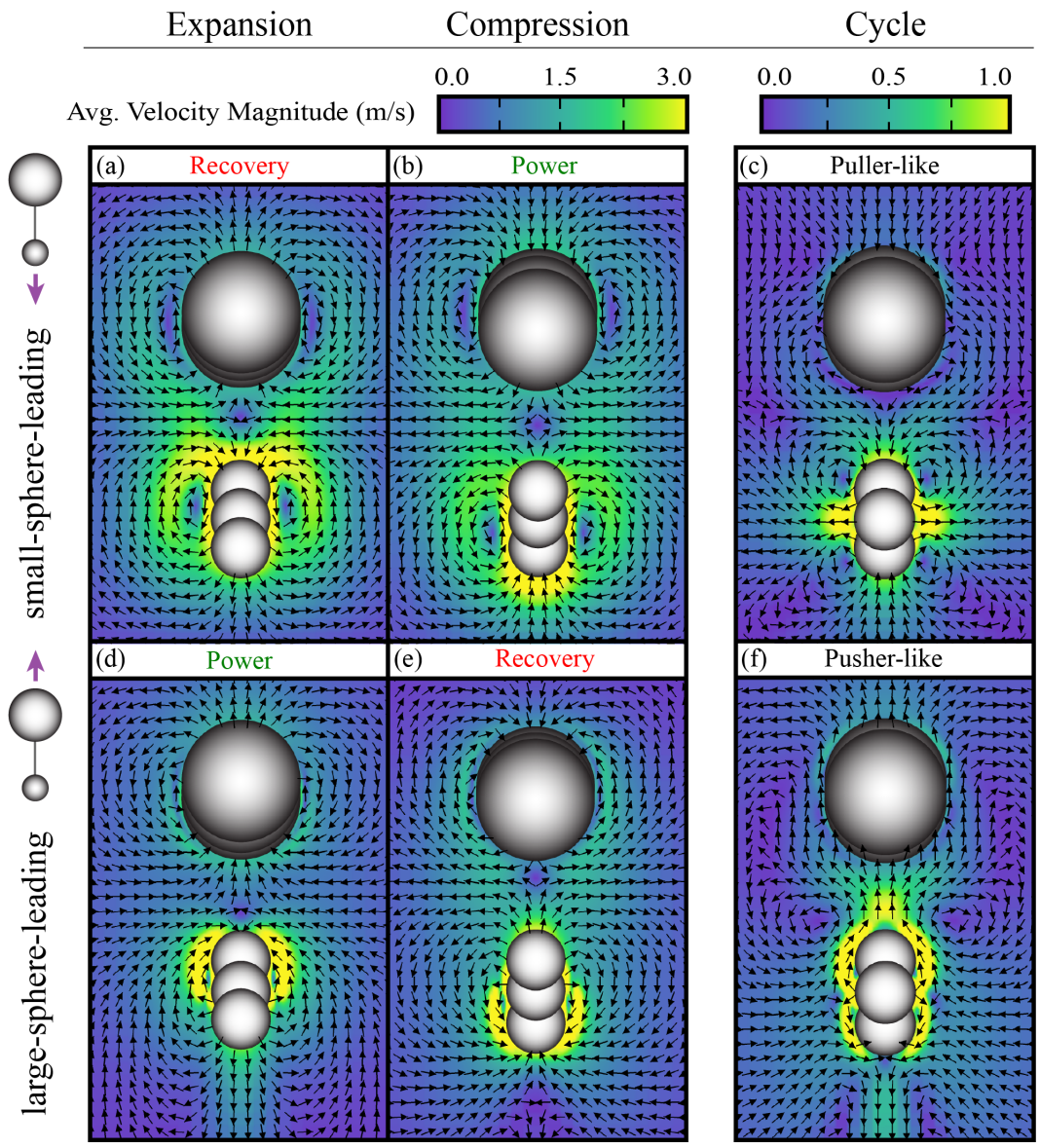

Figure 3.6: The average velocity field of a small-sphere-leading (top row) and large-sphere-leading (bottom row) spherobot averaged over (left) expansion, (middle) compression, and (right) an oscillation cycle. Flow magnitudes are represented by the heat map, and the flow direction is indicated by the black arrows. (a) Flow field of small-sphere-leading spherobot averaged over expansion. The fluid flows outward along the swimming axis and inward perpendicular. (b) Flow field of small-sphere-leading spherobot averaged over compression. The flow is opposite to that of expansion, inward along the swimmer's axis and outward perpendicular. (c) Averaged over a whole cycle small-sphere-leading spherobot flow. The net flow is puller-like. (d) Flow field of large-sphere-leading spherobot averaged over expansion. The fluid flows outward along the swimming axis and inward perpendicular. (e) Flow field of large-sphere-leading spherobot averaged over compression. The flow is opposite to that of expansion, inward along the swimmer's axis and outward perpendicular. (f) Averaged over a whole cycle large-sphere-leading spherobot flow. The net flow is pusher-like.

over the cycle, see Fig. 3.6. Note that we are presenting the near-field flow here, which extends to the edge of the box $\sim 53r$. It will be interesting to do a systematic study of the near and far-field flow and how they decay, and compare for example with the fields shown in Chisholm and Khair for inertial squirmers[24].

We also calculated the efficiency of our swimmer in each regime during expansion η_{exp}, compression η_{com}, and the whole cycle η_{cyc}. We defined the efficiency to be $\eta = \Delta y_+/E$. Δy_+ is the swimmer's total distance traveled in the net swimming direction and $E = \sum_{\tau=0}^{1} U_{spring}(\tau) = \sum_{\tau=0}^{1} 0.5k(d(\tau) - x(\tau))^2$ is the total energy added to the system over one cycle, where k is the spring constant, $d(\tau)$ is the prescribed spring length and $x(\tau)$ is the current spring length in the simulation (see also section II). There was zero contribution to the efficiency when the spherobot moved opposite to its swim direction. In Fig. 3.7, we calculated the efficiency of the spherobot with parameters $A = 0.18$m and $d_0 = 0.98$m and plotted as a function of Re. In the small-sphere-leading regime, the spherobot was more efficient during compression (green dotted line) than expansion (red solid line), $\eta_{com} > \eta_{exp}$, *i.e.* it was more efficient to push fluid out from between the spheres than to pull it in. In the large-sphere-leading regime, expansion (green solid line) was more efficient than compression (red dotted line), $\eta_{exp} > \eta_{com}$ *i.e.* it was more efficient to pull fluid in between the spheres than to push it out. For most Re, the power stroke is more efficient than the recovery stroke. However, at Re ≈ 110 for this spherobot configuration, the recovery stroke becomes more efficient than the power stroke. In fact, the Re where the recovery stroke becomes more efficient than the power stroke depends on the separation distance of the spheres, $\hat{d}_0$. The larger the separation, the larger the Re where the recovery becomes the more efficient stroke, see Fig. 3.19. We discuss possible explanations in the SI.

We can accredit the motion of the spherobot to the continuous evolution in its averaged fluid flow over a cycle (steady streaming) across Re, see Fig. 3.8. First, at low Re, Fig. 3.8(a), the spherobot oscillations generate only one vortex layer. The flow pulls inward along the swimming axis and pushes outward along the perpendicular, see also Fig. 3.6(c). Because of the asymmetry in the spherobot, there is a resulting asymmetry in fluid flow. The small sphere has a larger amplitude so its oscillation affects the surrounding flow farther away than the large sphere does. In fact, steady streaming flows theoretically scale as $A^2\omega/\nu$[39]. Thus the averaged flow appears to be dominated by the small sphere so much that the large sphere acts almost as an obstacle. As a result, at the lower end of Re, the spherobot moves small-sphere-leading because the fluid below the small spheres pulls it more than fluid above. As Re increases, the inner vortex layer reduces in size and extent, and eventually an additional outer vortex layer forms only below the small sphere, see Fig. 3.8(b). The outer vortex layer rotates counter to the inner vortex which creates a competition between pulling the

spherobot down and pushing the spherobot up along its swimming axis (stagnation point). The spherobot slows down and approaches zero. An outer vortex layer above the large sphere develops at a higher Re relative to the outer vortex below the small sphere *i.e.* Fig. 3.8(c). When the spherobot is stationary at $\mathrm{Re} = \mathrm{Re}_c$, the inner vortex pulls the spherobot as strong as the outer vortex pushes it. As Re increases further, Fig. 3.8(d), the outer vortex above the large sphere aligns its rotation with the outer vortex above the small sphere and it disappears. The small sphere's outer vortices become more and more dominant, and the spherobot is pushed up more by the fluid below the small sphere. The inner vortex becomes smaller, $\delta = \sqrt{\nu/\omega}$, and as a result the spherobot becomes more efficient in swimming large-sphere-leading. Thus, here is another example where we see how the spherobot's movement is due to a competition between pushing and pulling.

3.6 Discussion

To summarize, we explored the spherobot's kinematics and its relationship with Re, amplitude ϵ, and the equilibrium distance between spheres $\hat{d}_0$ by collapsing the net displacements during expansion $\Delta\hat{y}_{exp}$ and during compression $\Delta\hat{y}_{com}$. In the small-sphere-leading regime, the spherobot performed a back-and-forth motion where it moved more in the direction of swimming during compression than in the opposite direction during expansion. The backwards motion disappeared as Re increased and the spherobot moved in the direction of swimming during expansion and slowed down during compression. We categorized the spherobot's swimming into power and recovery strokes. The swim stroke itself did not change, however, due to the change in swim direction, the power and recovery strokes switched. We looked at the individual sphere's velocities and identified regions of slip where both spheres and the spherobot's CM moved in the same direction. We noticed the slip direction at the end of the power stroke was always in the same direction as the net swimming. We analyzed the flow fields for a small-sphere-leading and large-sphere-leading spherobot. Much like living organisms, there was a competition between puller and pusher type flow throughout the cycle. When averaged over the whole cycle, the flow that dominated was the one that occurs during the power stroke. We calculated the efficiencies of the spherobot over the cycle as well as during expansion and compression separately. We determined that in the small-sphere-leading regime, it was more efficient to push fluid out of the gap between the spheres than to pull fluid inward; the opposite was true for most Re in the large-sphere-leading regime. There was additional complexity in the efficiency in the large-sphere-leading

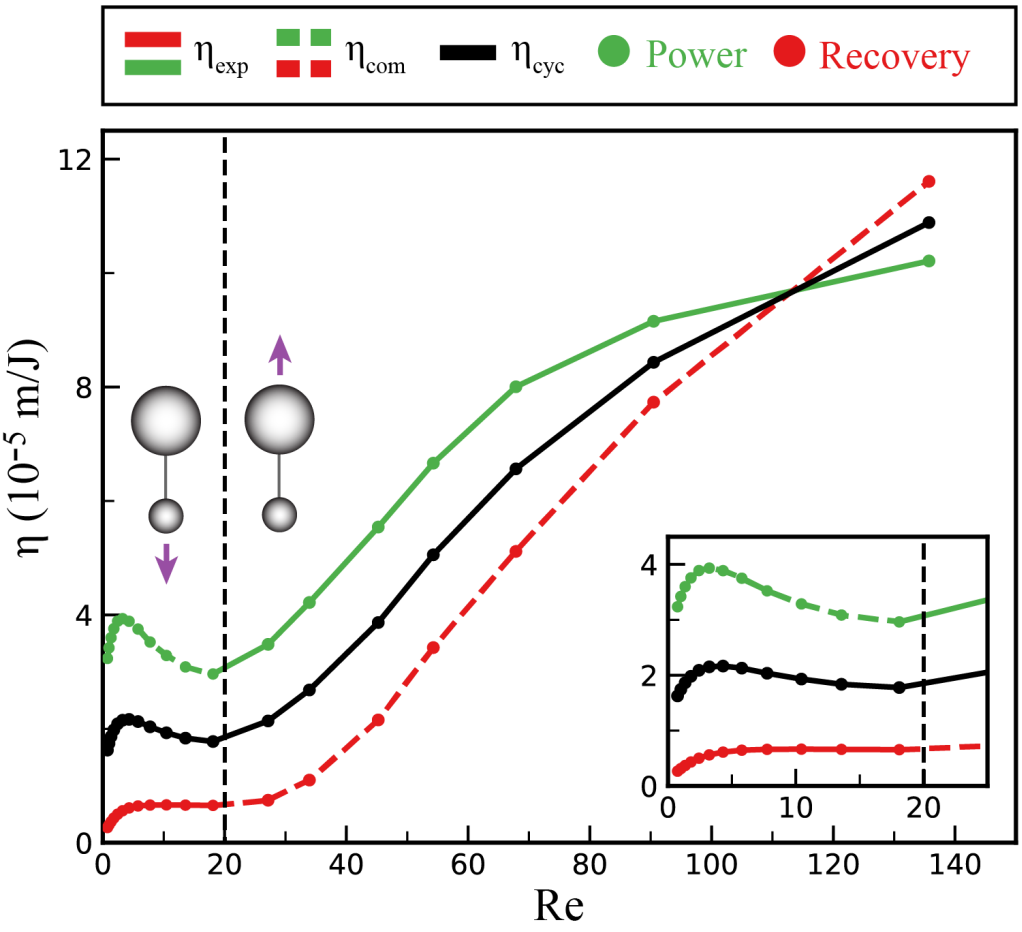

Figure 3.7: Efficiency of a spherobot with parameters $\epsilon = 1.2$ and $\hat{d}_0 = 6.5$ as a function of Re where η_{exp} (solid green and red), η_{com} (dashed green and red), and η_{cyc} (black) are depicted. Also shown are the efficiencies of the power (green) and recovery (red) strokes. The inset shows a close up of the efficiencies in the small-sphere-leading regime. Here, the power stroke occurs during compression, the recovery stroke during expansion, and $\eta_{com} > \eta_{exp}$. Because there is a switch in swimming direction at Re ≈ 20, the power and recovery strokes also switch. Now, $\eta_{exp} > \eta_{com}$. As expected, the power stroke is more efficient than the recovery, but up until Re > 110 for this configuration. There is also a trend in the spherobot's cycle efficiency where swimming large-sphere-leading is generally more efficient than swimming small-sphere-leading.

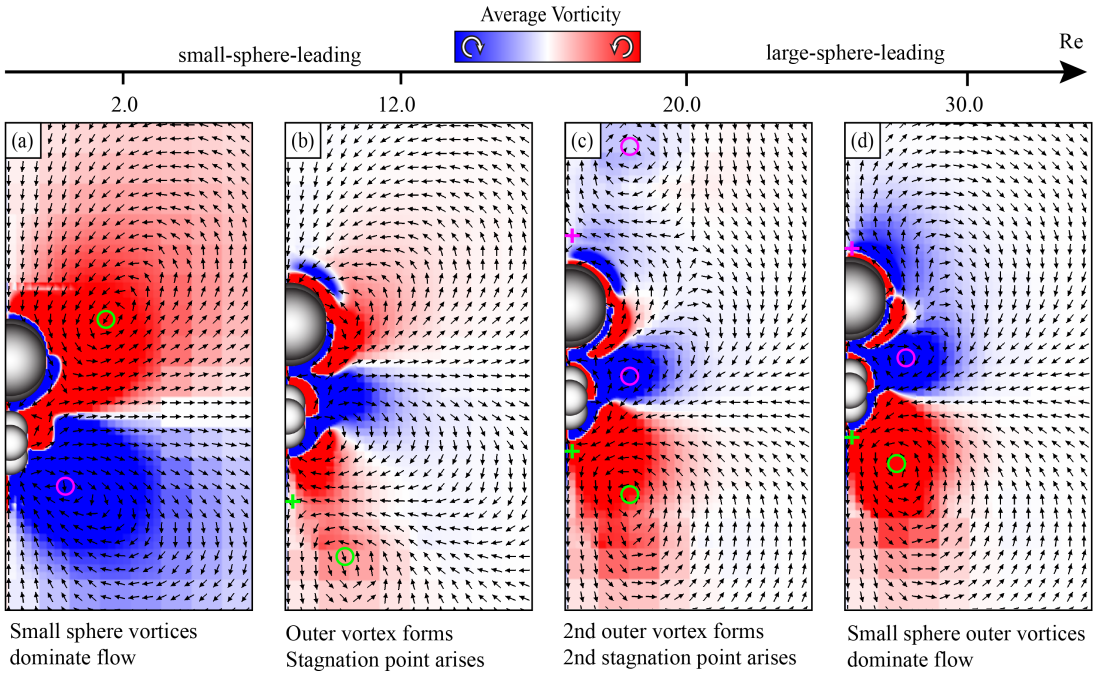

Figure 3.8: The fluid flow around the spherobot continuously evolves across Re. We provide four flows averaged over a cycle, from a spherobot with $\hat{d}_0 = 5.0$ and $\epsilon = 1.2$, across both swimming regimes to highlight its evolution. Vortices of interest are identified with circles (O) and stagnation points are shown with a (+). Their colors are chosen to contrast background vorticity. (a) At Re $= 2.0$, the spherobot swims small-sphere-leading. We observe one pair of vortices from each sphere, and the small sphere's vortices dominate the surrounding flow. (b) At Re $= 12.0$, an outer vortex forms below the small sphere which rotates counter to the inner vortex. The flow direction change below the small sphere is shown to occur at the specified stagnation point. (c) At Re $= 20.0$, another outer vortex forms above the large sphere with an accompanying stagnation point. There is a competition between pushing and pulling the fluid both above and below the spheres, and the spherobot does not swim. (d) The spherobot now swims large-sphere-leading at Re $= 30.0$. The outer vortex above the large sphere disappears, and the flow merges with the outer vortex above the small sphere, pink circle. The outer vortex below the small sphere (green circle) remains and moves closer to the spherobot. The outer vortices generated from the small sphere movement dominate the surrounding fluid flow.

regime where we found that at high Re depending on $\hat{d}_0$ the recovery stroke was more efficient than the power stroke.

We stress the importance in understanding motility and its complexity at intermediate Re. Recent studies have reported other model swimmers which can switch their swim direction based on internal or external stimuli, see *e.g.* passively flapping plate[26] and asymmetric dumbbell shaker[30] respectively. It remains open to see whether other model swimmers at intermediate Re show similar behavior, and what kind of classifications can be made. The theoretical models, such as ours presented here, are important because in their simplicity they hopefully capture physical mechanisms that are obscured by complexity in studies of real organisms. For example, it is possible that steady streaming flows are present in real swimmers at intermediate Re and could explain how they swim or switch between different modes of swimming. However, few studies have investigated flow fields around intermediate-Re swimmers or even other biological systems where there are fluid oscillations at intermediate Re, *e.g.* in the lung[101,102].

Another area of importance is how collective behavior emerges from the nonlinearities that arise when many mesoscale organisms swim together. Are there systems where, say, two organisms individually swim in one preferred direction, but together as a collective swim differently? Finally, from an applications standpoint, it is important to understand the underlying physical mechanisms behind motility at intermediate Re, impacting the design of artificial swimmers, drones, and inertial microfluidics.

3.7 Supplemental Information

3.7.1 Kinematics

We present kinematics after reaching steady state for all of the simulations. In the figures below, the data is separated such that the rows indicate equilibrium distance between spheres $\hat{d}_0$, the columns indicate the amplitude of oscillation ϵ, and the Reynolds number Re of each curve is shown in the accompanying legend (Fig. 3.9). The dashed vertical lines are shown to divide the oscillation cycle into quarters. We measured the fraction of time elapsed during a cycle with the dimensionless time unit, $\tau = ft$. The oscillation was set up so that when $\tau = 0.0, 1.0$ the spheres were at their minimum distance apart $\hat{d}_0 - \epsilon$, when $\tau = 0.5$ they were at their maximum distance apart $\hat{d}_0 + \epsilon$ (black), and when $\tau = 0.25, 0.75$ they were at their equilibrium distance apart (grey). The first half of the cycle was a region of expansion, and the second half was a region of compression.

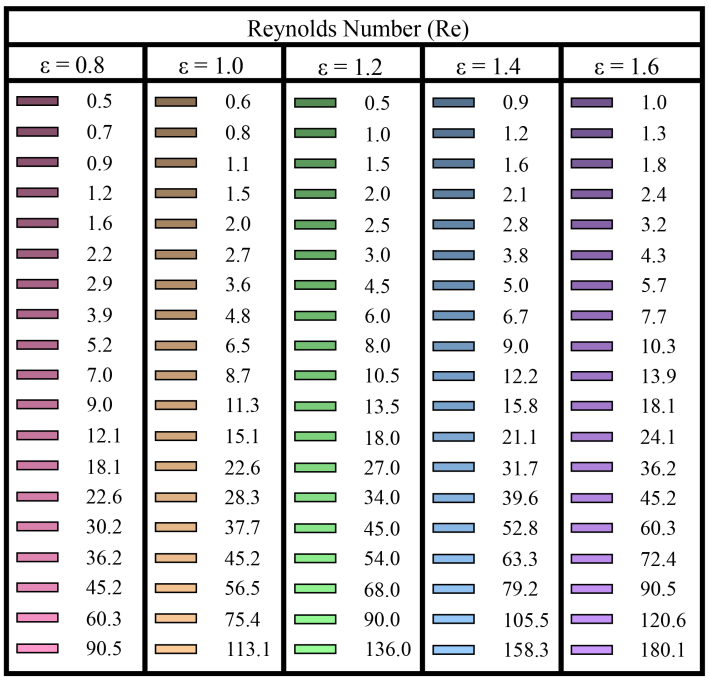

Figure 3.9: The legend used for the following SI figures.

3.7.1.1 Center of Mass: Displacement and Velocity

Fig. 3.10 and Fig. 3.11 show us the displacement and velocity of the spherobot during an oscillation after steady state has been reached, respectively, for all parameters specified in Fig. 3.9.

3.7.1.2 Individual spheres: Displacement and Velocity

Fig. 3.12 and Fig. 3.13 show us the displacements of the spherobot's large sphere and small sphere during an oscillation after steady state has been reached, respectively, for all parameters specified in Fig. 3.9. Fig. 3.14 shows us the net displacement of the individual spheres for the spherobot with equilibrium distance $\hat{d}_0$. Fig. 3.15 and Fig. 3.16 show us the velocities of the spherobot's large sphere and small sphere during an oscillation after steady state has been reached, respectively, for all parameters specified in Fig. 3.9.

3.7.1.3 Expansion and Compression

Fig. 3.17 shows us the net expansion (a) and compression displacement (b) for the spherobot with amplitude $\epsilon = 1.2$ as a function of Re. Fig. 3.18 is the same as Fig. 3.17, but on a log-log scale.

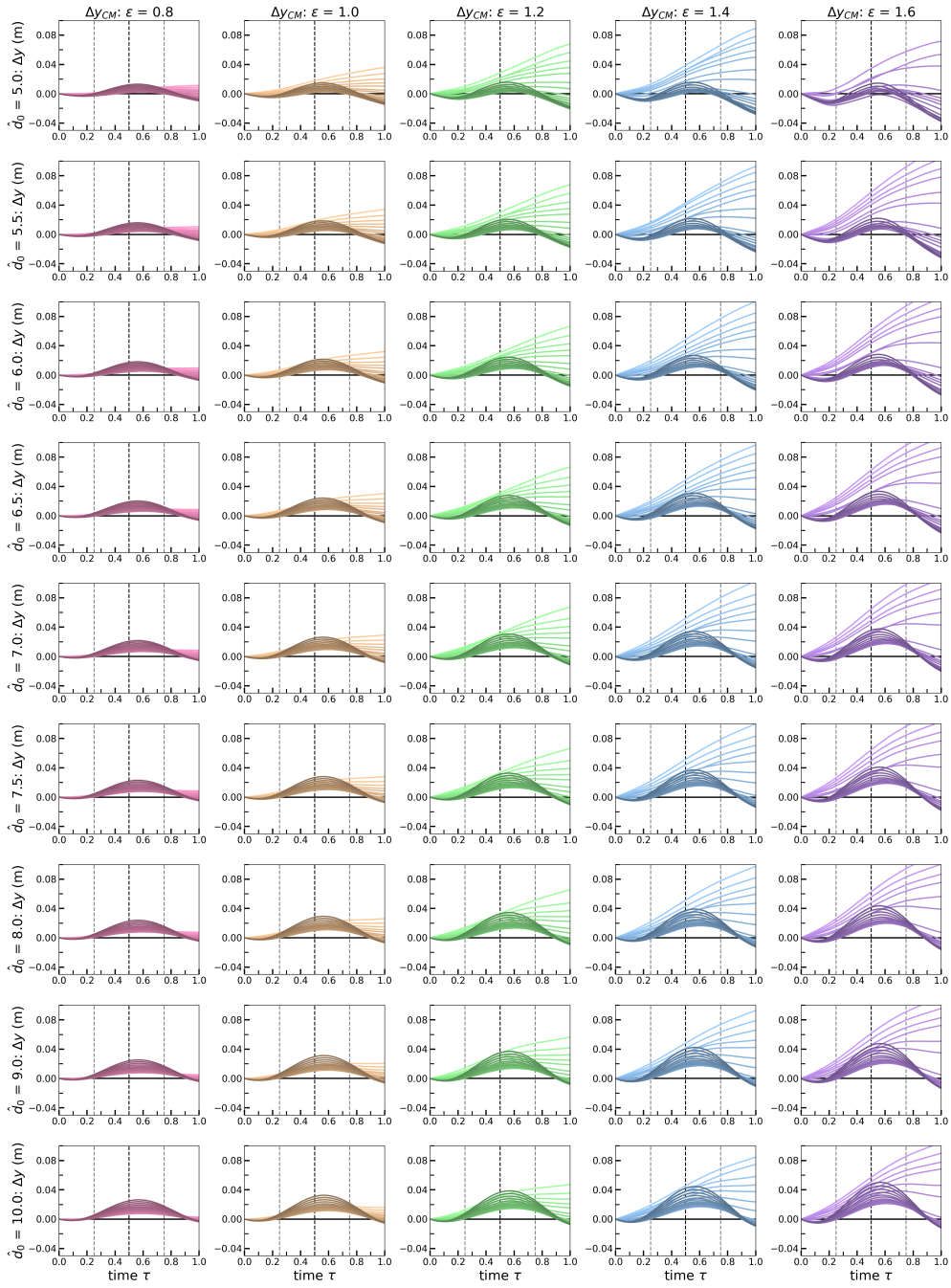

Figure 3.10: Net displacement of the spherobot Δy_{CM} during an oscillation.

3.7.2 Fluid Flow and Efficiency

Fig. 3.19 shows us the efficiency of the spherobot's stroke during expansion η_{exp}, compression η_{com}, and a whole cycle η_{cyc}, as well as its efficiencies during power and recovery, for a spherobot with $\epsilon = 1.2$ and varying $\hat{d}_0$. We immediately notice there is a point in the plots where the recovery stroke becomes

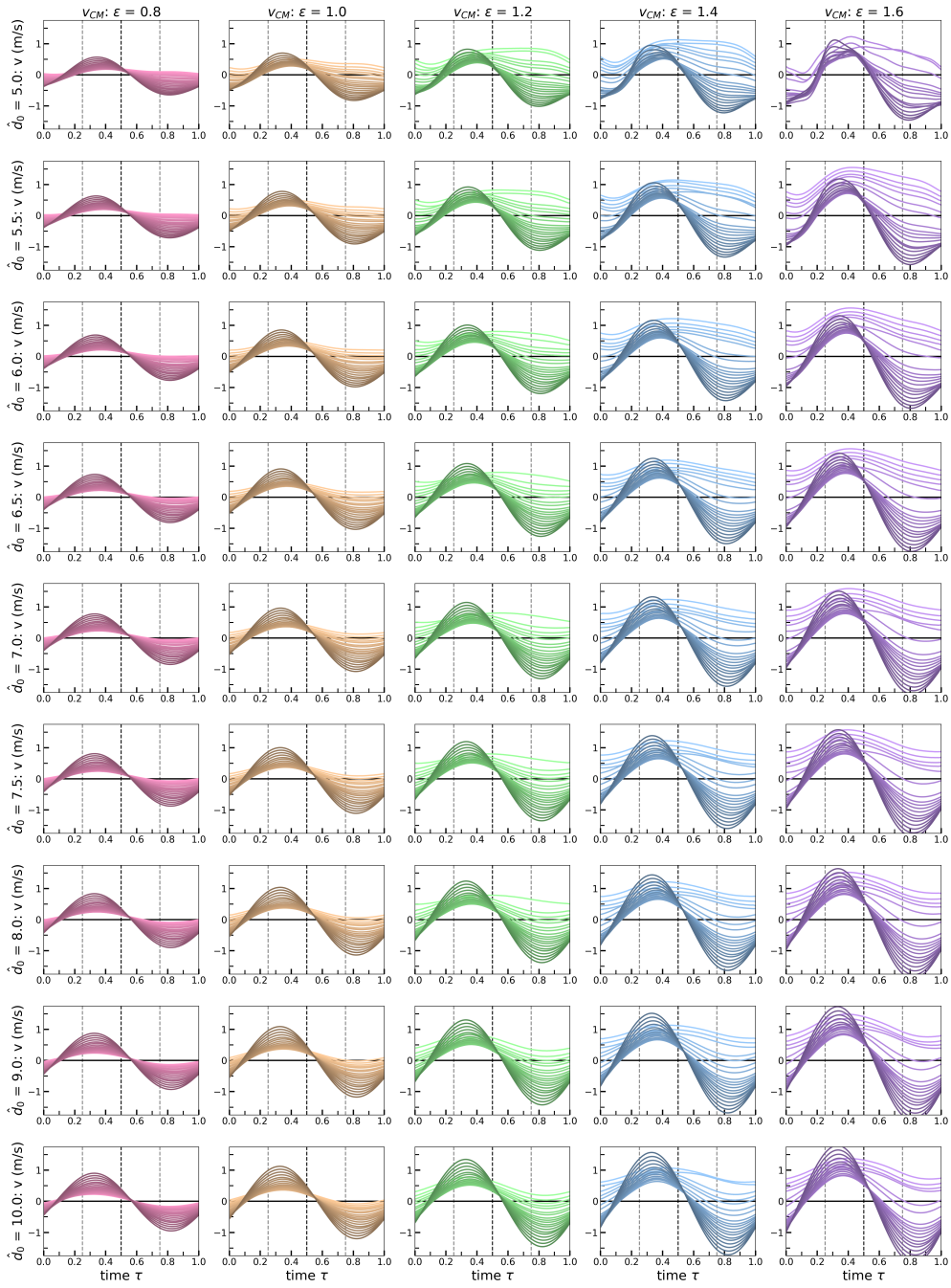

Figure 3.11: Velocity of the spherobot v_{CM} during an oscillation.

more efficient than the power stroke. We see the point where the recovery stroke is the more efficient stroke disappears when $\hat{d}_0$ increases to ($\hat{d}_0 = 9.0, 10.0$). We provide some plausible explanations for why the recovery stroke is more efficient than the power stroke at certain $\hat{d}_0$. The point appears to always occur at a Re higher than Re_c. Therefore, the spherobot is always moving large-sphere-leading there. We start

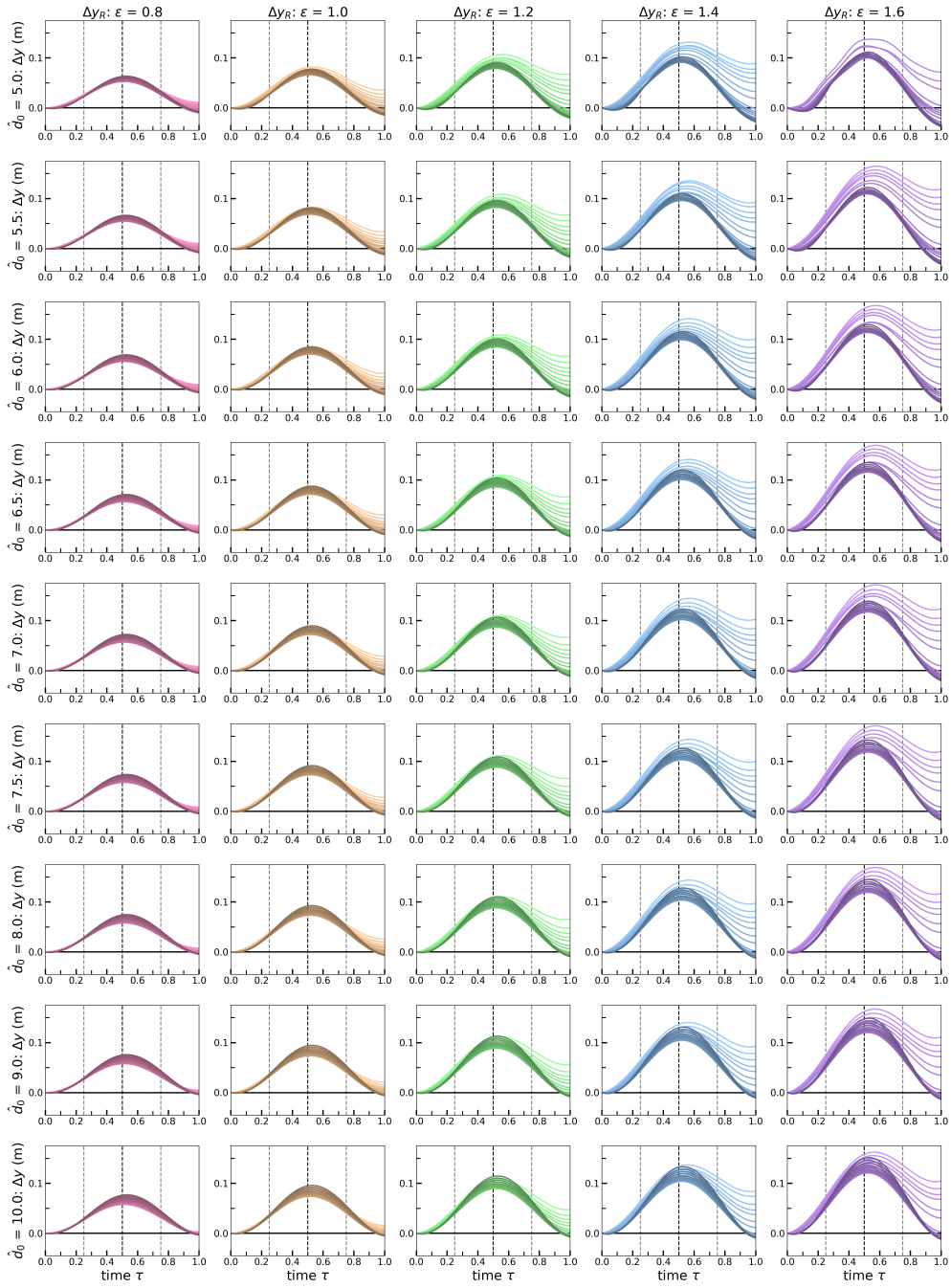

Figure 3.12: Net displacement of large sphere Δy_R during an oscillation.

with an explanation tied to the method used to move the individual spheres a prescribed distance. The spheres are connected to a spring which is prescribed to oscillate with a specified amplitude A at a specified frequency f, $\hat{d}(\tau) = \hat{d}_0 + Asin(2\pi\tau)$. A force is applied to "correct" the position of the spheres such that their distance between $d(\tau)$ is always prescribed correctly, $F(t) = -k(x(\tau) - d(\tau))$. When $x(\tau) > d(\tau)$

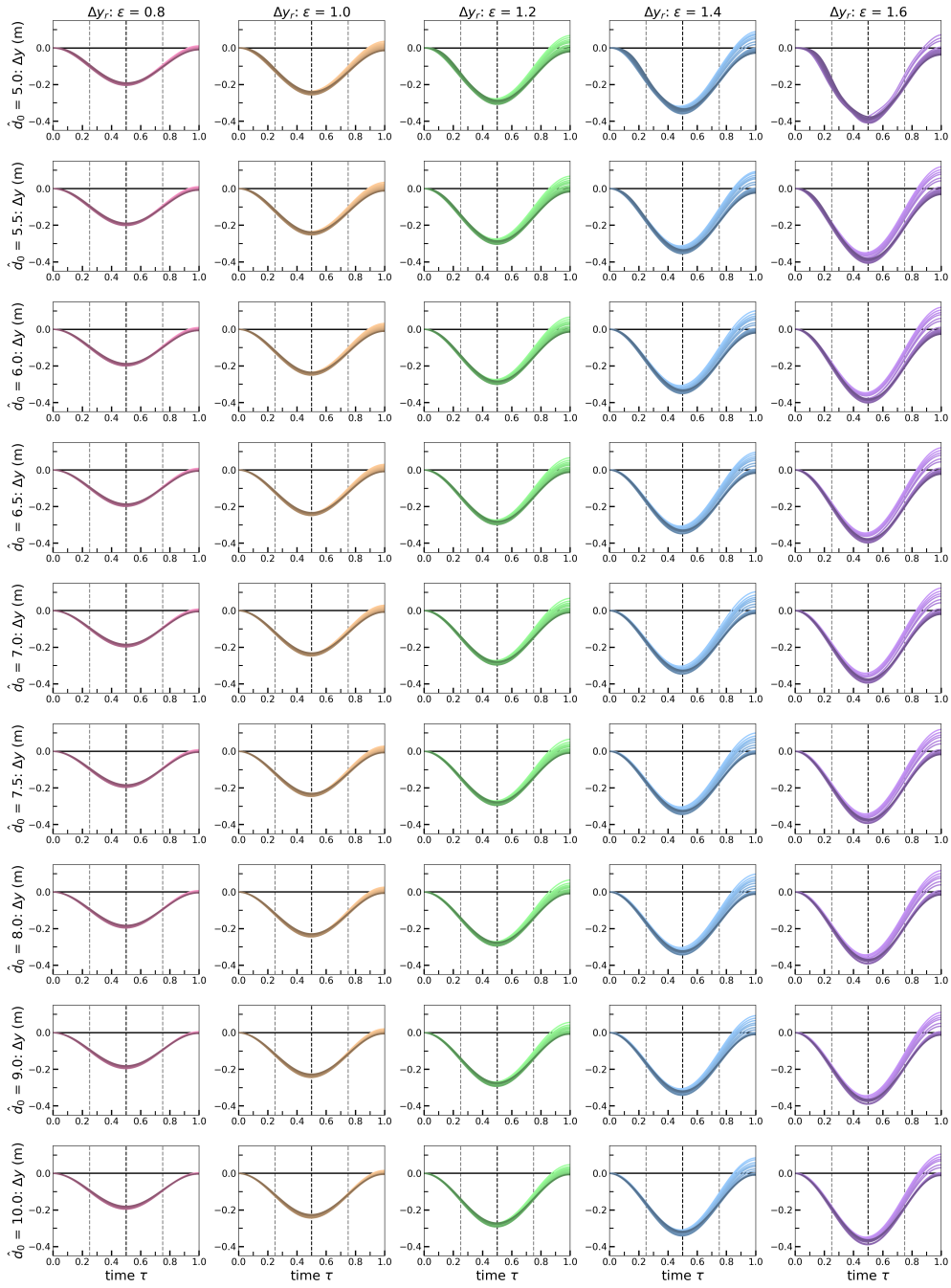

Figure 3.13: Net displacement of small sphere Δy_r during an oscillation.

or vice versa, work is done to the system to keep the prescribed distance. The recovery stroke occurs for a large-sphere-leading spherobot during compression. This means that the small sphere is moving in the mean swimming direction the net and the large sphere opposite to it such that $x(\tau)$ gets smaller. The spherobot is already moving large-sphere-leading so it is possible that the amount of work done to the system decreases to

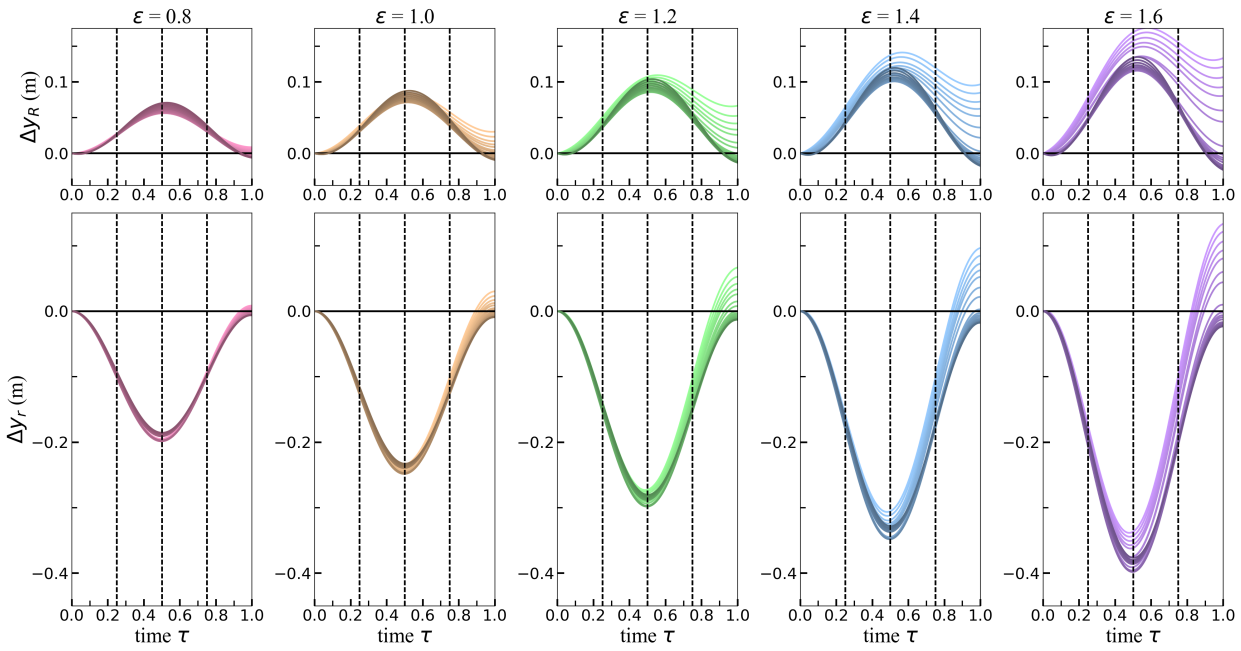

Figure 3.14: Net displacement of individual spheres: top row = sphere of radius R and bottom row = sphere of radius r for the spherobot of equilibrium distance $\hat{d}_0 = 6.5$.

ensure the small sphere is in the "correct" position. One could argue against this by saying the large sphere is moving opposite to net motion so more work must be done to prescribe its motion. We think that is a valid point, but we also think that the since the large sphere moves at a much slower velocity than the small sphere, this additional contribution would be very small compared to the amount the work would reduce because of the small sphere's motion and current positioning. Another possible explanation may come from the evolution in its fluid flow. There may be a coupling of flow between the spheres such that the flow in between the spheres is affecting the efficiency, either by reducing energy input or increasing motion in the mean swimming direction. A third option could be because of the increase in inertia. The spherobot is moving large-sphere-leading. The small sphere also moves large-sphere-leading during the recovery stroke. So as Re increases and v_{CM} increases in magnitude, the swimmer will tend to move large-sphere-leading even more during the recovery stroke.

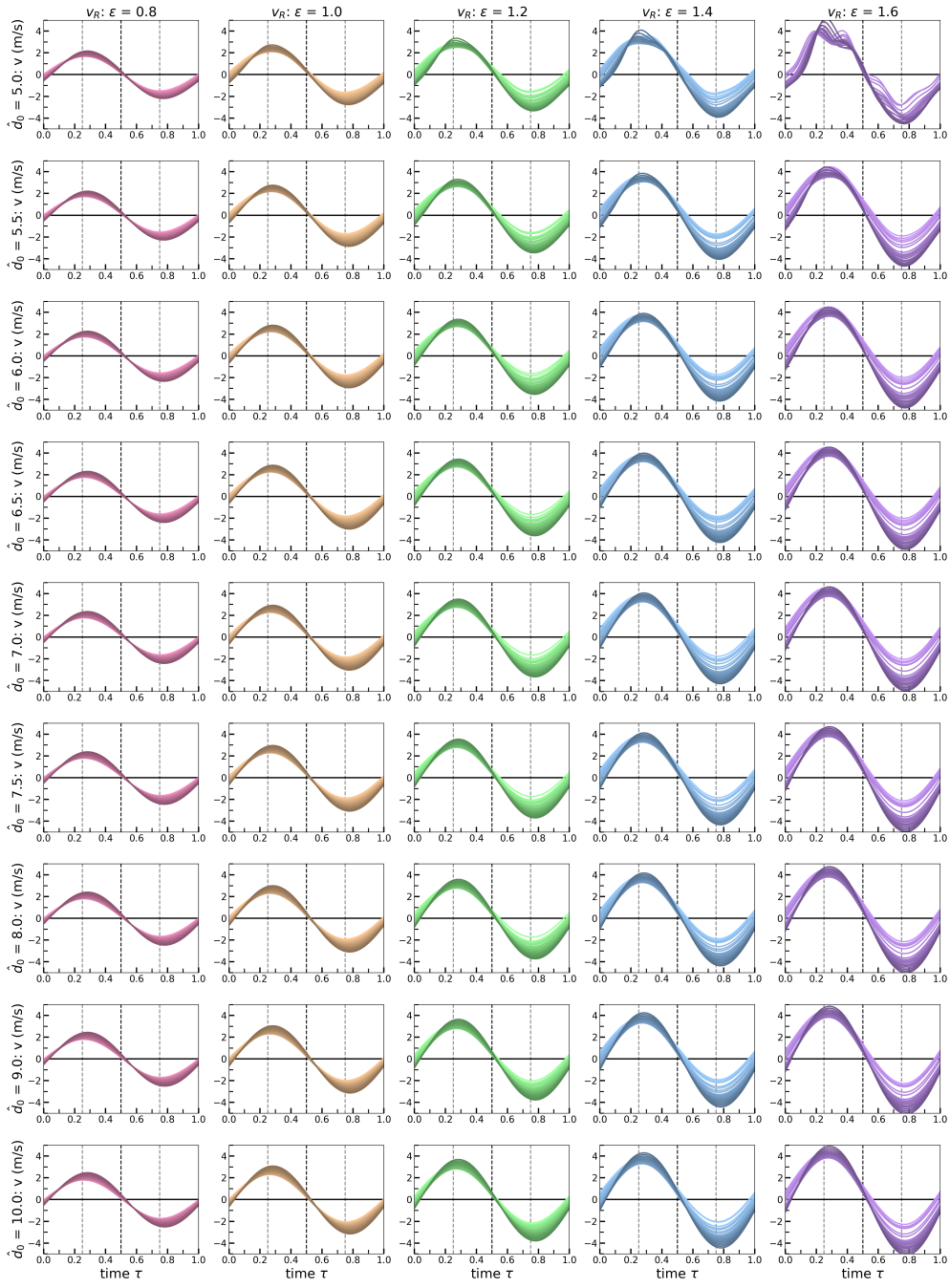

Figure 3.15: Velocity of large sphere v_R during an oscillation.

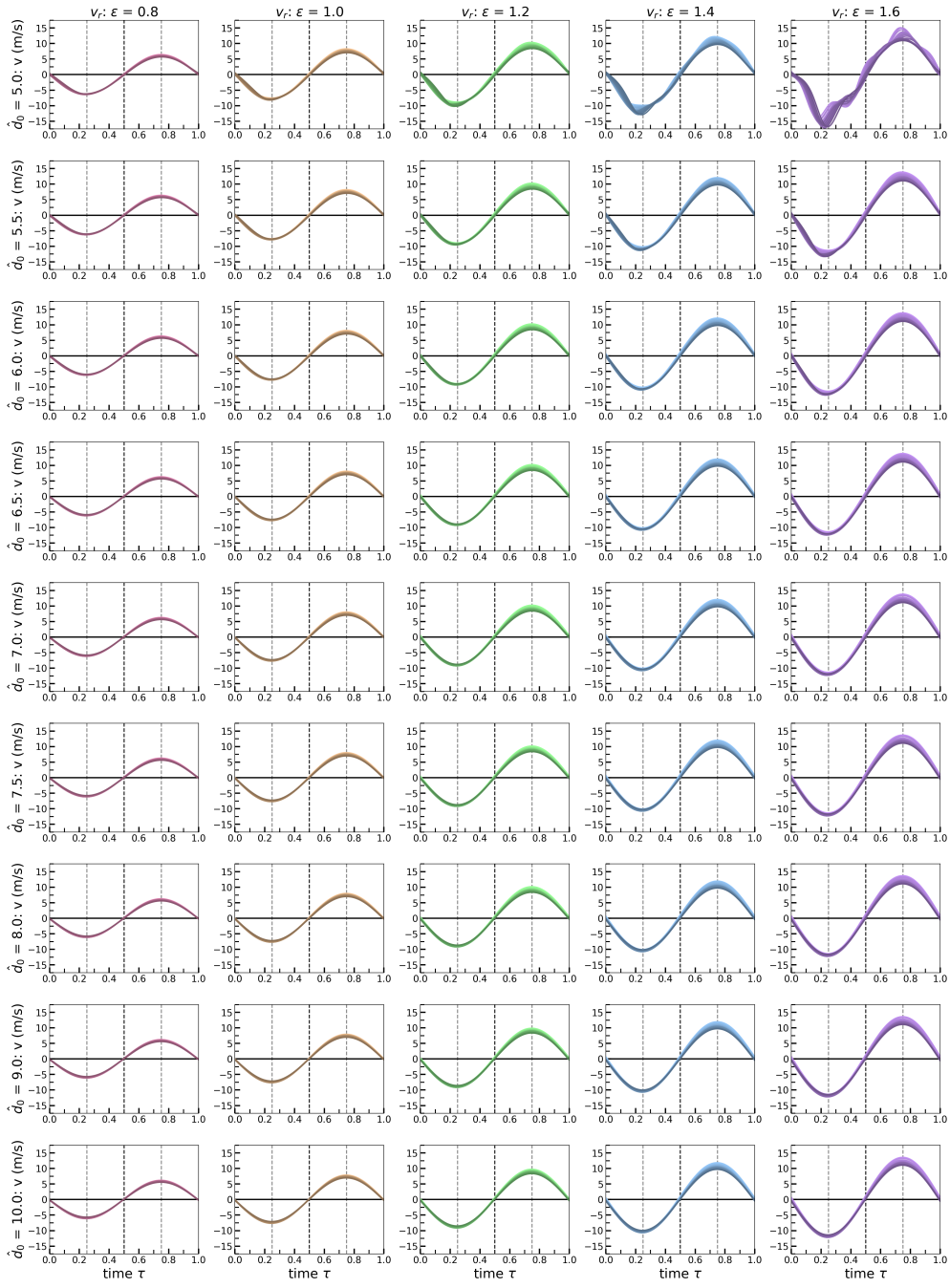

Figure 3.16: Velocity of small sphere v_r during an oscillation.

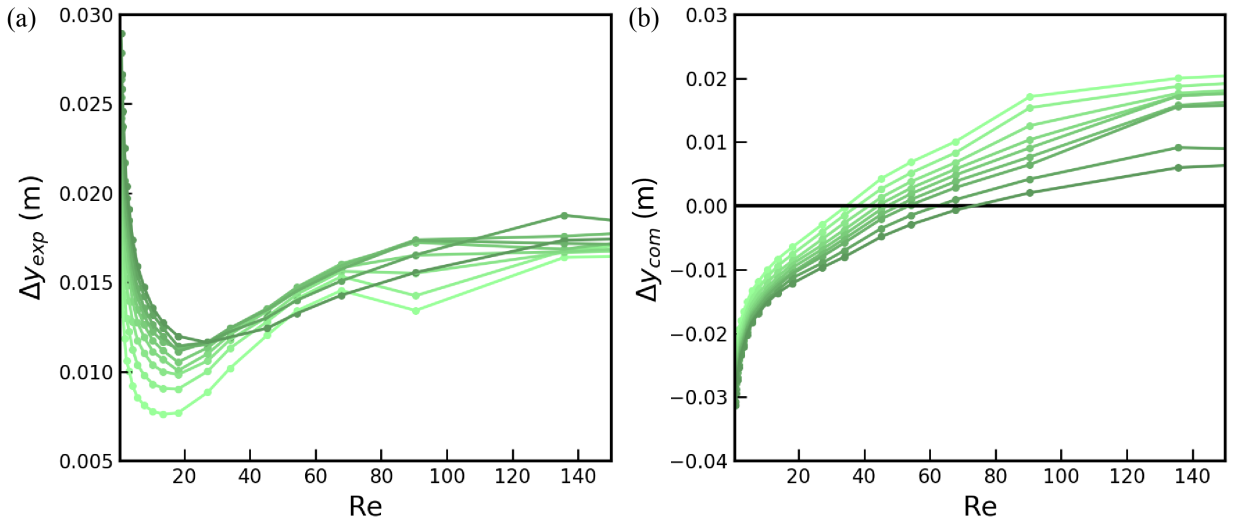

Figure 3.17: Net expansion displacement Δy_{exp} (a) and compression displacement Δy_{com} (b) for the spherobot with constant $\epsilon = 1.2$ versus Re.

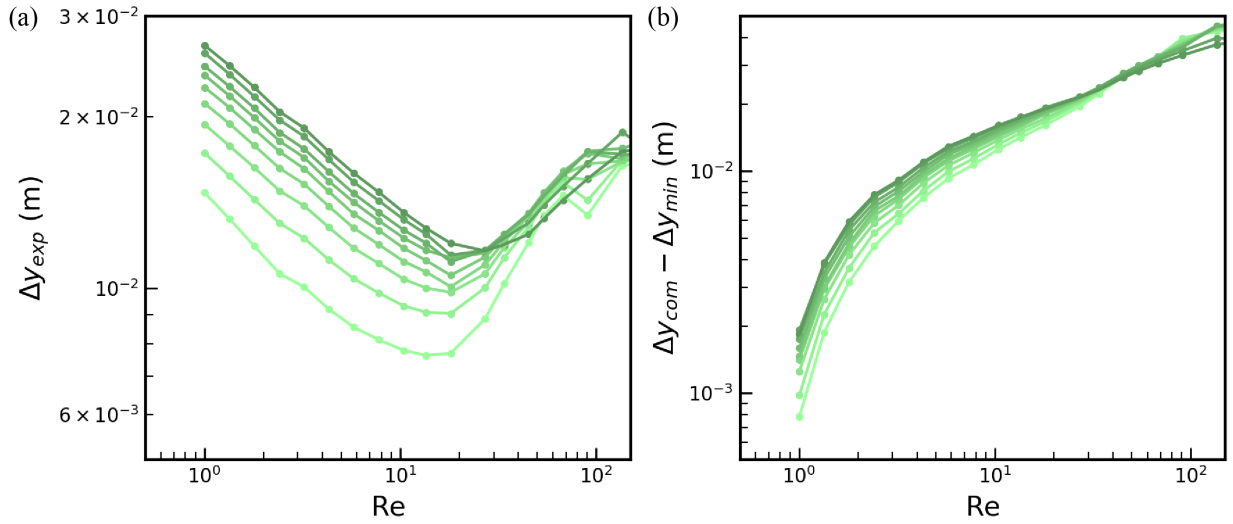

Figure 3.18: Net expansion displacement Δy_{exp} (a) and compression displacement Δy_{com} (b) for the spherobot with constant $\epsilon = 1.2$ versus Re on a log-log scale. The expansion displacements are clearly defined by two power laws with Re where one is of a negative exponent and the other a positive. The compression is renormalized by Δy_{min}. We notice two distinct constant slopes to the curves, indicative of two power laws.

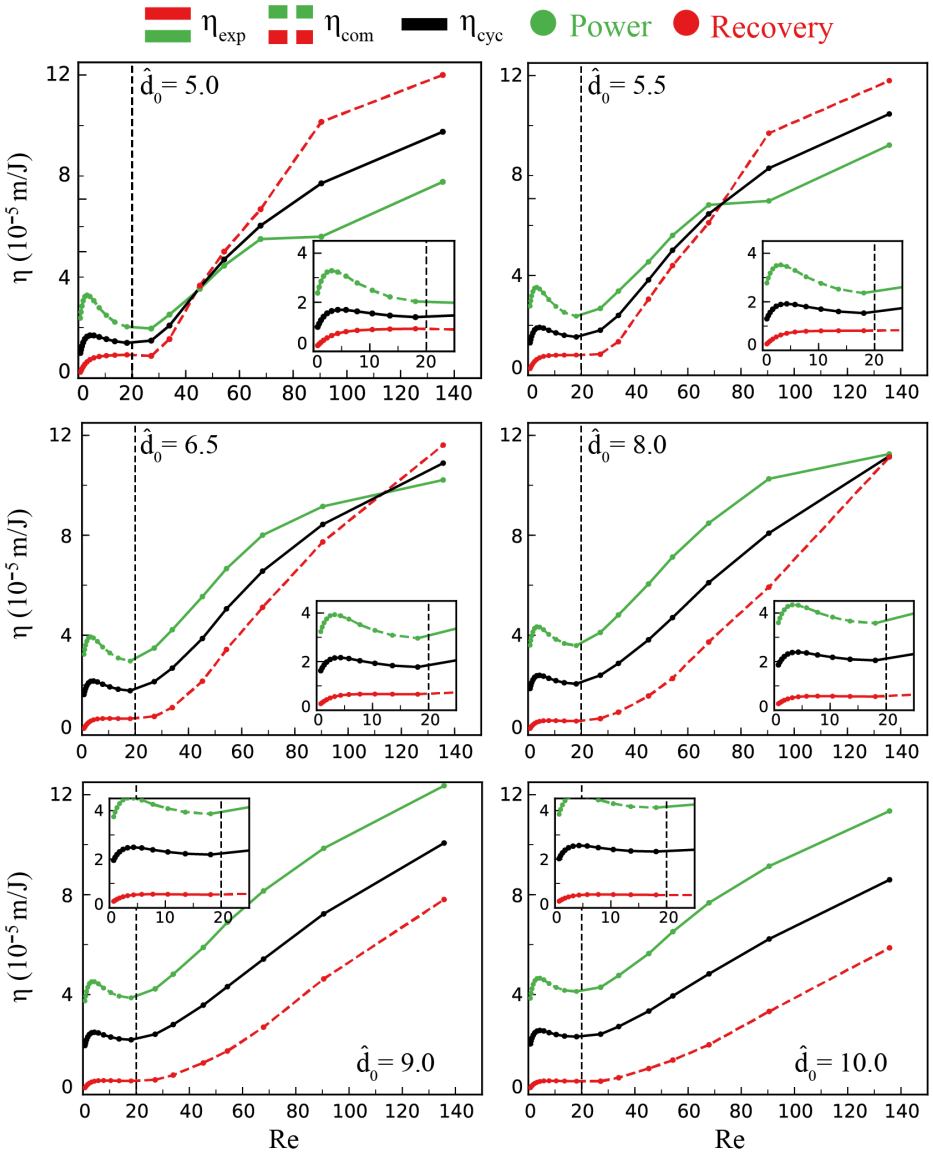

Figure 3.19: Efficiency of a spherobot with amplitude $\epsilon = 1.2$ with varying $\hat{d}_0$ as a function of Re where η_{exp} (solid green and red), η_{com} (dashed green and red), and η_{cyc} (black) are depicted. Also shown are the efficiencies of the power (green) and recovery (red) strokes. The inset shows a close up of the efficiencies in the small-sphere-leading regime. Here, the power stroke occurs during compression, the recovery stroke during expansion, and $\eta_{com} > \eta_{exp}$. Because there is a switch in swimming direction at Re ≈ 20, the power and recovery strokes also switch. Now, $\eta_{exp} > \eta_{com}$. The recovery stroke becomes more efficient than the power stroke at the crossing of the lines. This point is dependent on $\hat{d}_0$. As $\hat{d}_0$ increases, the point where the recovery stroke becomes more efficient than the power stroke occurs at a larger Re. When $\hat{d}_0 = 9.0, 10.0$, the Re where the recovery stroke becomes more efficient disappears in our range.

CHAPTER 4:

Pairwise and collective behavior between model swimmers at intermediate Reynolds numbers [1]

4.1 Overview

We computationally investigate the role of inertial effects in the hydrodynamic interactions between a pair and then a collection of reciprocal, asymmetric dumbbell swimmers at intermediate Reynolds numbers, Re. Dependent on the initial position and rotation, we find that two swimmers either repel and swim away from one another or rearrange to form one of four stable pairs, that are combinations of: in-line and in-tandem, both parallel and anti-parallel. In those stable pairs, swimmers were coordinated, swum together, and generated fluid flows as one. We studied the combined fluid flows and the pairs' velocities as a function of the Reynolds number and found that the in-line pairs act similar to a single swimmer, and are more frequent at lower Re while the in-tandem pairs have more complex dynamics and are more frequent with increasing Re. The collective behavior of 122 swimmers transitions from in-line network-like connections to small, transient in-tandem clusters. We also identify triples, indicative of many-body interactions. Thus, our results help identify when the system can be described by pairwise interactions and when many-body effects become important. Our findings demonstrate the richness and complexity of the collective behavior of intermediate-Re swimmers.

4.2 Introduction

In nature a large number of organisms at various scales use the surrounding medium fluid to perform vital functions, such as to move, feed and mate. Organisms also benefit also from being in pairs or groups as they increase swimming efficiency and speed, feeding rates, reproductive processes, and social interaction [16,24,51,103,104].

[1] This chapter has been submitted as an article in *Physical Review Fluids* and is co-authored by Hong Nguyen and Daphne Klotsa.

Locomotion in the microscopic world is largely limited by the so-called scallop theorem, which states that a swimmer with a reciprocal, time-reversible swim stroke cannot produce a net motion in Stokes flow[34]. Thus, real microscopic organisms break time reversibility with non-reciprocal swim strokes. Moreover, it is rare to find a swimmer isolated from other organisms, which has led to numerous studies (both theoretical and experimental) on the hydrodynamic interactions between Stokesian swimmers[105–110]. For example, sperm cells and B. Subtilis synchronize their flagella, and in doing so are hydrodynamically attracted to one another[105–107]. Many microscopic swimmers can be modeled as squirmers and then be classified as either a "puller" or a "pusher"; the former has a force dipole, which induces a flow field that pulls in parallel to its swimming axis and pushes out in the perpendicular, while the latter does the opposite. Pullers have been shown to attract along their swimming axis and repel in the perpendicular and pushers have been shown to repel along the swimming axis and attract along the perpendicular[49,108,109]. Collision dynamics for a model of chemically active droplets were shown to be sensitive to the relative sizes of the droplets and thus to affect the subsequent dynamics[110,111].

The scallop theorem does not have to hold when there is more than one swimmer (and thus time-reversibility can be broken by the presence of the additional swimmer)[112]. For instance, when two reciprocal, identical dumbbell swimmers oscillate with a phase difference, they could interact to produce a net motion like a single non-reciprocal swimmer. The dumbbell is a common model for a simple reciprocal swimmer composed of two spheres that oscillate with respect to each other. Studies on the hydrodynamic interactions between a pair of dumbbell swimmers in Stokes flow have shown how swimmers align and swim together, depending on their initial configuration[83,84,113]. The pair interactions between two asymmetric dumbbells have been analytically solved for the one-dimensional case of reflection invariant pairs (collective swimming at a constant velocity) and translation invariant pairs (attractive or repulsive dependent on the leading swimmer orientation)[84]. A more extensive study developed stroke-averaged equations of motion for the effective hydrodynamic interactions between asymmetric dumbbell pairs in Stokes flow[113].

Previous studies of interacting swimmers have been mostly limited to the Stokes regime, where inertial forces are negligible. However, as the Reynolds number increases, the inertial contribution to the system's dynamics becomes important. Indeed, inertial effects on a model mesoscale swimmer can induce a switch in the swimming direction[31,33] and impact predator/prey dynamics[114]. Recently, there has been a growing interest in understanding how inertial effects impact interactions between squirmers[115,116]. Squirmers aligned initially in parallel will attract if they are pushers and repel if they are pullers[115], and when on a

collision course, inertial effects change the contact time and dynamics for pushers and prompt hydrodynamic attraction for pullers[116]. Less is known about other inertial swimmers, models beyond squirmers or real ones. Additionally, the role of inertia on the collective behavior of swimmers beyond a pair is largely unexplored, with the exception of Chatterjee *et al.* who identified stable, unstable and turbulent states for active suspensions of weakly inertial pushers[117].

In this paper, we computationally studied the pairwise and many-body hydrodynamic interactions for model reciprocal, asymmetric dumbbell swimmers over a range of intermediate Reynolds numbers. Varying the initial positions and orientations for two swimmers, we found regions where they repel and swim away from one another and regions where they interact to form stable pair configurations. From thousands of initial conditions, only four stable pairs were identified, which can be grouped as: in-line and in-tandem, parallel and anti-parallel. Parallel in-tandem pairs form a V-shape and antiparallel form a dynamic orbit. In stable pairs, swimmers were coordinated, swum together, and generated fluid flows as one. We studied the pairs' combined fluid flows and velocities as a function of the Reynolds number. We found that in-line pairs act similar to a single swimmer and are more frequent at low Re, while the in-tandem pairs have more complex dynamics and become more frequent as Re increases. In-tandem pairs show a transition from small-sphere-leading to large-sphere-leading coordinated swimming at different Reynolds numbers to each other and different compared to the single swimmer[31]. Finally, we simulated 122 swimmers and found a transition from in-line network-like connections to in-tandem clusters as the Reynolds number increases. Pairwise interactions were used to partly explain the collective behavior; however, limitations were discovered as many-body interactions such as triples were also identified.

The structure of the paper is as follows. In section II, we describe the model, computational method, and simulation details. In section III we present our results: the stable pairs formed by two asymmetric dumbbells, the comparison between swimming as an individual and as a stable pair, and the stroke-averaged fluid flows. We end with the evolution of the collective behavior and conclusions in section IV.

4.3 Model and Methods

We consider a two-dimensional system of identical, asymmetric dumbbell swimmers. Each dumbbell is composed of two unequal sized spheres of radii R and r with an aspect ratio of $\alpha = r/R = 0.5$, see Fig 4.1a. The dumbbell's swimming axis is along the line connecting the centers of the two spheres. The following

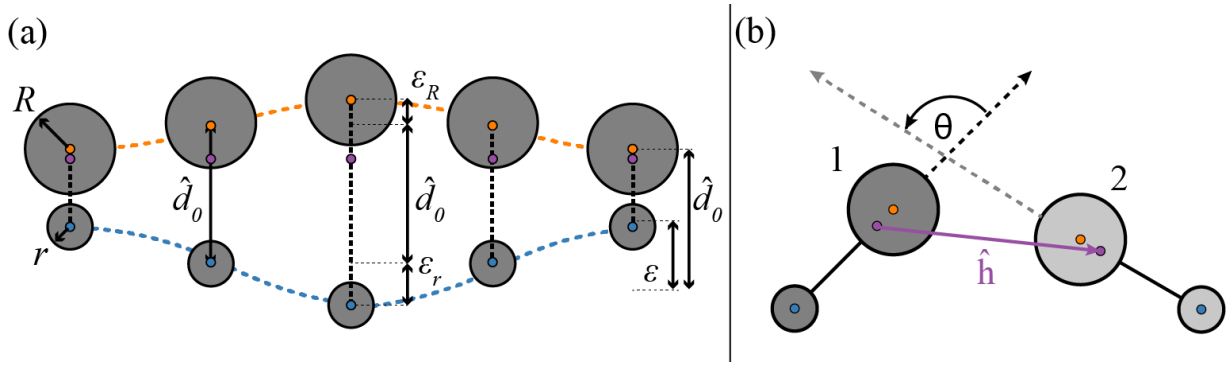

Figure 4.1: (a) Swim stroke of the asymmetric dumbbell with $\alpha = 0.5$. The dumbbell's large sphere (orange) oscillates in antiphase with the small sphere (blue) and the distance between them is prescribed to be of a simple harmonic oscillator with equilibrium length $\hat{d}_0$ and amplitude ε. (b) A pair of asymmetric dumbbells separated by a distance $\hat{H}$ and oriented with angle θ. θ is formed by the counter-clockwise rotation from the swimming axis of swimmer 1 to that of swimmer 2.

conditions ensure that the dumbbell swimmer is force- and torque-free. The spheres are neutrally buoyant with respect to the surrounding fluid. The distance between the two spheres $\hat{d}(t)$ is prescribed to be of a simple harmonic oscillator such that $\hat{d}(t) = \hat{d}_0 + \varepsilon\sin(2\pi\tau)$, where $\hat{d}_0 = d_0/R = 2.5$ is the equilibrium distance between sphere centers, $\varepsilon = 0.8$ is the amplitude of oscillation, and $\tau = ft$ is the dimensionless time parameterized by f the frequency of oscillation. The amplitudes of each sphere are determined by the conservation of momentum $\varepsilon_r = \varepsilon R^2/(r^2 + R^2)$ and $\varepsilon_R = \varepsilon r^2/(r^2 + R^2)$, where subscripts R and r represent quantities specific to the large sphere and small sphere, respectively. Because $R = 2r$ we find that $\varepsilon_r = 4\varepsilon_R$.

The asymmetric dumbbell swimmers were immersed in a viscous, incompressible Newtonian fluid that occupied a finite cell with periodic boundary conditions. The fully-coupled fluid-structure interaction system was resolved using the Immersed Boundary (IB) method[66,118]. The IB scheme was implemented in the open-source IBAMR software, which is an immersed boundary numerical method with adaptive mesh refinement[64,66]. The IB method for fluid-structure interaction uses an Eulerian formulation of the momentum equation and incompressibility constraint for the coupled fluid-solid system along with a Lagrangian description of the motion of the immersed structures. Let $\mathbf{x} \in \Omega$ be fixed Eulerian physical coordinates, and let $\mathbf{s} \in U$ be fixed Lagrangian curvilinear coordinates attached to the structure, where Ω and U are the physical regions occupied by the fluid-structure system and structures respectively. In our notation, $\mathbf{X}(\mathbf{s}, t) \subset \Omega$ is the physical position of material point $\mathbf{s}$ at time t. The momentum equation and

incompressibility constraint are given by

$$\rho\frac{D\mathbf{u}}{Dt}(\mathbf{x},t) = -\nabla p(\mathbf{x},t) + \mu\nabla^2\mathbf{u}(\mathbf{x},t) + \mathbf{f}(\mathbf{x},t), \tag{4.1}$$

$$\nabla\cdot\mathbf{u}(\mathbf{x},t) = 0, \tag{4.2}$$

in which $\mathbf{u}(\mathbf{x},t)$ is the Eulerian velocity field, $p(\mathbf{x},t)$ is the pressure field that imposes the incompressibility constraint, $\mathbf{f}(\mathbf{x},t)$ is a body force that arises from the presence of the immersed structure, ρ is the mass density, and μ is the viscosity. Eulerian and Lagrangian variables are coupled via integral transforms with Dirac delta function kernels:

$$\mathbf{f}(\mathbf{x},t) = \int_U \mathbf{F}(\mathbf{s},t)\,\delta(\mathbf{x}-\mathbf{X}(\mathbf{s},t))\,\mathrm{d}\mathbf{s}, \tag{4.3}$$

$$\mathbf{U}(\mathbf{s},t) = \int_\Omega \mathbf{u}(\mathbf{x},t)\,\delta(\mathbf{x}-\mathbf{X}(\mathbf{s},t))\,\mathrm{d}\mathbf{x}\,. \tag{4.4}$$

Eq. (4.3) converts the Lagrangian force density $\mathbf{F}(\mathbf{s},t)$ to an equivalent Eulerian force density $\mathbf{f}(\mathbf{x},t)$, and Eq. (4.4) evaluates the local material velocity at each structural position.

In our computer model, each sphere of the dumbbell was discretized using a collection of Lagrangian marker points that were generated using an in-house Python code, and the singular delta function kernels were replaced by a four-point regularized kernel function[66]. To maintain each sphere's rigidity, each marker point was connected with their nearest neighbors via intra-sphere stiff springs. The spheres were also connected by a set of inter-sphere springs which controlled their swim stroke oscillation and prevented individual sphere rotation. The force $\mathbf{F}(\mathbf{s},t)$ applied on marker point $\mathbf{s}$ at time t was solely due to the linear expansion/compression of the springs. The spring force for marker points $\mathbf{s}_1$ and $\mathbf{s}_2$ connected by the spring ℓ was given by:

$$\mathbf{F}^\ell(\mathbf{s}_1,\mathbf{s}_2,t) = -K_s(|\mathbf{X}(\mathbf{s}_1,t)-\mathbf{X}(\mathbf{s}_2,t)|-R_\ell) \tag{4.5}$$

where K_s was the spring stiffness coefficient and R_ℓ was the resting length of spring ℓ. We note that $\mathbf{F}^\ell(\mathbf{s}_1,\mathbf{s}_2,t) = -\mathbf{F}^\ell(\mathbf{s}_2,\mathbf{s}_1,t)$. The resting length of the inter-sphere springs updates to the prescribed distance between $\mathbf{s}_1$ and $\mathbf{s}_2$ at every time step, while the resting length for the intra-sphere springs is kept fixed. For the inter-sphere springs, $K_s = 1.0\times10^4$N/m, and for the intra-sphere springs, $K_s = 5.0\times10^4$N/m.

These stiffness coefficients have been chosen small enough for numerical stability and also large enough to ensure that the individual sphere's deformation is negligible, and that the distance between spheres is approximately kept at the prescribed distance at all time. More details on the spatial discretization and the time stepping algorithm for the IB method can be found in references [66,118].

In IBAMR, an adaptive fluid grid is implemented to improve the efficiency of the simulation. There were four refinement levels (N=16, 64, 256, and 1024) and the dumbbell meshes were evaluated at the highest grid refinement of N=1024 and grid spacing of $d\hat{\mathrm{X}} = d\mathrm{X}/R = L/NR = 0.049$, where L is the size of the simulation box. The spacing between marker points is set by the standard IB method to be $d\hat{\mathrm{S}} = 0.5d\hat{\mathrm{X}}$ to avoid fluid leak into the spheres. The simulation box L was large enough to prevent finite size effects, $L = 12.5(d_0 + R + r) = 50R$. Close contact between immersed structures are automatically handled by IBAMR with an enhanced version of the kernel function[119]. Therefore, no special treatment is needed for the collision between dumbbells within the IB scheme currently employed.

The pair system was composed of two identical dumbbells parameterized by the separation distance at time t, $\hat{h}(t) = h(t)/R$ between the dumbbells' centers of mass, and the counter-clockwise angle formed between their swimming axes θ, see Fig. 4.1b. The initial conditions are stated as $\hat{h}(t=0) = \hat{H} = \langle \hat{H}_x, \hat{H}_y \rangle$ We used the frequency Reynolds number of the small sphere $\mathrm{Re} = \alpha \varepsilon_r M^2$, with viscosity $M^2 = R^2/\delta^2$ and boundary layer thickness $\delta = \sqrt{\nu/\omega}$. The reason for the choice of Re is that it has been found to control the transition of swimming dynamics in the single dumbbell's system[31,33]. Note that there are many Reynolds numbers (dimensionless ratios) that can be defined in this system because of the many length scales – for a discussion see Dombrowski *et al.*[33]. We monitored the swimming pair until the swimmers either diverged ($\hat{h} > 10$) or reached a steady state (separation distance $\hat{h}$ and angle θ changed by less than one percent over consecutive swim strokes). We monitored the pair systems until steady state had been reached, and the simulation duration varied from at least twenty to over four hundred oscillations.

When extending to multiple swimmers, the IB method becomes computationally expensive due to the large number of marker points, stiff springs, and increasingly smaller time steps. Therefore, in the supplemental information (SI), we describe an alternative computational scheme with which we simulated a system of 122 swimmers.

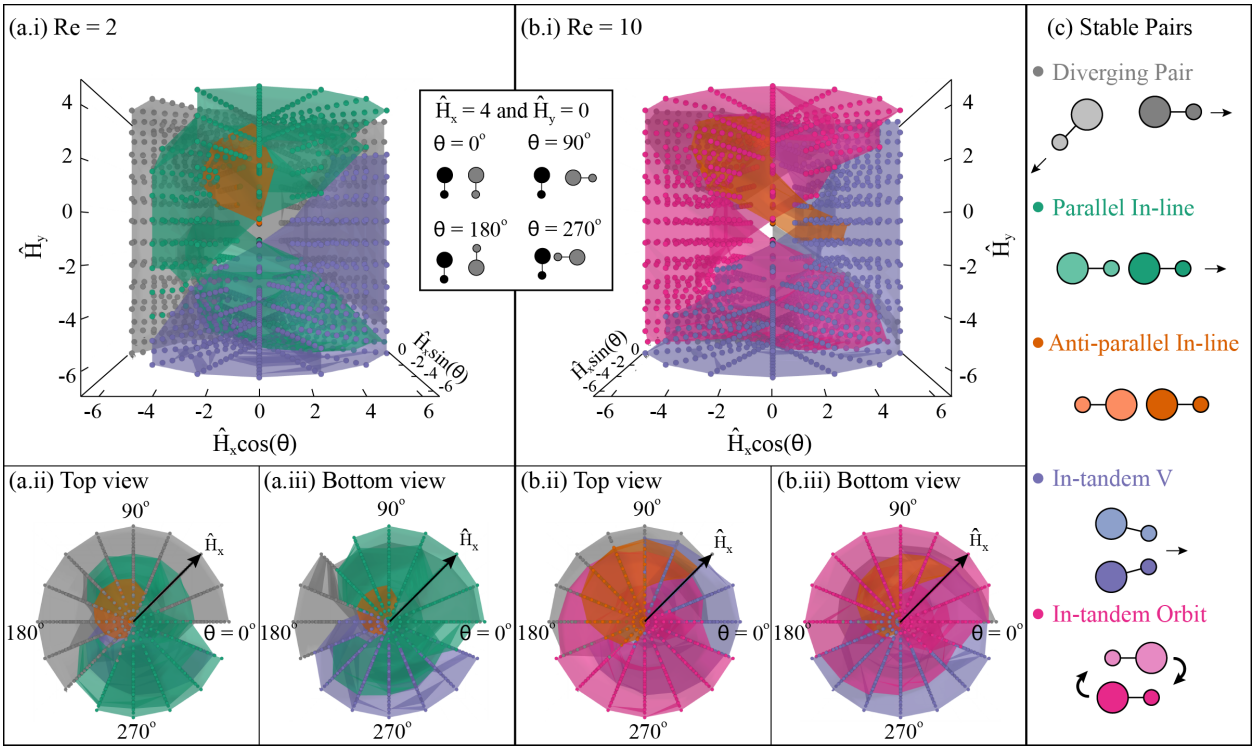

Figure 4.2: Identified regions of diverging or stable pairs after steady state had been reached for (a) Re $= 2.0$ and (b) Re $= 10.0$ based on initial configurations $\hat{H}_x$,$\hat{H}_y$, and θ. Initial configurations are determined based on the position and orientation of the grey swimmer with respect to the black swimmer. (ii) Regions of pair behavior when the grey swimmer is above the black swimmer and (iii) when the grey swimmer is below the black swimmer. (c) Schematic of pair behaviors: diverging (grey), parallel in-line (green), anti-parallel in-line (orange), in-tandem V (blue), and in-tandem orbit (pink).

4.4 Results

4.4.1 Pair stable states

We first investigated how two swimmers interacted starting from different initial configurations, for three representative intermediate Reynolds numbers, Re $= 2$, 7, and 10. Specifically, we performed a large sweep (more than 5,600 simulations) over position and rotation space, varying the initial separation distance, $0.25 \leq \hat{H}_x \leq 6.25$ and $-6.5 \leq \hat{H}_y \leq 4.5$, over angles θ in the range $0 - 360$ in increments of $360/16$.

We found that for all initial configurations, and Reynolds numbers studied, the swimmers either swam away from one another or converged to one of only four stable pair states, that are the combinations of in-line and in-tandem, parallel and antiparallel arrangements, as shown schematically in Fig. 4.2(c). Once the swimmers arranged into their preferred stable pair, they then swum together in a coordinated motion as one. We plotted three-dimensional "phase diagrams" showing the resulting stable pairs as a function of the initial relative positions and angles between the swimmers. It is interesting to compare these diagrams for Re $= 2$ and Re $= 10$, see Fig. 4.2 (a),(b). For Re $= 2$, we see a large portion of the initial-conditions phase space assembles parallel in-line pairs or leads to diverging pairs, and there are also smaller regions of antiparallel in-line and in-tandem V pairs, see Fig. 4.2 (a). On the other hand, for Re $= 10$, we found that parallel in-line pairs have become in-tandem orbit pairs. Moreover, there is a larger region of in-tandem V pairs and almost no diverging pairs, see Fig. 4.2 (b). The Re $= 7$ phase diagram shows how the stable configurations gradually change as a function of Reynolds numbers between the Re $= 2$ and Re $= 10$, see SI (section III). We note that there was a fourth state discovered which resembled an L shape. But this state was found to be meta-stable because all of the L shaped systems eventually transitioned into parallel in-line pairs. Next, we investigate each pair in more detail.

4.4.2 Pair velocity as a function of Re

We monitored the pairs' steady-state velocity, as well as their separation distance H across Re to understand how different pair dynamics compares to those of a single swimmer and thus provide insight on possible benefits behind forming each stable pair. We calculated the average velocity of the swimmers by averaging the velocity per oscillation over the total number of oscillations in steady state. Note that, for

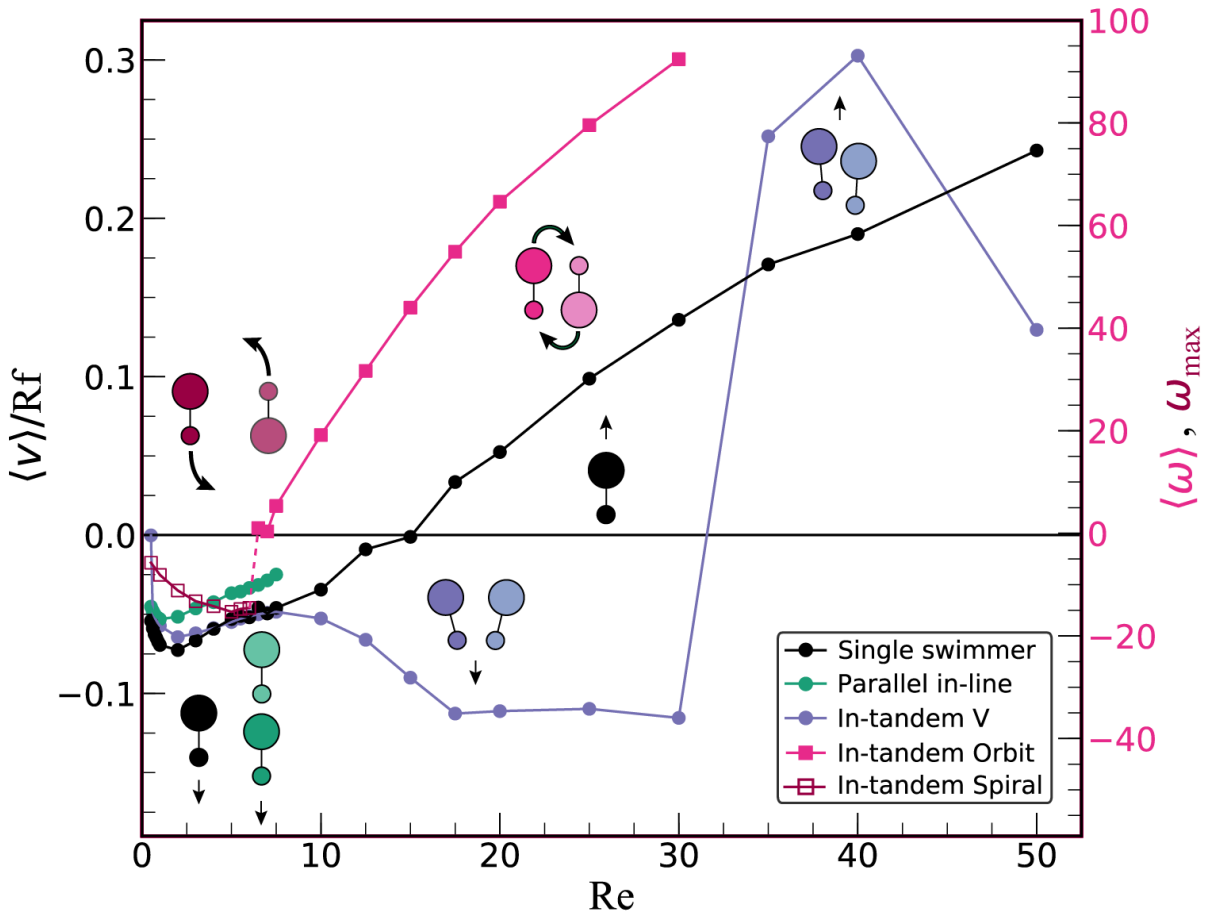

Figure 4.3: The swimming velocity of an in-tandem V pair (blue), a parallel in-line pair (green), and a single swimmer (black), as well as the angular velocity of the in-tandem orbit pair (pink) versus the Reynolds number. The single swimmer switches its swimming direction from small-sphere-leading to large-sphere-leading at Re ≈ 15, the in-tandem V pair at Re ≈ 35 and the in-tandem orbit at Re ≈ 6.5

the in-tandem orbit pair, we calculated the angular velocity. We excluded antiparallel in-line pairs from the comparison because they are stationary and have neither net translational nor angular velocity. A comparison of the velocities for the swimming and orbiting pairs and of a single swimmer are shown in Fig. 4.3. The pairs' separation distance as a function of Re is shown in the SI.

The parallel in-line pair swims small-sphere-leading, and the curve looks similar to the single swimmer in the Reynolds number range $0.5 \leq$ Re ≤ 7.5, but with a slightly lower speed than the single swimmer case. It seems reasonable to ascertain that the speed difference is due to the presence of the second swimmer in tow behind the leading swimmer. The swimmer in tow may be increasing the resistance, which could be attributed to a net attraction/pulling motion between the swimmers, an increase in fluid flow motion behind the leading swimmer, or the mass added to the system by the second swimmer. For $Re > 7.5$, the swimmers collide and push away from one another, so there is no stable pair for which to calculate an average translational velocity.

The in-tandem V pair swims small-sphere-leading for a larger Reynolds number range $0.5 <$ Re ≤ 30 compared to the single swimmer. While from $Re = 0.5$ to $Re = 7.5$ the V-pair and the single swimmer's velocity curves are almost on top of each other; for Re¿7.5, the curves diverge. The V-pair actually speeds up till it stops moving in a straight line and picks up a rotational velocity and moves on an arc (which results in the plateau of the translational velocity around $Re \approx 17$, see Fig. 4.3). Then at $Re \approx 35$ we see a sharp transition from small-sphere-leading to large-sphere-leading. In other words, the Reynolds number at which the switch in swim direction occurs is much larger for the pair (Re $= 35$) than for the single swimmer (Re $= 15$), which we would not have predicted. Looking closely, the switch in swimming direction for the V-pair happens when the swim stroke actually changes a little bit, to include a stagger motion, see movie in the Supplemental Material. When Re > 50 swimmers eventually physically collide and no longer form a stable pair.

The in-tandem orbit pair is stable only in the large-sphere-leading regime, which occurs around $Re \approx 6.5$ (a lower Re than for the single swimmer which is at $Re \approx 15$). For $Re < 6.5$ the swimmers swim small-sphere-leading and move away from one another in a small-sphere-leading spiral. For Re ≥ 6.5 the angular velocity of the stable orbit pair increases monotonically with increasing Re.

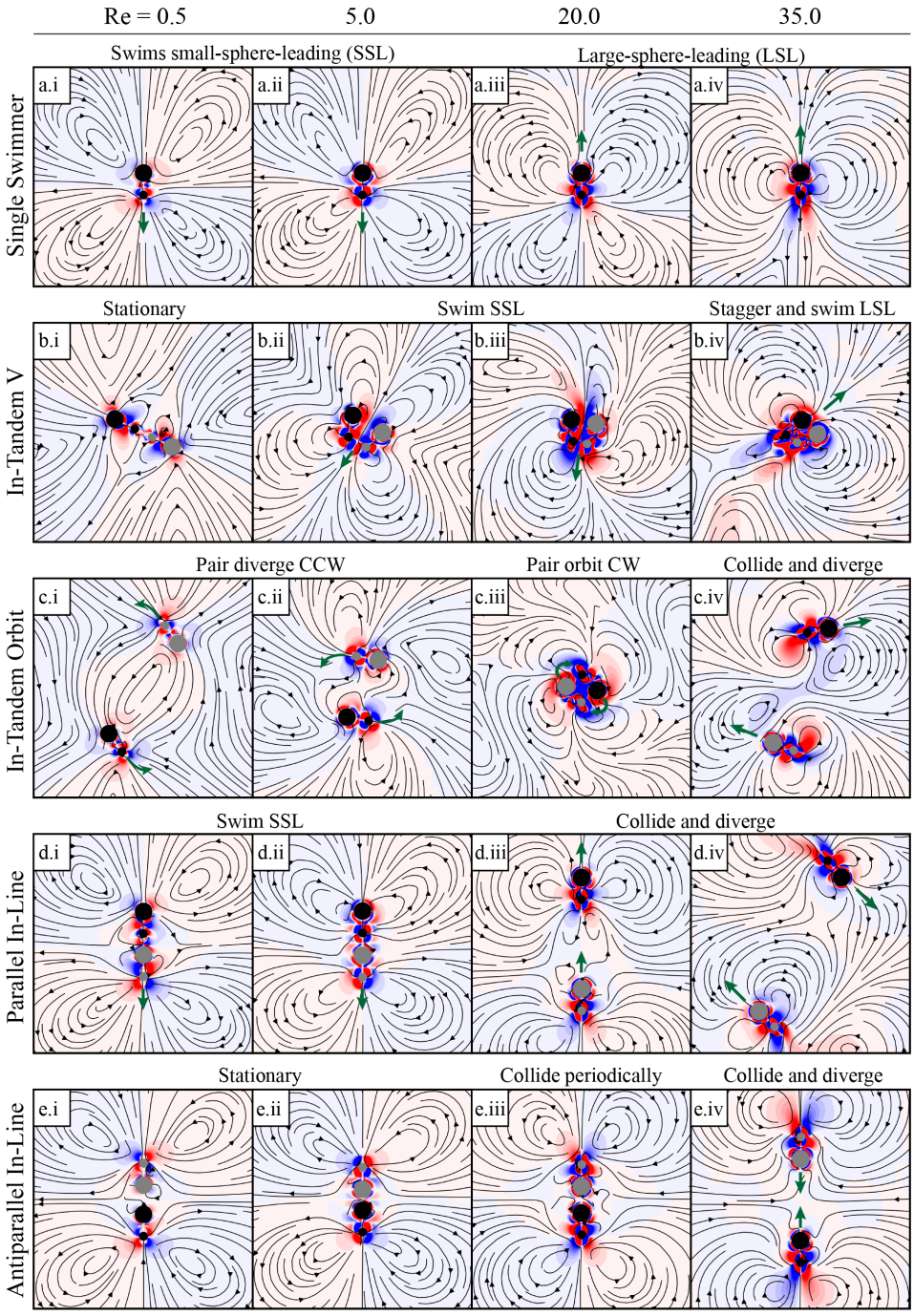

Figure 4.4: Stroke-averaged fluid flow for (a) an individual dumbbell, (b) in-tandem V, (c) in-tandem orbit, (d) parallel in-line, and (e) anti-parallel in-line on the 100th swim stroke, $\tau = 100$.(a) Individual swimmer flow and swim direction transitions from puller-like SSL (i-iii) to pusher-like LSL (iv). (b) In-tandem V forms a stationary pump pair, a V formation which swims SSL, and a staggering V formation which swims LSL. (c) In-tandem orbits diverge counter-clockwise when $\mathrm{Re} < 6.5$ and form a stable orbit when $6.5 \leq \mathrm{Re} < 30.0$. (d) Parallel in-line pairs form when $\mathrm{Re} < 10.0$ and diverge otherwise. (e) Anti-parallel in-line pairs transition from stationary pumps to swimmers in a periodically occuring head-on collision.

4.4.3 Pair fluid flows and swimming

We then investigated the details of the stable pairs identified in the previous section and studied their fluid flow fields and how they changed as a function of the Reynolds number. Before we discuss the pair, we should explain what is known for the fluid flows of the single swimmer. In our previous work, we found that the dumbbell swimmer produces a time-averaged fluid flow (steady streaming) that changes as the Re increases. Specifically, for Re < 15 the flow field is puller-like, i.e. it pulls in along the swimming axis and pushes fluid out in the perpendicular, see Fig. 4.4a.i,ii. The swimmer swims small-sphere-leading in this Re range. For Re > 15, the swimmer switches direction and swims with the large sphere on the front, while the flow field is more pusher-like, i.e. it pushes fluid away along the swimming axis and pulls fluid in on the perpendicular, see Fig. 4.4a.iii,iv and references[31,33]. Based on these findings, we might expect there to be an attraction along the swimming axis and a repulsion perpendicular when Re < 15. On the other hand, when Re > 15, we might expect there to be a repulsion along the swimming axis and an attraction on the perpendicular. What we will show next is that while sometimes this is true, the pair system is more complex and interesting.

We calculated the stroke-averaged fluid flow for the four stable pairs after they reached a steady state, over the range $0.5 \leq$ Re ≤ 50. We show four characteristic Reynolds numbers, Re = 0.5, 5, 20, and 35, that capture most of the interesting behavior, see Fig. 4.4(b-e). For comparison, we also show the stroke-averaged fluid flow for a single swimmer at the same Re, see Fig. 4.4(a).The way each pair was initialized is reported in the Supplemental Material section.

Consider the in-tandem V pair as a function of Re. For $Re > 0.5$, once the swimmers found their preferred relative positions, the pair swum together in-tandem as one. As Re increases, both the angle and distance between the swimmers get smaller, see Fig. 4.4b.ii-iv and SI. The flow field around the pair for Re $= 5$ is qualitatively different from the puller-like flow field around a single swimmer at the same Re, see Figs. 4.4b.ii and a.ii respectively. Specifically, the flow field for the pair at Re $= 5$ pulls in along the swimming axis from underneath the small spheres, pulls through the pair like a zipline, and pushes out behind the large spheres, while elongated vortices return the flow back towards the small spheres. Yet, the pair is similar to the single swimmer in that they both swim small-sphere leading. At Re $= 20$, the flow field of the pair resembles a pusher pushing fluid out along the swimming axis and pulling fluid in towards the perpendicular, though the field is not quite as symmetric as in the single swimmer case (also pusher-like), see

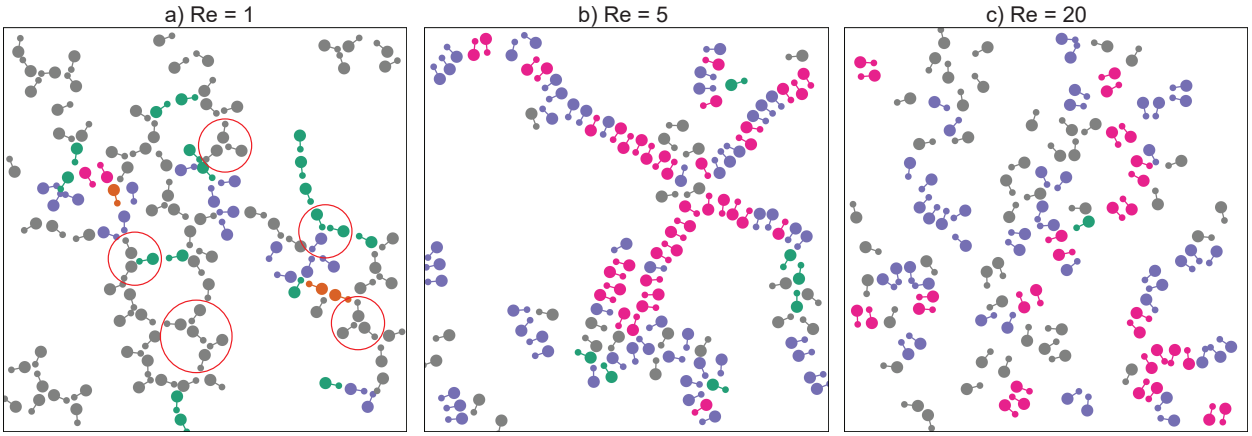

Figure 4.5: Snapshots of a system composed of 122 swimmers at a) Re $= 1$, b) Re $= 5$, and c) Re $= 20$. Swimmers are colored according to which stable pair configuration they belong: green for parallel in-line, orange for anti-parallel in-line, purple for in-tandem V, pink for in-tandem orbit, and gray for other. Note that if a swimmer appears in more than one stable pair, then its color is of the first pair identified. a) Swimmers organize in a diffuse network-like structure wherein many swimmers are in in-tandem V or parallel in-line configurations. The latter is naturally favorable in this structure. b) Most swimmers organize themselves in in-tandem orbit or in-tandem V pairs making up the network strands. c) Many swimmers are identified to form in-tandem V or in-tandem orbit pairs; however, they mostly appear in few large clusters, in sharp contrast to the network-like structures seen at Re $= 1$ and 5. Open red circles in (a) highlight some triple swimmers with the angles of 120 degrees

Fig. 4.4b.iii and a.iii or as in the V-pair at lower Re. In fact, we see an arc to the V-pair's trajectory around Re ≈ 20, which is the reason why the translational velocity plateaus between Re $= 20 - 30$, see Fig.3. For Re ≥ 35, the pair swims large-sphere-leading (as does the single swimmer) but there is an extra periodicity to the swim stroke. The pair stagger, switch leading swimmers, and shed vortices, Fig. 4.4a.iv. For a more dynamic visualization, see the movie provided in the supplemental information. Interestingly, for Re ≤ 0.5, the swimmers do not really form a V pair, as the angle between them becomes $\theta = 180$. The pair forms a line with the small spheres closest, and remains stationary overall, like a pump, see Fig. 4.4b.i. The symmetry of the pump pair is reflected in the flow field which pulls in along the line connecting the spheres of each swimmer and pushes away in the perpendicular (puller-like). Note that each swimmer individually would be swimming (albeit slowly) small-sphere-leading, see Fig. 4.4a.i. Thus, it seems that two swimmers together interacted in such a way that they formed an immotile pair.

We next studied the stroke-averaged fluid flows for the in-tandem orbit pair, see Fig. 4.4c. When Re ≤ 6, the swimmers swim away from one another, in a small-sphere-leading spiral, see Fig. 4.4c.i-ii. When $6.5 \leq$ Re ≤ 30, the swimming pair attract enough to form a large-sphere-leading stable orbit about their

combined center of mass, as shown in Fig. 4.4c.iii. Again, we see that having two interacting swimmers instead of a single one changes the dynamics: while the single swimmer transitions from small-sphere-leading to large-sphere-leading at Re $= 15$, the orbiting pair makes an analogous transition from a small-sphere-leading diverging spiral to a large-sphere-leading stable orbit at a lower Re $= 6.5$. As Re increases (e.g. Re $= 20$), when the orbiting pair rotates quickly enough, the outer set of vortices shed, and due to the rotation, the shed vortices seem to recombine with the following outer vortex, see Fig. 4.4c.iii and movie. For Re > 30, the swimming pair physically collide and are unable to maintain a stable orbit, see Fig. 4.4c.iv.

The parallel in-line pair attract and swim together as one, and the behavior of the pair is similar to that of a single swimmer: both swim small-sphere-leading and generate a flow field that is puller-like (Fig. 4.4d.i,d.ii and a.i, a.ii). For $Re > 7.5$, the swimmers collide and push away from each other, see Fig. 4.4d.iii,d.iv.

When $0.5 \leq$ Re < 10, for the antiparallel in-line (head-on) pair, the swimmers aligned along their swimming axis with their large spheres closest and formed a net-motionless pump pair, see Fig. 4.4e.i-ii. At these Reynolds numbers, each swimmer would individually swim small-sphere-leading. But as they interact with one another in pairs, they get "trapped" and form a symmetric pair that stays in place, like a pump, the fluid flows of which resemble a puller. As Re increases, the swimmers approach one another enough to the point of collision. When Re > 15, the swimmers individually swim large-sphere-leading, which results in the pair periodically colliding into one another as their swimming paths are blocked by each other, see Fig. 4.4e.iii. Eventually, for Re ≥ 35, the pair collide hard enough that they swim away from one another, see Fig. 4.4e.iv.

4.4.4 Collective Behavior of Multiple Swimmers

Our main goal for studying pair interactions was to build on our findings and explore whether from pairwise interactions we can explain the collective behavior of multiple swimmers. We note that the collective behavior of intermediate Re swimmers is largely unknown.

We studied a system of 122 identical swimmers over the Reynolds number range $0.1 \leq$ Re ≤ 40, and present three representative cases for Re $= 1$, 5, and 20. We monitored the dumbbell positions over the course of 1000 oscillations and developed an algorithm to identify stable pairs (from the previous section) that form here, too. All systems reached a statistical (and dynamical) steady state after 300 oscillations, where there is no significant change in their topology with time as confirmed by visual inspection. The pair

identification algorithm is detailed in the Supplemental Information (Section V). Fig. 4.5 shows a snapshot of the collective behavior after 500 oscillations for Re $= 1, 5,$ and 20. The swimmers are colored based on the first identified stable pair. Note that swimmers may appear in more than one stable pair.

When Re $= 1$, the swimmers organize in a network-like structure with loops and nodes, see Fig. 4.5a. The network is composed of many parallel in-line pair strands (green), as well as in-tandem V pairs (blue). The identified pairs are consistent with the pairs we expect to see at Re $= 1$. Interestingly, the swimmers also form a structure made up of three swimmers with angles of $\theta \approx 120$. This three-body interaction is found at a lot of the nodes of the network, see red circles in Fig. 4.5a, and of course could not have been predicted by pairwise interactions.

When Re $= 5$, a closer-packed network develops consisting of in-tandem V pairs and anti-parallel in-tandem orbits, though because there are many more swimmers they do not really orbit, see Fig. 4.5b (pink and blue). We notice the stable pairs dominate the collective structure, and the in-line pairs are less frequent than at Re $= 1$. There is thus a clear transition from in-line pairs to in-tandem pairs as Re increases, which is what we saw with the pairs, too. In other words, as the Reynolds number increases, we see a transition in the collective behavior from network-like in-line structures to in-tandem clustering. When Re $= 20$, the swimmers develop into localized, transient in-tandem clusters which exchange members through physical collisions, see Fig. 4.5c.

The overall trend from in-line network-like connections to in-tandem clusters as Re increases seems to hold for both pairs and multiple swimmers. The details, as well as, many-body interactions also indicate more complex behavior for the multiple swimmer case, such as the triples in Fig. 4.5a.

4.5 Conclusions

We computationally studied the pair interactions and collective behavior of asymmetric, dumbbell swimmers over a range of intermediate Reynolds numbers and initial configurations. We found rich and complex pair interactions which developed four stable pairs: in-line and in-tandem, both parallel and anti-parallel. We compared the pair swimming behavior to that of the single swimmer. The in-line stable pairs behaved much like the single swimmer transitioning from puller-like to pusher-like stroke-averaged flow fields. In contrast, for the in-tandem pairs we discovered differences in the swim direction transition as well as the stroke-averaged fluid flow directions when compared to the single swimmer. Notably, the in-tandem V

pair switched its swim direction at a higher Re than the single swimmer due to the development of a different combined swim stroke. Meanwhile, the swim direction of the in-tandem orbiting pair switched at a lower Re. We also studied a system of 122 dumbbell swimmers and found the collective behavior transitioned from in-line network-like connections to small, transient in-tandem clusters as the Reynolds number increases, consistent with the in-line to in-tandem pair behavior. Details in the collective behavior involved the formation of triples, a higher-order interaction that were not predicted by the pair or the single. Our findings show that even a simple model swimmer can demonstrate the richness of intermediate Re dynamics and collective behavior. Such rich and complex behavior indicates that an effective Reynolds number which accounts for the number of swimmers as well as pair parameters would be a better tool for describing systems with more than one swimmer.

4.6 Supplemental Information

4.6.1 Collective Methods

Previous methods of simulating a pair of dumbbell model swimmers base purely on the traditional explicit IB scheme that is computationally expensive when extending to a larger system of swimmers. This is due to i) a large number of Lagrangian marker points used to discretize the immersed structures, ii) very stiff springs used to obtain, and iii) a small time step required to advance the Navier-Stokes equations. Therefore, in this section, we describe an alternative computational approach to simulate many-swimmer systems that can overcome these inherent difficulties. Basically, the approach is a variant of a fictitious domain wherein the momentum equations for the fluid. The immersed structures are converted to a unified set of equations for the entire coupled system which then are solved on a structured Eulerian grid. Additionally, it employs distributed Lagrange multipliers to enforce the deformation kinetics of the structure given in its own reference frame.

Similar to the IB method, the momentum equations and in-compressibility constraint for the coupled fluid-structure system are described by an Eulerian formulation the motion of the immersed structures by a Lagrangian formulation. We use $\mathbf{x} \in \Omega$ to be fixed Eulerian physical coordinates and $\mathbf{s} \in U$ to be fixed Lagrangian curvilinear coordinates attached to the structures, with Ω and U are the physical regions occupied by the fluid-structure system and structures respectively. Here $U = \cup_i \left(U_r^i \cup U_R^i\right)$ where U_r^i, U_R^i are the

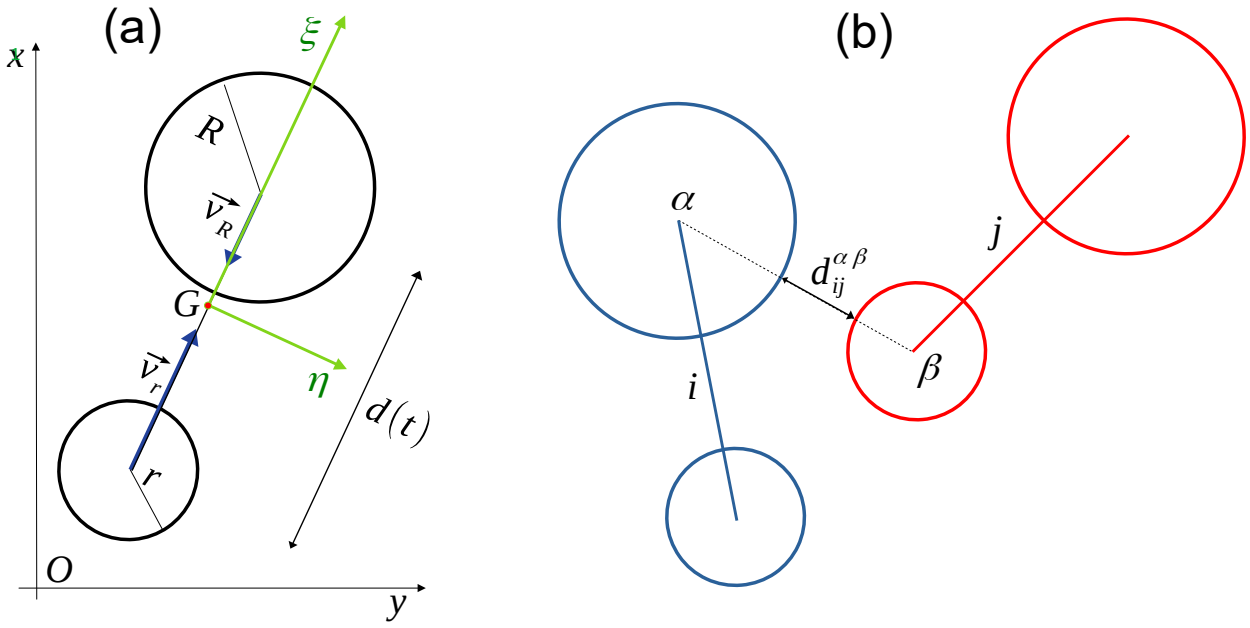

Figure 4.6: Schematic illustration of all key parameters in simulations of many-spherobot systems. (a) The deforming velocity of individual spherobot is specified in the curvilinear coordinate frame (ξ, η) fixed to the center of mass G of the model. (b) Repulsive interaction is included between individual spheres (α, β) on a pair of spherobots (i, j); where (α, β) are either small or large spheres.

(time-dependent) physical region occupied by small and large sphere of structure (dumbbell) i. The mapping $\mathbf{X}(\mathbf{s}, t) \in \Omega$ is the time-dependent physical position of the material point $\mathbf{s}$.

To enforce the time-dependent shape of an individual dumbbell swimmer , instead of using stiff springs, the deforming velocity of material point $\mathbf{s}$ in the reference frame fixed to the center of mass of the dumbbell is prescribed by

$$\mathbf{u}_k(\mathbf{X}(\mathbf{s},t),t) = \begin{cases} -2\pi f \varepsilon_R \cos(2\pi f t)\, \hat{\mathbf{e}}^i & \mathbf{X}(\mathbf{s},t) \in U_R^i \\ 2\pi f \varepsilon_r \cos(2\pi f t)\, \hat{\mathbf{e}}^i & \mathbf{X}(\mathbf{s},t) \in U_r^i \\ \mathbf{0} & \text{otherwise.} \end{cases} \tag{4.6}$$

Where ε_R and ε_r (see definition in the main text) are the amplitude of oscillation of large and small sphere respectively. $\hat{\mathbf{e}}^i$ is the swimming direction (unit) vector of the swimmer i. It is straightforward to verify that with prescribed deforming velocities, the dumbbell's oscillation is described by the same harmonic oscilator as in the main text's model, i.e. for $\hat{d}(t) = \hat{d}_0 + \varepsilon \sin(2\pi f t)$ for every swimmer.

To avoid unphysical penetration of the dumbbells, we employ a collision strategy between individual spheres on distinct swimmers. We note that, in a real fluid, high pressure would occur in the gap between the

colliding immersed structures because of squeezing out the fluid. Therefore, to resolve near contact interaction an extremely high refinement is needed, which is computationally impractical in computer simulations. A simple solution is to apply an artificial repulsion when dumbbells collide, much like an excluded volume interaction. It is important to keep in mind that this force only arises due to the discrete nature of numerical simulation, and is absent in real systems. For sphere-sphere interactions, repulsion only acts when the two spheres are sufficiently close. We adopt here a simple functional form of these forces (density) evaluated in Lagrangian form similar to previous work[120]:

$$\mathbf{F}^r_{i\alpha,j\beta}(\mathbf{s},t) = \kappa(\mathbf{X}_{i\alpha} - \mathbf{X}_{j\beta})(d_{ij}^{\alpha\beta} - \delta)^2\Theta(\delta - d_{ij}^{\alpha\beta})/(\pi R_\alpha^2); \quad \mathbf{X}(\mathbf{s},t) \in U_\alpha^i \tag{4.7}$$

where $d_{ij}^{\alpha\beta}$ is the gap between sphere $\alpha, \beta = \{R, r\}$, whose centers are located at $\mathbf{X}_{i\alpha}, \mathbf{X}_{j\beta}$ on swimmers i, j respectively. $\Theta(.)$ is the Heaviside step function, κ is the repulsion stiffness, δ is the range of the repulsion and R_α is radius of sphere α. For simplicity, $\kappa = 0.48R^3(Nm^{-3})$ and $\delta = 0.4R$ are assumed to be constant in all collisions. These parameters are chosen such that their small variations are insensitive to the resulting dynamics of the system. Then the Lagrangian repulsive force density at any physical point $\mathbf{X}$ is the sum over all large and small spheres $\mathbf{F}^r(\mathbf{s},t) = \sum_{i,\alpha,j,\beta} \mathbf{F}^r_{i\alpha,j\beta}(\mathbf{s},t)$.

A collection of spherobots are immersed in initially stationary viscous, in-compressible Newtonian fluid. The Navier-Stokes equations are

$$\rho\frac{D\mathbf{u}}{Dt}(\mathbf{x},t) = -\nabla p(\mathbf{x},t) + \mu\nabla^2\mathbf{u}(\mathbf{x},t) + \mathbf{f}^c(\mathbf{x},t) + \mathbf{f}^r(\mathbf{x},t), \tag{4.8}$$

$$\nabla\cdot\mathbf{u}(\mathbf{x},t) = 0, \tag{4.9}$$

where p is pressure to maintain the incompressibility condition, ρ is fluid density, $\mathbf{u}$ is fluid velocity, μ is fluid viscosity. $\mathbf{f}^c(\mathbf{x},t)$ and $\mathbf{f}^r(\mathbf{x},t)$ are the Eulerian body force density arising from prescribed kinematics imposed on individual dumbbells and repulsive forces between them respectively. Similar to the standard IB method, the latter is related to its Lagrangian counterpart $\mathbf{F}^r(\mathbf{s},t)$ by:

$$\mathbf{f}^r(\mathbf{x},t) = \int_U \mathbf{F}^r(\mathbf{s},t)\,\delta(\mathbf{x} - \mathbf{X}(\mathbf{s},t))\mathrm{d}\mathbf{s}, \tag{4.10}$$

$$\mathbf{f}^c(\mathbf{x},t) = \int_U \mathbf{F}^c(\mathbf{s},t)\,\delta(\mathbf{x} - \mathbf{X}(\mathbf{s},t))\mathrm{d}\mathbf{s}. \tag{4.11}$$

Where $\mathbf{F}^c(\mathbf{s},t)$ is the Lagrangian force density required to enforce the constraint of deforming velocity in the region occupied by swimmers, which has been found to be equivalent the vanish of the rate of deformation of structure in Ω_α, i.e. $\nabla(\mathbf{u}-\mathbf{u}_k(\mathbf{X},t))+\nabla(\mathbf{u}-\mathbf{u}_k(\mathbf{X},t))^T=0$ in U[121].

The equations (4.8, 4.9) with the kinematic constraint condition of rigidity and deforming velocities are solved using the an efficient and fast algorithm developed by Pantankar and co-workers[121], which has been implemented as an implicit scheme in the open-source fluid dynamics codes IBAMR[122]. For details of the spatial and temporal discretizations, interested readers are referred to the above refs.[122].

The discretization of individual dumbbells is the same in in the case of pair described in the main text, except that the spacing between marker points is now required by the algorithm to be equal the underlying grid spacing; a fact that has substantially reduces the computational cost with the current approach. Non-overlapping 122 swimmers are randomly distributed in a square simulation box with periodic boundary conditions applied on all dimensions.The simulation box size $L=70$ was used and has been found to be sufficiently large to minimize the finite size effect. A uniform grid of size $N=1400$ is used along two dimensions, resulting grid spacing of $d\hat{\mathrm{X}}=L/N=0.05R$ which is comparable as in pair's simulations.

A collection of spherobots are immersed in initially stationary viscous, in-compressible Newtonian fluid. The Navier-Stokes equations are

$$\rho\frac{D\mathbf{u}}{dt} = -\nabla p+\mu\Delta\mathbf{u}+\mathbf{f}, \tag{4.12}$$

$$\nabla\cdot\mathbf{u} = 0. \tag{4.13}$$

where p is pressure to maintain the incompressibility condition, ρ is fluid density, $\mathbf{u}$ is fluid velocity, μ is fluid viscosity and $\mathbf{f}$ is the body force density arising from prescribed kinematics imposed on individual spherobots and repulsive forces between them.

The equations (4.13) with the kinematic constraint condition of rigidity and deforming velocities are solved using the an efficient and fast algorithm developed by Pantankar and co-workers[121], which has been implemented as an implicit scheme in the open-source fluid dynamics codes IBAMR[122]. Basically, the method is a variant of a fictitious domain wherein momentum equations for the fluid and the immersed structures are converted to a single equation which is then solved on a structured Eulerian grid. This numerical approach also employs distributed Lagrange multipliers to enforce the body deformation kinetics given in the

reference frame fixed to the body. For more details and its practical implementation in IBAMR to simulate an isolated swimmer, interested readers are referred to the above refs.[121,122]. Here to simulate a collection of spherobots, it is necessary to modify the original algorithm to include the repulsive force (4.7) whenever spheres on two distinct spherobots are within the interaction range to remove any unphysical penetration between them.

4.6.2 Pair stable states

Fig. 4.7 shows the identified regions of stable pairs after steady state had been reached for Re $= 7$ based on initial configurations $\hat{H}_x$,$\hat{H}_y$, and θ.

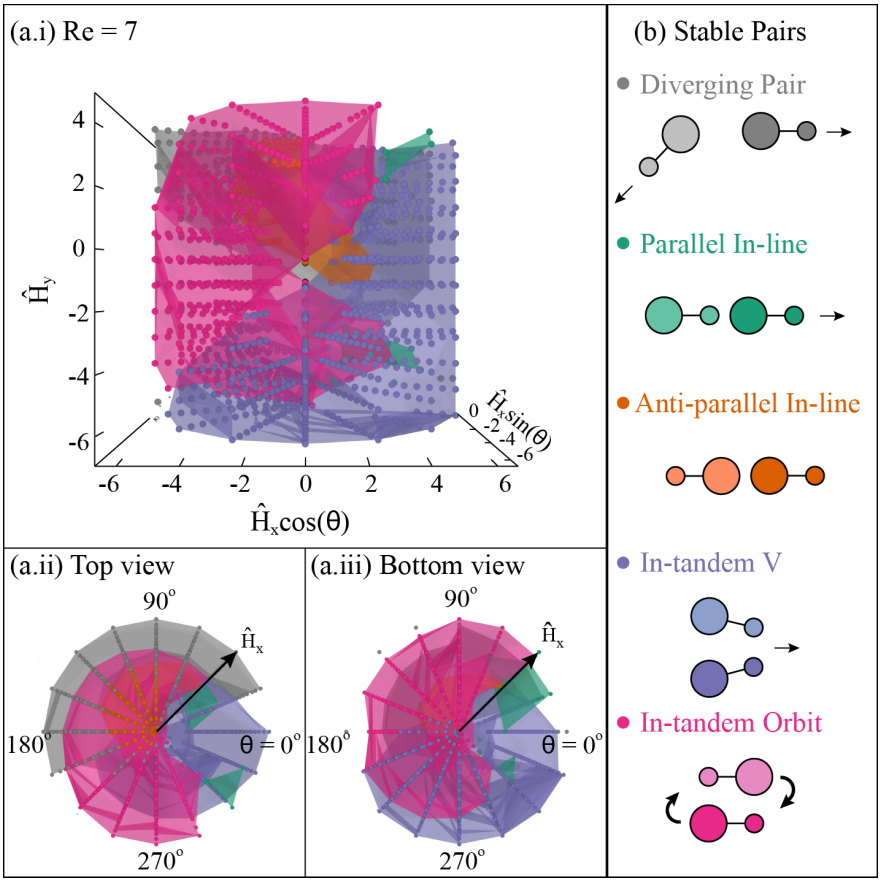

Figure 4.7: Identified regions of diverging or stable pairs after steady state had been reached for (a) Re $= 7$ based on initial configurations $\hat{H}_x$,$\hat{H}_y$, and θ. Initial configurations are determined based on the position and orientation of the grey swimmer with respect to the black swimmer. (ii) Regions of pair behavior when the grey swimmer is above the black swimmer and (iii) when the grey swimmer is below the black swimmer. (b) Schematic of pair behaviors: diverging (grey), parallel in-line (green), anti-parallel in-line (orange), in-tandem V (blue), and in-tandem orbit (pink).

4.6.3 Pair initial configurations for sweep across Re

The following are the initial conditions for the simulations presented in sections "Pair velocity as a function of Re" and "Pair fluid flows and swimming". The in-tandem V pairs were initialized with $\theta = 270.0$, $\hat{H}_x = 4.0$, and $\hat{H}_y = -1.625$. The in-tandem orbit pairs were initialized with $\theta = 180$, $\hat{H}_x = 5.0$, and $\hat{H}_y = -1.5$. The parallel in-line pairs were initialized with $\theta = 0.0$, $\hat{H}_x = 0.0$, and $\hat{H}_y = -5.0$. The anti-parallel in-line pairs were initialized with $\theta = 180.0$, $\hat{H}_x = 0.0$, and $\hat{H}_y = 3.5$.

4.6.4 Stable pair separation distances and in-tandem V angle vs. Re

Fig. 4.8a shows the separation distance for the four stable pairs after steady state has been reached as a function of Re. Fig. 4.8b shows how the angle between swimmers changes for the in-tandem V pair as Re changes.

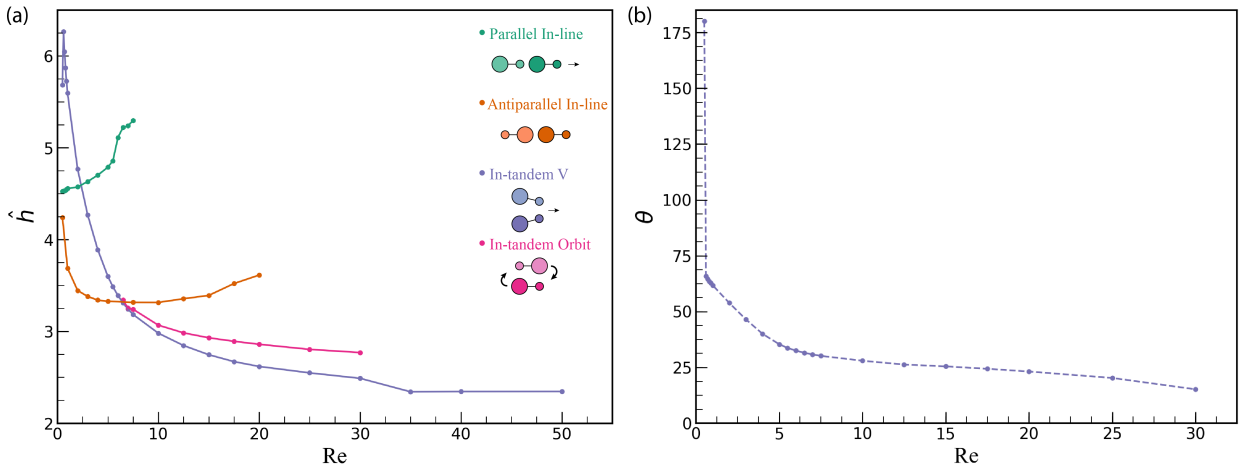

Figure 4.8: (a) The separation distance measured for the four stable pairs after they reached a steady state as a function of Re. The in-tandem pairs (pink and blue) separation monotonically decreases as Re increases, except for when Re $= 0.5$ for the in-tandem V pair. Here, the pair has formed an angle of 180 degrees with the small spheres closest. (b) The angle between the two swimmers when they form an in-tandem V pair after steady state has been reached.

4.6.5 Pair identification algorithm in multiple swimmer systems

In order to identify stable pair configuration in many-swimmer systems, we need a set of parameters characterizing for the relative position of a given pair of swimmers. These parameters should be chosen such

a way that simplifies the recognition rules employing for each pair. In addition to account for many-body effect, these rules should also respect the variation of the same parameter space observed in pair simulations for the range of Re studied in the paper. Our general strategy is to loop over all possible pairs in the system and sequentially apply the rules for each of these.

Because of sinusoidal variation of the swimmer shape, and to make the pair configuration well-defined, it is reasonable to consider only swimmer that is in equilibrium length. For a pair of such swimmers, we calculate three parameters $\{\theta_1, \theta_2, l\}$ as shown in Fig. 4.9. In principle, there are many ways to uniquely represent a pair of swimmers in space. For example, we can attach a reference frame to one swimmer and specify the coordinate of the second swimmer in this frame. However, such choice complicates the algorithm as it needs to account for the reference frame which varies from pair to pair. Therefore, our choice of parameters bases on the requirement that the corresponding identification rule is independent of which swimmer is choose as reference.

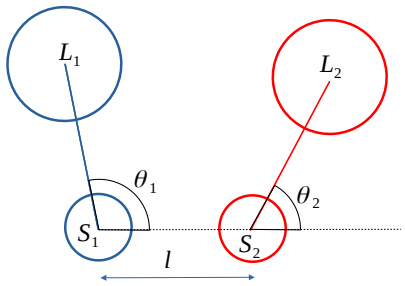

Figure 4.9: A schematic illustrates three parameters $\{\theta_1, \theta_2, l\}$ determining the relative position of two swimmers. L_i and S_i are the center of large, small sphere of swimmer i $(i = 1, 2)$ respectively. $\theta_{1(2)} \in [0°, 360°]$ are the angle between the center-line of each swimmer with respect to the direction vector $\mathbf{S_1S_2}$ whose magnitude denoted as l. These parameters are only defined for swimmer in equilibrium length. Note that if the index of swimmers is switched, the new set of parameters $\{\theta_1', \theta_2', l'\}$ can be obtained by $l' \leftarrow l$, $\theta_1' \leftarrow (180 + \theta_2)$ and $\theta_2' \leftarrow (180 + \theta_1)$, thus $\{\theta_1', \theta_2', l'\} = \{180 + \theta_2, 180 + \theta_1, l\}$.

The rules to describe specific pair configurations use different l_{thresh} as a threshold of l to remove all irrelevant pair candidates before continuing apply further restrictions. They are as follow (below R is the radius of large sphere):

a) V-shape: A pair of swimmer (1, 2) is classified as in V-shape configuration if one of the following is correct:

1. $l \leq l_{thresh}$, $\theta_1 < 180$, $\theta_2 < 180$, and $\theta_1 - \theta_2 \in (0, 90)$

2. $l \leq l_{thresh}$, $\theta_1 > 180$, $\theta_2 > 180$, and $\theta_2 - \theta_1 \in (0, 90)$

where $l_{thresh} = 3.5R$. These conditions state that two large spheres belong to each swimmer are on the same side with respect to the small-small center line and the angle created by the swimmer's axes is less than 90 degree, which agrees with the pair statistics observed in the paper. The rule is invariant relative to the swimmer index change.

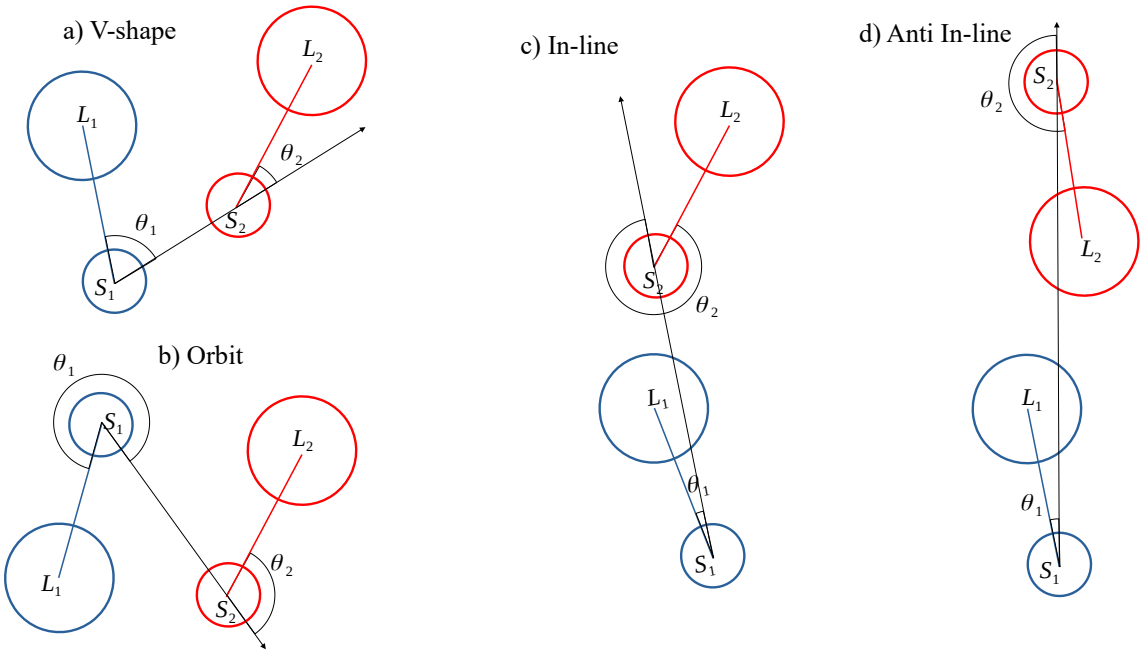

Figure 4.10: Determination of three parameters $\{\theta_1, \theta_2, l\}$ for all stable pair configurations: a) V-shape, b) Orbit, c) In-line and d) Anti In-line.

b) Orbit: A pair of swimmers (1, 2) is said to be in Orbit if $l < l_{thresh} = 5R$ and one of the following is correct:

1. $\theta_1 \in (360 - \theta_{tol1}, 360)$, $\theta_2 \in (180 - \theta_{tol1}, 180)$ and $\theta_1 - \theta_2 \in (180 - \theta_{tol2}, 180 + \theta_{tol2})$
2. $\theta_1 < \theta_{tol1}$, $\theta_2 \in (180, 180 + \theta_{tol1})$ and $\theta_2 - \theta_1 \in (180 - \theta_{tol2}, 180 + \theta_{tol2})$

where θ_{tol1} is the maximum angle allowed between either swimmer axis and the small-small center line, and θ_{tol2} controls the extent to which the swimmer directions are still considered 'aligned' (i.e in parallel). Conditions [1, 2] are equivalent if the swimmer index is switched.

c) In-line: A pair of swimmer $(1, 2)$ is classified as in In-line configuration if $l < l_{thresh}$ and one of the following is correct:

1. $\{\theta_1 < \theta_{tol1}$ or $\theta_1 > 360 - \theta_{tol1}\}$ and $\{\theta_2 < \theta_{tol2}$ or $\theta_2 > 360 - \theta_{tol2}\}$

2. $\theta_1 \in (180 - \theta_{tol1}, 180 + \theta_{tol1})$ and $\theta_2 \in (180 - \theta_{tol2}, 180 + \theta_{tol2})$

where $l_{thresh} = 6R$. Conditions [1, 2] are equivalent if we switch the swimmer indies. They state that the orientation of swimmer 1(2) can not deviate more than $\theta_{tol1}(\theta_{tol2})$ with respect to the small-small sphere axis. Here we take $\theta_{tol1} = 10$ and $\theta_{tol2} = 30$. Of course, different values can be used.

(d) Anti In-line: A pair of swimmer (1, 2) is said to be in Anti In-line if $l < l_{thresh} = 8R$ and the following is correct:

1. $\{\theta_1 < \theta_{tol}$ or $\theta_1 > 360 - \theta_{tol}\}$ and $\{\theta_2 \in (180 - \theta_{tol}, 180 + \theta_{tol})\}$.

Here $\theta_{tol} = 10$ is tolerance of the deviation of either swimmer direction relative to the small-small sphere axis. Clearly, the rule is independent of the swimmer index.

BIBLIOGRAPHY

[1] Daphne Klotsa. As above, so below, and also in between: mesoscale active matter in fluids. Soft matter, 15(44):8946–8950, 2019.

[2] MJ Lighthill. On the squirming motion of nearly spherical deformable bodies through liquids at very small reynolds numbers. Communications on Pure and Applied Mathematics, 5(2):109–118, 1952.

[3] John R Blake. A spherical envelope approach to ciliary propulsion. Journal of Fluid Mechanics, 46 (1):199–208, 1971.

[4] Ian K Bartol, Paul S Krueger, William J Stewart, and Joseph T Thompson. Pulsed jet dynamics of squid hatchlings at intermediate Reynolds numbers. The Journal of Experimental Biology, 2009. ISSN 0022-0949. doi: 10.1242/jeb.033241.

[5] Gregory Herschlag and Laura Miller. Reynolds number limits for jet propulsion: a numerical study of simplified jellyfish. Journal of theoretical biology, 285(1):84–95, 2011.

[6] Stefan Kern and Petros Koumoutsakos. Simulations of optimized anguilliform swimming. Journal of Experimental Biology, 209(24):4841–4857, 2006.

[7] Lee A Fuiman and Paul W Webb. Ontogeny of routine swimming activity and performance in zebra danios (Teleostei: Cyprinidae). Animal Behaviour, 36(1):250–261, 1988.

[8] J. Sznitman, X. Shen, R. Sznitman, and P. E. Arratia. Propulsive force measurements and flow behavior of undulatory swimmers at low Reynolds number. Physics of Fluids, 22(12):121901, dec 2010. ISSN 1070-6631. doi: 10.1063/1.3529236. URL http://aip.scitation.org/doi/10.1063/1.3529236.

[9] Matthew J McHenry, Emanuel Azizi, and James A Strother. The hydrodynamics of locomotion at intermediate Reynolds numbers: undulatory swimming in ascidian larvae (Botrylloides sp.). Journal of Experimental Biology, 206(2):327–343, 2003.

[10] Amneet Pal Singh Bhalla, Boyce E Griffith, and Neelesh A Patankar. A forced damped oscillation framework for undulatory swimming provides new insights into how propulsion arises in active and passive swimming. PLoS computational biology, 9(6):e1003097, 2013.

[11] Brendan J Borrell, Jeremy A Goldbogen, and Robert Dudley. Aquatic wing flapping at low Reynolds numbers: swimming kinematics of the Antarctic pteropod, Clione antarctica. Journal of Experimental Biology, 208(15):2939–2949, 2005.

[12] Brad J Gemmell, Houshuo Jiang, and Edward J Buskey. A tale of the ciliate tail: Investigation into the adaptive significance of this sub-cellular structure. In Proc. R. Soc. B, volume 282, page 20150770. The Royal Society, 2015.

[13] Houshuo Jiang. Why does the jumping ciliate Mesodinium rubrum possess an equatorially located propulsive ciliary belt? Journal of plankton research, page fbr007, 2011.

[14] J Rudi Strickler. Swimming of planktonic Cyclops species (Copepoda, Crustacea): pattern, movements and their control. In Swimming and flying in nature, pages 599–613. Springer, 1975.

[15] R W Blake. Hydrodynamics of swimming in the water boatman, Cenocorixa bifida. Canadian journal of zoology, 64(8):1606–1613, 1986.

[16] Monica M Wilhelmus and John O Dabiri. Observations of large-scale fluid transport by laser-guided plankton aggregations a). Physics of Fluids, 26(10):101302, 2014.

[17] Janna C Nawroth and John O Dabiri. Induced drift by a self-propelled swimmer at intermediate Reynolds numbers. Physics of Fluids, 26(9):Art–No, 2014.

[18] Shannon K Jones, Young JJ Yun, Tyson L Hedrick, Boyce E Griffith, and Laura A Miller. Bristles reduce the force required to 'fling' wings apart in the smallest insects. Journal of Experimental Biology, 219(23):3759–3772, 2016.

[19] Eric Lauga. Continuous breakdown of purcell's scallop theorem with inertia. Physics of Fluids, 19(6): 061703, 2007. doi: 10.1063/1.2738609. URL http://dx.doi.org/10.1063/1.2738609.

[20] S Wang and A Ardekani. Inertial squirmer. Physics of Fluids, 24(10):101902, 2012.

[21] Aditya S Khair and Nicholas G Chisholm. Expansions at small reynolds numbers for the locomotion of a spherical squirmer. Physics of Fluids, 26(1):011902, 2014.

[22] Nicholas G. Chisholm, Dominique Legendre, Eric Lauga, and Aditya S. Khair. A squirmer across reynolds numbers. Journal of Fluid Mechanics, 796:233–256, 2016. doi: 10.1017/jfm.2016.239.

[23] Gaojin Li, Anca Ostace, and Arezoo M. Ardekani. Hydrodynamic interaction of swimming organisms in an inertial regime. Physical Review E, 94(5):053104, nov 2016. doi: 10.1103/PhysRevE.94.053104. URL https://journals.aps.org/pre/abstract/10.1103/PhysRevE.94.053104.

[24] Nicholas G Chisholm and Aditya S Khair. Partial drift volume due to a self-propelled swimmer. Physical Review Fluids, 3(1):014501, 2018.

[25] Raksha Mahalinkam, Felicity Gong, and Aditya S Khair. Reduced-order model for inertial locomotion of a slender swimmer. Physical Review E, 97(4):043102, 2018.

[26] Jie Zhang, Nan-Sheng Liu, and Xi-Yun Lu. Locomotion of a passively flapping flat plate. Journal of Fluid Mechanics, 659:43–68, 2010.

[27] Saverio E Spagnolie, Lionel Moret, Michael J Shelley, and Jun Zhang. Surprising behaviors in flapping locomotion with passive pitching. Physics of Fluids, 22(4):041903, 2010.

[28] Daphne Klotsa, Kyle A Baldwin, Richard J A Hill, R M Bowley, and Michael R Swift. Propulsion of a Two-Sphere Swimmer. Phys. Rev. Lett., 115(24):248102, 2015. doi: 10.1103/PhysRevLett.115.248102.

[29] B. U. Felderhof. Effect of fluid inertia on the motion of a collinear swimmer. Physical Review E, 063114(6):1–7, dec 2016. ISSN 15502376. doi: 10.1103/PhysRevE.94.063114. URL http://link.aps.org/doi/10.1103/PhysRevE.94.063114.

[30] Jesse F Collis, Debadi Chakraborty, and John E Sader. Autonomous propulsion of nanorods trapped in an acoustic field. Journal of Fluid Mechanics, 825:29–48, 2017.

[31] Thomas Dombrowski, Shannon K Jones, Georgios Katsikis, Amneet Pal Singh Bhalla, Boyce E Griffith, and Daphne Klotsa. Transition in swimming direction in a model self-propelled inertial swimmer. Physical Review Fluids, 4(2):021101, 2019.

[32] Tejaswin Parthasarathy, Fan Kiat Chan, and Mattia Gazzola. Streaming-enhanced flow-mediated transport. Journal of Fluid Mechanics, 878:647–662, 2019.

[33] Thomas Dombrowski and Daphne Klotsa. Kinematics of a simple reciprocal model swimmer at intermediate reynolds numbers. Physical Review Fluids, 5(6):063103, 2020.

[34] E. M. Purcell. Life at low Reynolds number. American Journal of Physics, 45(1):3–11, jan 1977. ISSN 0002-9505. doi: 10.1119/1.10903. URL http://aapt.scitation.org/doi/10.1119/1.10903.

[35] Victor China and Roi Holzman. Hydrodynamic starvation in first-feeding larval fishes. Proceedings of the National Academy of Sciences, 111(22):8083–8088, 2014.

[36] Stephen Childress and Robert Dudley. Transition from ciliary to flapping mode in a swimming mollusc: flapping flight as a bifurcation in re_ω. Journal of Fluid Mechanics, 498:257–288, 2004.

[37] Ulrike K Müller, Jos GM van den Boogaart, and Johan L van Leeuwen. Flow patterns of larval fish: undulatory swimming in the intermediate flow regime. Journal of Experimental Biology, 211(2): 196–205, 2008.

[38] N. Riley. On a sphere oscillating in a viscous fluid. Quart. Journ. Mech. and Applied Math, XIX:461–472, 1966. URL http://qjmam.oxfordjournals.org/cgi/doi/10.1093/qjmam/19.4.461.

[39] N Riley. Steady streaming. Annual Review of Fluid Mechanics, 33:43–65, 2001.

[40] Werner Nachtigall. Some aspects of Reynolds number effects in animals. Mathematical Methods in the Applied Sciences, 24(17-18):1401–1408, nov 2001. ISSN 0170-4214. doi: 10.1002/mma.188. URL http://doi.wiley.com/10.1002/mma.188.

[41] Steven Vogel. Life's devices. Princeton University Press, 1988.

[42] Steven Vogel. Life in moving fluids : the physical biology of flow. Princeton University Press, 1994. ISBN 0691026165. URL https://books.google.com/books/about/Life{_}in{_}Moving{_}Fluids.html?id=XBqncfXFsOIC.

[43] Wei Wang, Wentao Duan, Suzanne Ahmed, Ayusman Sen, and Thomas E Mallouk. From one to many: Dynamic assembly and collective behavior of self-propelled colloidal motors. Accounts of chemical research, 48(7):1938–1946, 2015.

[44] Debabrata Patra, Samudra Sengupta, Wentao Duan, Hua Zhang, Ryan Pavlick, and Ayusman Sen. Intelligent, self-powered, drug delivery systems. Nanoscale, 5(4):1273–1283, 2013.

[45] Sherif Tolba, Reda Ammar, and Sanguthevar Rajasekaran. Taking swarms to the field: A framework for underwater mission planning. In Computers and Communication (ISCC), pages 1007–1013. IEEE, 2015.

[46] Ryo Fujiwara, Takeshi Kano, and Akio Ishiguro. Self-swarming robots that exploit hydrodynamical interaction. Advanced Robotics, 28(9):639–645, 2014.

[47] Miguel Duarte, Vasco Costa, Jorge Gomes, Tiago Rodrigues, Fernando Silva, Sancho Moura Oliveira, and Anders Lyhne Christensen. Evolution of collective behaviors for a real swarm of aquatic surface robots. PloS one, 11(3):e0151834, 2016.

[48] Stephen Childress. Mechanics of swimming and flying. Cambridge University Press, 1981.

[49] Eric Lauga and Thomas R Powers. The hydrodynamics of swimming microorganisms. Reports on Progress in Physics, 72(9):096601, sep 2009. ISSN 0034-4885. doi: 10.1088/0034-4885/72/9/096601.

[50] Eric Kunze, John F Dower, Ian Beveridge, Richard Dewey, and Kevin P Bartlett. Observations of biologically generated turbulence in a coastal inlet. Science, 313(5794):1768–1770, 2006.

[51] Isabel A Houghton, Jeffrey R Koseff, Stephen G Monismith, and John O Dabiri. Vertically migrating swimmers generate aggregation-scale eddies in a stratified column. Nature, page 1, 2018.

[52] Eugene J Chang and Martin R Maxey. Unsteady flow about a sphere at low to moderate reynolds number. part 1. oscillatory motion. Journal of Fluid Mechanics, 277:347–379, 1994.

[53] Charlotte W Kotas, Minami Yoda, and Peter H Rogers. Visualization of steady streaming near oscillating spheroids. Experiments in fluids, 42(1):111–121, 2007.

[54] Florian Otto, Emmalee K Riegler, and Greg A Voth. Measurements of the steady streaming flow around oscillating spheres using three dimensional particle tracking velocimetry. Physics of fluids, 20 (9):093304, 2008.

[55] D. Klotsa, Michael R. Swift, R. M. Bowley, and P. J. King. Interaction of spheres in oscillatory fluid flows. Phys. Rev. E, 76:056314, Nov 2007. doi: 10.1103/PhysRevE.76.056314. URL https://link.aps.org/doi/10.1103/PhysRevE.76.056314.

[56] H. S. Wright, Michael R. Swift, and P. J. King. Migration of an asymmetric dimer in oscillatory fluid flow. Phys. Rev. E, 78:036311, Sep 2008. doi: 10.1103/PhysRevE.78.036311. URL https://link.aps.org/doi/10.1103/PhysRevE.78.036311.

[57] D. Klotsa, Michael R. Swift, R. M. Bowley, and P. J. King. Chain formation of spheres in oscillatory fluid flows. Phys. Rev. E, 79:021302, Feb 2009. doi: 10.1103/PhysRevE.79.021302. URL https://link.aps.org/doi/10.1103/PhysRevE.79.021302.

[58] Tamsin A. Spelman and Eric Lauga. Arbitrary axisymmetric steady streaming: flow, force and propulsion. Journal of Engineering Mathematics, 105(1):31–65, 2017. doi: 10.1007/s10665-016-9880-8. URL https://doi.org/10.1007/s10665-016-9880-8.

[59] Barry R Lutz, Jian Chen, and Daniel T Schwartz. Hydrodynamic tweezers: 1. noncontact trapping of single cells using steady streaming microeddies. Analytical chemistry, 78(15):5429–5435, 2006.

[60] Kurt M. Ehlers and Jair Koiller. Could cell membranes produce acoustic streaming? making the case for synechococcus self-propulsion. Mathematical and Computer Modelling, 53(7):1489 – 1504, 2011. ISSN 0895-7177. doi: https://doi.org/10.1016/j.mcm.2010.03.054. URL http://www.sciencedirect.com/science/article/pii/S089571771000172X. Mathematical Methods and Modelling of Biophysical Phenomena.

[61] Charles S. Peskin. The immersed boundary method. Acta Numerica, 11:479–517, jan 2002. ISSN 0962-4929. doi: 10.1017/S0962492902000077. URL http://www.journals.cambridge.org/abstract{_}S0962492902000077.

[62] B. Kallemov, A. P. S. Bhalla, B. E. Griffith, and A. Donev. An immersed boundary method for rigid bodies. Comm Appl Math Comput Sci, 11(1):79–141, 2016.

[63] F. Balboa Usabiaga, B. Kallemov, B. Delmotte, A. P. S. Bhalla, B. E. Griffith, and A. Donev. Hydrodynamics of suspensions of passive and active rigid particles: a rigid multiblob approach. Communications in Applied Mathematics and Computational Science, 11(2):217–296, 2016. doi: 10.2140/camcos.2016.11.217.

[64] IBAMR: An adaptive and distributed-memory parallel implementation of the immersed boundary method. https://github.com/IBAMR/IBAMR.

[65] Hank Childs, Eric Brugger, Brad Whitlock, Jeremy Meredith, Sean Ahern, David Pugmire, Kathleen Biagas, Mark Miller, Cyrus Harrison, Gunther H. Weber, Hari Krishnan, Thomas Fogal, Allen Sanderson, Christoph Garth, E. Wes Bethel, David Camp, Oliver Rübel, Marc Durant, Jean M. Favre, and Paul Navrátil. VisIt: An End-User Tool For Visualizing and Analyzing Very Large Data. In High Performance Visualization-Enabling Extreme-Scale Scientific Insight, pages 357–372. Oct 2012.

[66] Boyce E Griffith, Richard D Hornung, David M McQueen, and Charles S Peskin. An adaptive, formally second order accurate version of the immersed boundary method. Journal of Computational Physics, 223(1):10–49, 2007.

[67] See Supplementary Material at http://link.aps.org/supplemental/10.1103/PhysRevFluids.4.021101 for more details on methods, additional figures and movies of the spherobot.

[68] J Milton Andres and Uno Ingard. Acoustic streaming at low reynolds numbers. The Journal of the Acoustical Society of America, 25(5):932–938, 1953.

[69] Z Zapryanov, Zh Kozhoukharova, and A Iordanova. On the hydrodynamic interaction of two circular cylinders oscillating in a viscous fluid. Zeitschrift für angewandte Mathematik und Physik ZAMP, 39 (2):204–220, 1988.

[70] SS Tabakova and ZD Zapryanov. On the hydrodynamic interaction of two spheres oscillating in a viscous fluid. i. axisymmetrical case. Zeitschrift für angewandte Mathematik und Physik ZAMP, 33 (3):344–357, 1982.

[71] SS Tabakova and ZD Zapryanov. On the hydrodynamic interaction of two spheres oscillating in a viscous fluid. ii. three dimensional case. Zeitschrift für Angewandte Mathematik und Physik (ZAMP), 33(4):487–502, 1982.

[72] R.S. Alassar and H.M. Badr. Oscillating viscous flow over a sphere. Computers & Fluids, 26 (7):661–682, sep 1997. ISSN 00457930. doi: 10.1016/S0045-7930(97)00017-0. URL http://www.sciencedirect.com/science/article/pii/S0045793097000170.

[73] H. M. Blackburn. Mass and momentum transport from a sphere in steady and oscillatory flows. Physics of Fluids, 14(11):3997–4011, 2002. doi: 10.1063/1.1510448. URL https://doi.org/10.1063/1.1510448.

[74] Masakazu Tatsuno. Circulatory streaming around an oscillating circular cylinder at low reynolds numbers. Journal of the Physical Society of Japan, 35(3):915–920, 1973.

[75] W Coenen and N Riley. Oscillatory flow about a cylinder pair. Quarterly journal of mechanics and applied mathematics, 62(1):53–66, 2008.

[76] Masakazu Tatsuno. Secondary flow induced by a circular cylinder performing unharmonic oscillations. Journal of the Physical Society of Japan, 50(1):330–337, 1981.

[77] Tore Olsen. Rotational flow of a viscous fluid. The Journal of the Acoustical Society of America, 28 (2):313–314, 1956.

[78] J Holtsmark, I Johnsen, To Sikkeland, and S Skavlem. Boundary layer flow near a cylindrical obstacle in an oscillating, incompressible fluid. The journal of the acoustical society of America, 26(1):26–39, 1954.

[79] T. J. Pedley. Spherical squirmers: models for swimming micro-organisms. IMA Journal of Applied Mathematics, 81(3):488–521, 2016. doi: 10.1093/imamat/hxw030. URL http://dx.doi.org/10.1093/imamat/hxw030.

[80] Kurt Ehlers and Jair Koiller. Synechococcus as a" singing" bacterium: biology inspired by micro-engineered acoustic streaming devices. arXiv preprint arXiv:0903.3781, 2009.

[81] François Nadal and Eric Lauga. Asymmetric steady streaming as a mechanism for acoustic propulsion of rigid bodies. Physics of Fluids, 26(8):082001, 2014.

[82] Mohammad Mohaghar, Deepak Adhikari, and Donald R Webster. Characteristics of swimming shelled antarctic pteropods (limacina helicina antarctica) at intermediate reynolds number regime. Physical Review Fluids, 4(11):111101, 2019.

[83] GP Alexander and JM Yeomans. Dumb-bell swimmers. EPL (Europhysics Letters), 83(3):34006, 2008.

[84] Eric Lauga and Denis Bartolo. No many-scallop theorem: Collective locomotion of reciprocal swimmers. Phys. Rev. E, 78:030901, Sep 2008. doi: 10.1103/PhysRevE.78.030901. URL https://link.aps.org/doi/10.1103/PhysRevE.78.030901.

[85] Victor B Putz and Jörn Dunkel. Low reynolds number hydrodynamics of asymmetric, oscillating dumbbell pairs. The European Physical Journal Special Topics, 187(1):135–144, 2010.

[86] Ali Najafi and Ramin Golestanian. Simple swimmer at low Reynolds number: Three linked spheres. Physical Review E, 69(6):062901, jun 2004. ISSN 1539-3755. doi: 10.1103/PhysRevE.69.062901. URL https://link.aps.org/doi/10.1103/PhysRevE.69.062901.

[87] JE Avron, O Kenneth, and DH Oaknin. Pushmepullyou: an efficient micro-swimmer. New Journal of Physics, 7(1):234, 2005.

[88] Raymond E Goldstein. Batchelor prize lecture fluid dynamics at the scale of the cell. Journal of Fluid Mechanics, 807:1–39, 2016.

[89] Stewart A Mallory, Chantal Valeriani, and Angelo Cacciuto. An active approach to colloidal self-assembly. Annual review of physical chemistry, 69:59–79, 2018.

[90] M Omar Din, Tal Danino, Arthur Prindle, Matt Skalak, Jangir Selimkhanov, Kaitlin Allen, Ellixis Julio, Eta Atolia, Lev S Tsimring, Sangeeta N Bhatia, et al. Synchronized cycles of bacterial lysis for in vivo delivery. Nature, 536(7614):81–85, 2016.

[91] Terri A Williams. A model of rowing propulsion and the ontogeny of locomotion in artemia larvae. The Biological Bulletin, 187(2):164–173, 1994.

[92] Andrew T Sensenig, Kenneth T Kiger, and Jeffrey W Shultz. The rowing-to-flapping transition: ontogenetic changes in gill-plate kinematics in the nymphal mayfly centroptilum triangulifer (ephemeroptera, baetidae). Biological journal of the Linnean Society, 98(3):540–555, 2009.

[93] Nicolas Vandenberghe, Stephen Childress, and Jun Zhang. On unidirectional flight of a free flapping wing. Physics of Fluids, 18(1):014102, 2006.

[94] Nicolas Vandenberghe, Jun Zhang, and Stephen Childress. Symmetry breaking leads to forward flapping flight. Journal of Fluid Mechanics, 506:147–155, 2004.

[95] Silas Alben and Michael Shelley. Coherent locomotion as an attracting state for a free flapping body. Proceedings of the National Academy of Sciences, 102(32):11163–11166, 2005.

[96] Hermann Schlichting and Klaus Gersten. Boundary-layer theory. Springer, 2017.

[97] W. Coenen. Steady streaming around a cylinder pair. Proceedings of the Royal Society A: Mathematical, Physical and Engineering Sciences, 472(2195):20160522, 2016. doi: 10.1098/rspa.2016.0522. URL https://royalsocietypublishing.org/doi/abs/10.1098/rspa.2016.0522.

[98] Frank E Fish. Transitions from drag-based to lift-based propulsion in mammalian swimming. American Zoologist, 36(6):628–641, 1996.

[99] Silas Alben, LA Miller, and Jifeng Peng. Efficient kinematics for jet-propelled swimming. Journal of Fluid Mechanics, 733:100–133, 2013.

[100] Gary S. Klindt and Benjamin M. Friedrich. Flagellar swimmers oscillate between pusher- and puller-type swimming. Physical Review E, 92(6):063019, dec 2015. ISSN 1539-3755. doi: 10.1103/PhysRevE.92.063019. URL https://link.aps.org/doi/10.1103/PhysRevE.92.063019.

[101] Haribalan Kumar, Merryn H Tawhai, Eric A Hoffman, and Ching-Long Lin. Steady streaming: A key mixing mechanism in low-reynolds-number acinar flows. Physics of Fluids, 23(4):041902, 2011.

[102] James B Grotberg. Respiratory fluid mechanics. Physics of Fluids, 23(2):021301, 2011.

[103] Haoran Xu, Justas Dauparas, Debasish Das, Eric Lauga, and Yilin Wu. Self-organization of swimmers drives long-range fluid transport in bacterial colonies. Nature communications, 10(1):1–12, 2019.

[104] Douglas H Kelley and Nicholas T Ouellette. Emergent dynamics of laboratory insect swarms. Scientific reports, 3(1):1–7, 2013.

[105] Andrey Sokolov, Shuang Zhou, Oleg D Lavrentovich, and Igor S Aranson. Individual behavior and pairwise interactions between microswimmers in anisotropic liquid. Physical Review E, 91(1):013009, 2015.

[106] Gwynn J Elfring and Eric Lauga. Passive hydrodynamic synchronization of two-dimensional swimming cells. Physics of Fluids, 23(1):011902, 2011.

[107] Yingzi Yang, Jens Elgeti, and Gerhard Gompper. Cooperation of sperm in two dimensions: synchronization, attraction, and aggregation through hydrodynamic interactions. Physical review E, 78(6):061903, 2008.

[108] Takuji Ishikawa, MP Simmonds, and Timothy J Pedley. Hydrodynamic interaction of two swimming model micro-organisms. Journal of Fluid Mechanics, 568:119, 2006.

[109] Alex Kanevsky, Michael J Shelley, and Anna-Karin Tornberg. Modeling simple locomotors in stokes flow. Journal of Computational Physics, 229(4):958–977, 2010.

[110] Kevin Lippera, Michael Benzaquen, and Sébastien Michelin. Bouncing, chasing, or pausing: Asymmetric collisions of active droplets. Physical Review Fluids, 5(3):032201, 2020.

[111] Kevin Lippera, Michael Benzaquen, and Sébastien Michelin. Alignment and scattering of colliding active droplets. Soft Matter, 17(2):365–375, 2021.

[112] Jair Koiller, Kurt Ehlers, and Richard Montgomery. Problems and progress in microswimming. Journal of Nonlinear Science, 6(6):507–541, 1996.

[113] Victor B. Putz and Jörn Dunkel. Low Reynolds number hydrodynamics of asymmetric, oscillating dumbbell pairs. The European Physical Journal Special Topics, 187(1):135–144, sep 2010. ISSN 1951-6355. doi: 10.1140/epjst/e2010-01278-y. URL http://www.springerlink.com/index/10.1140/epjst/e2010-01278-y.

[114] Brad J Gemmell, Jian Sheng, and Edward J Buskey. Compensatory escape mechanism at low reynolds number. Proceedings of the National Academy of Sciences, 110(12):4661–4666, 2013.

[115] Ingo O Götze and Gerhard Gompper. Mesoscale simulations of hydrodynamic squirmer interactions. Physical Review E, 82(4):041921, 2010.

[116] Gaojin Li, Anca Ostace, and Arezoo M Ardekani. Hydrodynamic interaction of swimming organisms in an inertial regime. Physical Review E, 94(5):053104, 2016.

[117] Rayan Chatterjee, Navdeep Rana, R Aditi Simha, Prasad Perlekar, and Sriram Ramaswamy. Fluid flocks with inertia. arXiv preprint arXiv:1907.03492, 2019.

[118] Boyce E Griffith. Immersed boundary model of aortic heart valve dynamics with physiological driving and loading conditions. International Journal for Numerical Methods in Biomedical Engineering, 28 (3):317–345, 2012.

[119] Boyce E. Griffith, Xiaoyu Luo, David M. McQueen, and Charles S. Peskin. Simulating the fluid dynamics of natural and prosthetic heart valves using the immersed boundary method. Int. J. Appl. Mech., 1(1):137–177, mar 2009. ISSN 17588251. doi: 10.1142/S1758825109000113.

[120] R Glowinski, T Pan, T I Hesla, and D D Joseph. A distributed Lagrange multiplier fictitious domain method for particulate flows. Int. J. Multiph. Flow, 25:755–794, 1999.

[121] Anup A. Shirgaonkar, Malcolm A. MacIver, and Neelesh A. Patankar. A new mathematical formulation and fast algorithm for fully resolved simulation of self-propulsion. J. Comput. Phys., 228(7):2366–2390, apr 2009. ISSN 10902716. doi: 10.1016/j.jcp.2008.12.006.

[122] Amneet Pal Singh Bhalla, Rahul Bale, Boyce E. Griffith, and Neelesh A. Patankar. A unified mathematical framework and an adaptive numerical method for fluid-structure interaction with rigid, deforming, and elastic bodies. J. Comput. Phys., 250:446–476, 2013. ISSN 10902716. doi: 10.1016/j.jcp.2013.04.033. URL http://dx.doi.org/10.1016/j.jcp.2013.04.033.